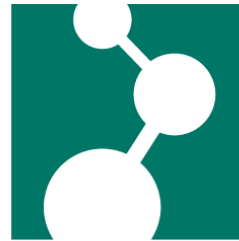# Fabrication and applications of superhydrophobic and superamphiphobic surface

Dissertation

Zur Erlangung des Grades

"Doktor der Naturwissenschaften"

im Promotionsfach Physikalische Chemie

der Johannes Gutenberg-Universität Mainz

Xu Deng

geboren in Chongqing, P.R China

Mainz, 2013

Die vorliegende Arbeit wurde am Max-Planck-Institut für Polymerforschung in Mainz unter der Betreuung von Dr.Doris Vollmer und Prof. Dr. H.-J. Butt in der Zeit von October 2009 bis July 2013 angefertigt.

Dekan: Prof. Dr. Holger Frey

1. Berichterstatter: PD Dr. Doris Vollmer

2. Berichterstatter: Prof. Dr. Wolfgang Tremel

Table of Contents

Abstract

A major goal in coating research is to design self-cleaning surfaces. Many surfaces in nature are superhydrophobic – for example lotus leaves. Mimicking its surface morphology led to the development of a number of artificial superhydrophobic surfaces, offering many applications in industrial and biological processes. The self-cleaning property results from microscopic pockets of air, which are trapped beneath the water drops. This composite interface leads to an increase in the macroscopic contact angle and reduced contact angle hysteresis, enabling water droplets to roll off easily. In chapter 2 of this thesis, we describe the fabrication of lotus leaf-like superhydrophobic surface, using porous silica capsules as key component. The latter are highly transparent as well as mechanically and thermally stable. When used as transparent coatings for organic solar cells they leave their performance unaffected.

However, slightly lowering the water-air interfacial tension by adding an organic liquid such as alcohol or oil decreases the interfacial tension sufficiently to induce homogeneous wetting of the surface. Contrary to superhydrophobic surfaces, the fabrication of "superamphiphobic" surfaces is much more difficult. The reason is that organic liquids have a contact angle less than 90° on low surface energy flat surface. According to Young's equation, $\cos\Theta = (\gamma - \gamma_{SL})/\gamma_{LV}$, i.e. $\gamma_{SV} - \gamma_{SL}$ is always positive. To fabricate superamphiphobic surfaces overhangs, re-entrant geometry or convex curvature is required. Incomplete understanding of the meaning and the complex interplay between these three key parameters – surface roughness, energy and topography – has so far made it difficult and expensive to fabricate superamphiphobic surfaces. Examples are rare, and none fulfils the requirements of thermal and mechanical stability, and transparency simultaneously. In the chapter 3 of the thesis we demonstrate a simple way to template candle soot to make robust, transparent superamphiphobic surfaces.

Impact dynamics of liquid drops is of high importance in a variety of industrial processes such as rapid spray cooling, spray painting and coating, precision solder-drop dispersions in microelectronics, or deposition of pesticides on plant leaves. In chapter 4, we investigate the impact dynamics of drops with low interfacial tension on superamphiphobic layers. The dependence of the interfacial tension and viscosity has been systematically studied.

Since low surface tension organic liquids, melts and monomer solutions can form spherical droplets on superamphiphobic coating. In the chapter 5 we show that polymeric and composite microspheres can be produced without solvents, process liquids, or additives by using superamphiphobic layers.

Motivations

Since in the meantime the mechanism of superhydrophobicity is well-understood, several methods have been developed to fabricate artificial superhydrophobic surface to achieving self-cleaning property. However for many applications good mechanical stability and optical transparency are required, especially for self-cleaning solar cells. In general, transmittance decreases with increasing roughness, especially if the roughness exceeds the wavelength of light. In general, superhydrophobic surfaces show poor durability. Damage of the coating diminishes its water repellent function, which depends on the micro structure of the surface. For overcome these two main problems, we choose porous silica capsules since they have nano scale roughness and are transparent. I made use of electrostatic self-assembly to form a monolayer of particles on a substrate, optimizing micron scale roughness *vs* transparency. I have shown that transparency of the coating can be as large as 90 %. But still the particles can easily be removed from the surface. Therefore, I introduce a new method to improve the mechanical durability by chemical vapor deposition of tetraethoxysilane. This process chemically binds neighboring particles to each other and to the surface by SiO_2 bridge. After CVD modification the surface shows greatly improved mechanical resistance as verified by sand abrasion and tape peeling.

Another issue for self-cleaning surface is its oil repellency. Most superhydrophobic surface are wetted by oils due to the low surface tension of oil. Even in nature no superoleophobic surface exists. For oil repellency, overhang structures and low surface energy materials are the key factors. Based on this knowledge, researchers developed a few techniques to fabricate overhang structures. In this thesis, I report a completely new strategy to achieve this goal. Inspired by the fractal structure of carbon soot and its good water repellency, I expected that templating carbon soot might be ideal to fabricate oil repellent surfaces. Carbon beads are only physical bonded together and the bonds can even be destroyed by a deposited water droplet. For overcome this problem, I used chemical vapor deposition of tetraethoxysilane is coat the fractal like carbon soot structure with a silica. Placing the coating under high temperature in air or O_2 plasma, the carbon converted to CO_2 and evaporated, leaving a hollow silica network behind. After fluorination, the surface shows highly oil repellency and transparency.

This superamphiphobic surface, opens new possibilities to design chemical or physical experiments. In this thesis we studied the dynamics of ethanol-water and glycerin-water mixtures

to investigate the effect of surface tension and viscosity on pinning, spreading and retraction during drop impact.

Superamphiphobic surface repel low surface tension organic liquids, monomers as well as polymer melts. These liquids form spherical drop when deposited on the superamphiphobic coating. I showed that spherical micro particle can be fabricated on superamphiphobic coatings without using solvents.

Chapter 1: Introduction of superhydrophobicity and superamphiphobicity

1.1   Wetting behaviour on a solid surface

The wetting behaviour of a liquid on a solid surface can be experimentally characterized by depositing a liquid drop on the surface and measuring the contact angle (Figure 1.1).

In general, when the contact angle is less than 90°, the solid surface is considered as hydrophilic; when the contact angle is larger than 90°, the solid surface is considered as hydrophobic. For the lowest surface free energy of the solid-air interface material a contact angle of ~ 120° has been recorded for water. [1]
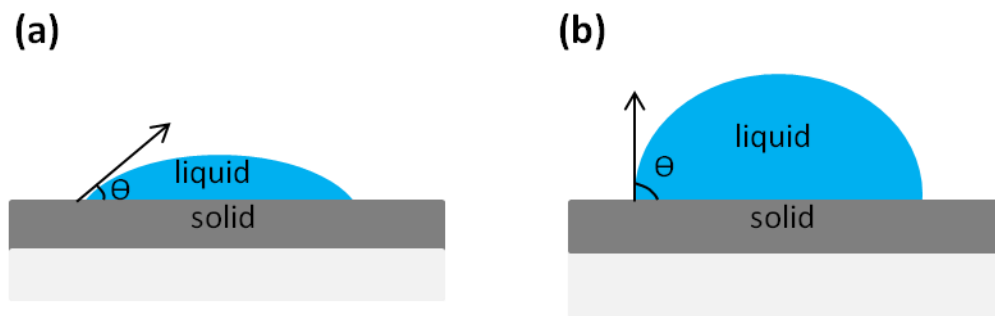

Figure 1.1 Contact angle θ of a water drop on a hydrophilic (a), and on a hydrophobic surface (b).

1.1.1   Wetting on smooth surface

For a smooth and chemically homogeneous solid surface, the contact angle θ of a drop can be calculated theoretically by the Young's equation,

$$\cos\theta = \frac{\gamma_{SV} - \gamma_{SL}}{\gamma_{LV}} \qquad (1)$$

where γ_{SV} is the solid-vapour interfacial energy; γ_{SL} is the solid-liquid interfacial energy and γ_{LV} is the liquid-vapour interfacial energy. The boundary three phases contact line is schematically illustrated in Figure 1.2.
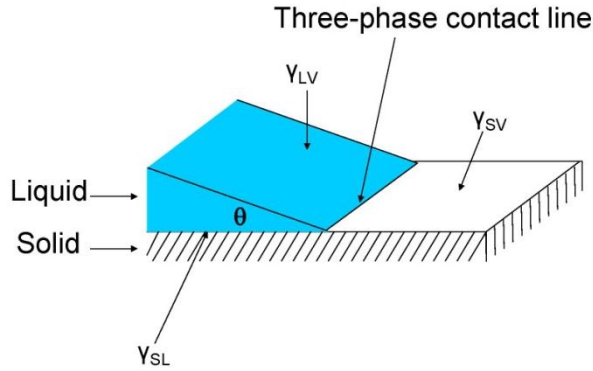

Figure 1.2 Sketch of the three phase contact line of a water drop on a solid surface. (Reprinted from ref[2]).

The molecules are energetically favourable to be surrounded by other molecules. Compare with the bulk, at the surface, molecules are only partially surrounded by other molecules, this is energetically unfavourable. The energy require to take the molecular from the bulk to the surface to create a new surface is so called "interfacial energy". If the interfacial energy is higher than that of the solid-liquid interface ($\gamma_{SV} > \gamma_{SL}$), the right side of the Young's equation is positive. As a consequence, the value of the contact angle will be in the range of 0° to 90°, which means the liquid partially wet the surface. When the $\cos\theta$ is negative ($\gamma_{SV} < \gamma_{SL}$), the contact angle exceeds 90°, the liquid is said not to wet the solid. Among the three interfacial energies, only γ_{LV} can be measured experimentally, using various methods, including capillary rise and pendant drop. No well-established technique exists to measure γ_{SV} and γ_{SL}, separately. The Young's equation only works for flat surface, when the surface become rough, the Young's equation is not suitable anymore.

1.1.2   Wetting on rough surface: Wenzel's and Cassie's models

According to Eqn (1), the surface hydrophobicity increases with decreasing the surface free energy of the solid-air interface γ_{SV}. Further increase of the hydrophobicity requires manipulation of the surface topography. The fact that roughness can strongly affect the wetting of a surface was already discussed by Wenzel in 1936[3] and then by Cassie and Baxter in 1944[4].
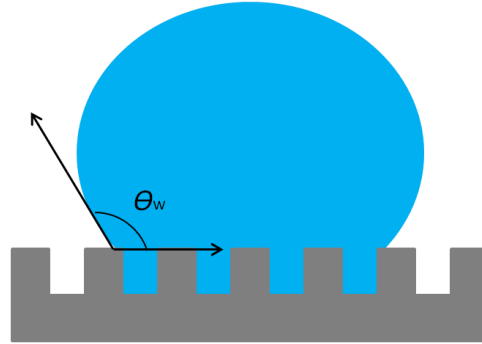
Wenzel's Model

Figure 1.3 Sketch of a water drop on a rough surface in case water penetrates the asperities (Wenzel model).

In the Wenzel state, the drop deposited on a surface and the bottom of the drop penetrates into the asperities (Figure 1.3), the increase of the surface roughness (due to the presence of the texture) amplifies the natural hydrophobicity or hydrophilicity of the material. Thus the key parameter controlling the contact angle θ_w on the same material is the solid roughness. The apparent contact angle on such rough surface can be described by the Wenzel equation:

$$\cos\theta_w = r\cos\theta \qquad (2)$$

where θ_w is the apparent contact angle, this angle we can observe by eye or an optical microscope; and r defined as the ratio between the true surface area over the projected area, the roughness factor is always larger than 1 for a rough solid surface; θ is the contact angle of the corresponding smooth surface obtained by the Young's equation.

For a given hydrophilic surface ($\theta < 90°$), liquid drop has lower contact angle on rough surface compared with corresponding smooth one. If the surface essentially is hydrophobic ($\theta > 90°$), liquid drop has higher contact angle on rough surface compared with corresponding smooth one.

However, *Periklis Papadopoulos* et al found that the contact angle in Wenzel state is not always the same, if the substrate has regular periodic array. So the pillar distance is different at main axis and diagonal axis. The water contact line pinning at the pillars which has different pillar distance will induce different curvature at the bottom of the drop. The drop shape asymmetry factor is decreasing with increase the distance from the substrate.[5]

Cassie's Model

As the surface roughness or the surface hydrophobicity increases, it becomes unlikely for water to completely follow the surface topography of a hydrophobic substrate. Since if water has a complete contact with the solid surface, at this system it is in a high energy state. In the other state, if the water is only partial contact with solid, it is more energy favourable. Instead, air may be trapped between water and the surface texture (Figure 1.4).
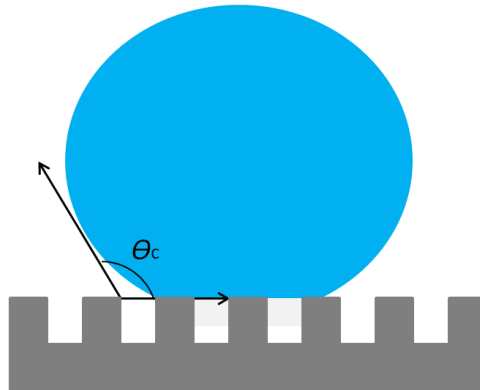
Figure 1.4 A water drop suspended on a rough surface, with air trapped bewteem asperities (Cassie model).

The apparent contact angle for this vapour-liquid-solid composite interface is the sum from all contributions of the different phase fractions. The minimum interfacial energy, together with Young's relation applied to each solid surface, result to Cassie-Baxter relation:

$$\cos \theta_c = f_1 \cos \theta_1 + f_2 \cos \theta_2 \qquad (3)$$

Here θ_c is the apparent contact angle, θ_1 and θ_2 are the contact angles on two different kinds of materials; f_1 and f_2 is the surface fraction of materials 1 and 2, respectively. If the liquid would

12

fully rest on air, the ''contact angle'' would be 180°: the smaller f_{solid}, the closer to this extreme situation, and the higher the contact angle. More precisely, the contact angle θ_c of such a ''fakir'' drop is an average between the angles on solid, and on air. For air $\cos(180°)$= -1, and $f_2 = (1 - f_1)$, the equation (3) can be rewritten as follow[6]:

$$\cos\theta_c = f_1(1 + \cos\theta - 1) \qquad (4)$$

Here f_1 represents the solid-liquid fractions under the contact area; θ is the contact angle on flat surface. This implies for achieve a high apparent contact angle, the contribution from solid phase, should be as small as possible.

1.1.3 Wenzel – Cassie transition

Most likely the transition from the Cassie state to Wenzel state is an irreversible process, since the droplet in Wenzel state is more energy favourable. The detail calculation was discussed by *Barbieri* et al.[27] Cassie to Wenzel transition could be spontaneous or induced by many ways. For instance, drop impacting from a certain height, applying external pressure on a droplet or water column, evaporation of droplet, vibrating the substrate.

For pressure induced transition there are two possible mechanisms.

Figure 1.5 Schematic of the curvature of liquid / air interface between two pillar pattern. The liquid is suspended on the top of the pillar, without external pressure the liquid surface is flat. When pressure is applied, the contact line moves down and form a curved surface. (Reprinted from ref[7])

Sag impalement. When the liquid droplet sets on the pillar surface, the regular circular pillars with diameter R, pitch a as show in figure 1.5. If the pillars are high ($H > a/\sqrt{2}$), the sag pressure is related the maximum pressure allowed by the geometry conformation. The largest possible curvature for a square lattice is around $a\sqrt{2}$. The curvature of the interface in governed by the Laplace equation, and the curvature is the same at the top and at the bottom of the droplet. So the maximum pressure can be calculated as: [7]

$$P = \frac{4}{\sqrt{2}} \frac{\gamma}{a} \qquad (5)$$

Here γ is the interfacial tension of liquid and air. If $H < a/\sqrt{2}$, the liquid interface can easily touch the bottom of the substrate and induce transition. The lower limiting pressure can be calculated as: [7]

$$P = \frac{8\gamma H}{a^2 + 2H^2} \qquad (6)$$

Depinning induced impalement. The maximal force to keep the liquid / air interface on the pillar without sliding down and depinning is governed by the capillary force. Here we assume the liquid / air interface having rotational symmetry, and the capillary force can be calculated as:

$$F_c = 2\pi\gamma R \sin\alpha \sin(\theta_a - \alpha) \qquad (7)$$

α is the contact angle of liquid on particle, θ_a is the liquid advancing angle on pillar. When $\alpha = \theta_a/2$, the force reaches the maximum value and equation (7) can be expressed as follow

$$F_c = 2\pi\gamma R \sin^2\frac{\theta_a}{2} \qquad (8)$$

Here if we assume the radius of the pillar is 500 nm, the advancing angle of water is 120°, the roughly calculated adhesion force for a single nano asperity is around 170 nN. In the mechanical equilibrium state, the capillary pressure is equal to F_c/A, here A is the projected area of liquid / air interface on pillar. Different projected area can be defined, for square lattice shape $A = a^2$. For hexagonal shape $A = a^2\sqrt{3}/2$. The depinning pressure on pillar is described as

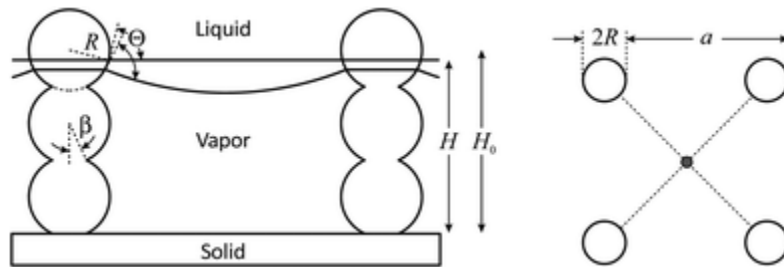$$P = \frac{2\pi\gamma R}{A} \sin^2\frac{\theta_a}{2} \qquad (9)$$
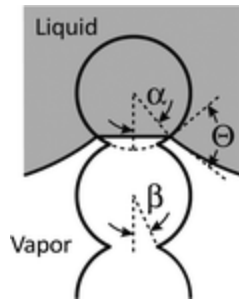
Figure 1.6 Schematic of the curvature of liquid / air interface between two pillar pattern. The liquid is suspended on the top of the pillar, without external pressure the liquid surface for water is flat, for low surface energy liquid, it shows a little curvature. When pressure is applied, the contact line moves down and form a more curved surface. (Reprinted from ref[7])

1.1.4   Contact angle hysteresis
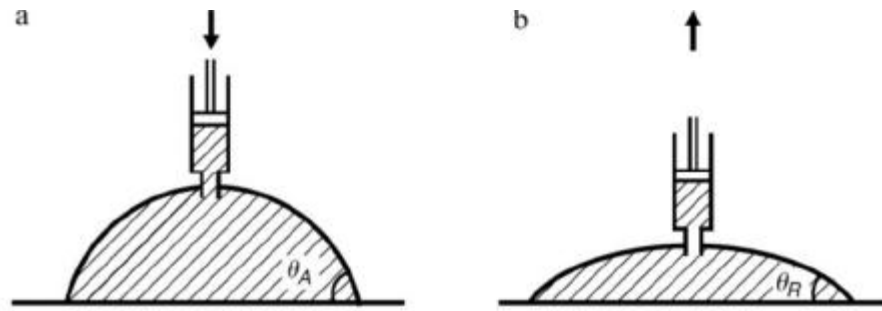
Figure 1.7 (a) Advancing angle when the drop is inflated; (b) receding angle when the drop is deflated. (Reprinted from ref[8]).

Traditionally the static contact angle has been use to quantify the wettability, adhesiveness, and solid surface free energy. Increasing or decreasing the volume of a sessile drop and monitoring the contact angle is a giving way to describe the contact angle hysteresis. It depends on the liquid drop and the solid surface. The largest possible drop that can stay without increasing the interfacial area between the drop and solid, this contact angle referred to as the advancing angle (θ_a). Similarly, as volume is removed from the drop, the contact angle formed just before the

15

drop recedes is referred to as the receding angle (θ_r). The difference between the advancing and receding contact angle is defined as the contact angle hysteresis (Figure 1.7). In general, the advancing angle is higher than the receding angle. The static contact angle can help us to understand the total surface energy of the substrate. And contact angle hysteresis can help us to understand surface roughness, chemical inhomogeneity, the effect of chemical or geometrical defects and the adsorption and desorption of liquid molecules while spreading and receding.

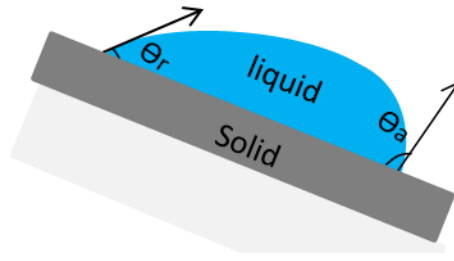**Figure 1.8** Sketch of a plan view of a liquid sliding on a tilted solid surface.

Sliding angle, is defined as the minimum tilting angle before the droplet starts to slide off, this dynamic angle can also be used to characterize the wettability of a solid surface[9]. Increasing the tilt angle of the solid substrate, (Figure 1.8) the right side angle (advancing contact angle θ_a) will increase and the left side angle (receding contact angle θ_r) will decrease. At the moment when liquid starts to slide, the contact angle hysteresis can be defined as: $\theta_{hysteresis} = \theta_a - \theta_r$. At low adhesion surface the water intend to roll off instead to slide down a surface, because the contact line of the liquid can easily depinning from the substrate. On textured surface, a liquid has high contact angle hysteresis if it is in the Wenzel's state (the roll off is generally above 20°) and small contact angle hysteresis in Cassie's state (the roll off angle is less than 10°). In a special Cassis's state air pockets are inside of the structure but still the drop has a very high roll off angle. This can be the case if the microstructure roughness has strong interaction with the water droplet, and the local contact line is strongly pinned on the top of the microstructure.[10]

Generally, superhydrophobicity is defined as follow: a water droplet has a static contact angle above 150° with the surface and a roll off angle of less than 10°. A superhydrophobic surface is always in the Cassis's state, but a Cassis state needs not to be superhydrophobic.

1.2   Special wetting: superhydrophobicity

1.2.1   Experimental approaches to fabricate superhydrophobic surface

During the last few decades, many artificial self-cleaning surfaces were fabricated by different techniques. All original designs were inspired by the "lotus leaf", fist discussed by W. Barthlott in 1997. For the first time W. Barthlott studied the interdependence between surface roughness, surface energy and water repellency.
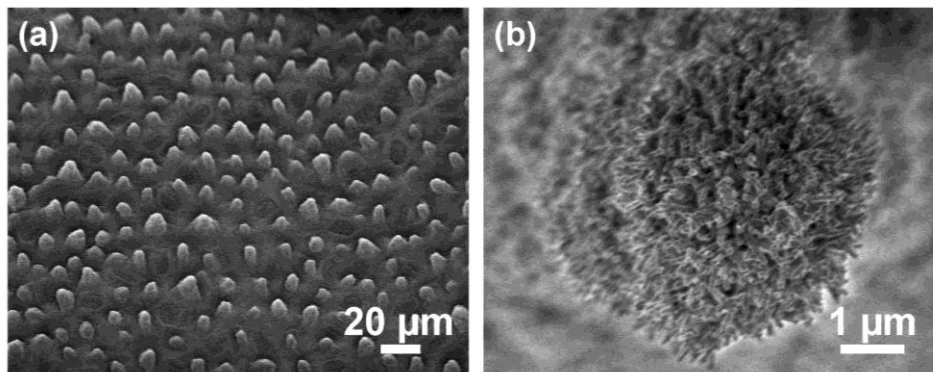
Figure 1.9 SEM images of lotus leaf surface at low magnification (a) and high magnification (b). (Reprinted from ref[11]).

The most well-known self-cleaning surface in nature is the lotus leaf. Water has a contact angle above 150° and rolls-off easily. A close look of the surface by SEM (Figure 1.9) shows that the surface has a complex micro- and nanoscopic architecture, also the entire surface is covered by a low surface energy wax. The combination of dual scale roughness and low surface energy material minimizes the adhesion of water on its surface. Based on this mechanism, there are many approaches to mimic the lotus leaf to create superhydrophobic surfaces. The design principles and fabrication methods are described below, also the advantages and disadvantages are briefly discussed.

Templating technique

Templating is a direct way to replicate 2D or 3D patterns or shapes of a surface. The main idea is: cover the to be template surface with a suitable material, typically a polymer, press to improve the contact and remove the solidified material from the template.
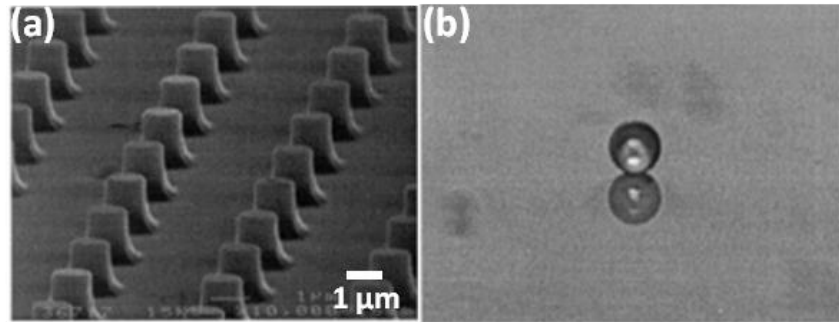
Figure 1.10 (a) Replica surfaces produced by templating a micro pillars morphology. (b) Water droplet on the corresponding surface, the contact angle is about 167°. (Reprinted from ref[12])

In 1999, D. Quéré *et al* used photolithography to fabricate a mask surface which only has micro pillar features. The entire structure of the mask was then replicated using an elastomeric mould, which was subsequently used to cast silica features onto a silicon wafer. Followed by coating a hydrophobic monolayer on those pillars, the pillar surface showed a static contact angle of 167° with water[12].
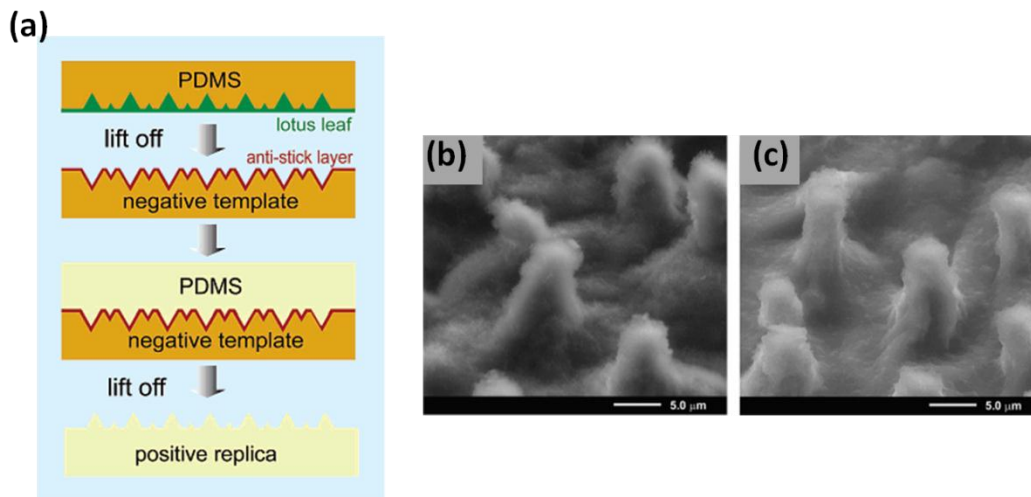
Figure 1.11. (a) Scheme of the lotus leaf replication step and creation of a superhydrophobic surface. Higher magnification SEM images of (b) the lotus leaf and (c) its positive replica. Both have a similar surface morphology. (Reprinted from ref[13])

In 2005, Yong Chen *et al*. casted a PDMS or PMMA polymer solution on a lotus leaf surface. After solidification the PDMS at room temperature for 24 h, the layer was peeled off. The texture of the original lotus leaf was transferred to the negative template. Then, a second replication of PDMS was performed on the negative template in the same procedure as the previous process. SEM images (Figure 1.11) showed that the lotus leaf structure was templateed by the PDMS surface. This rough PDMS surface has a static contact angle above 155° and a roll off angle of less than 2°[13].

Templating is a useful technique to replicate the structure texture. It is a direct way to mimetic and copy the original structure. However, this method is not suitable for many materials, especially for inorganic materials and metals. Furthermore it is difficult to replicate large surfaces.

Aggregation/assembly of colloids

Rough surfaces can also be formed using colloidal particles. The particles stick together utilizing the attractive Van der Waals forces, electrostatic forces between particles and particles to the substrate.

W. Ming *et al* report a simple way to prepare superhydrophobic films with dual-size hierarchical structure originated from well-defined raspberry-like particles. The fabrication step is sketched in Figure 1.12a. First, a conventional cross-linked film based on an epoxy-amine system is prepared with uncured epoxy groups available for further surface grafting. Then, raspberry-like silica particles functionalized by amine groups are deposited onto the epoxy films. The surface topography could be controlled by the deposition parameters. This method generates a double-structured roughness on the epoxy film. Finally, a low surface energy layer of monoepoxy end capped poly(dimethylsiloxane) is grafted onto the raspberry-like particles to render the film surface hydrophobic. The raspberry like particle has two-level roughness, the micro scale roughness is contributed by the large silica particles forming the core of the raspberry-like particles, whereas on each of the micro scale structures there is a nano scale silica bead, that supplied the second roughness (Figure 1.12b). This dual scale hierarchical structure resembles the surface of a lotus leaf. It has a static contact angle of 154° and a roll off angle less than 3°.[14]

The advantage of particle aggregation method is that it can easily achieve both nano and micro scale roughness in a conformal and controlled way. However the interaction of the particles itself and the adhesion of the aggregated particle to the substrate are quite weak. Due to the random roughness, the transparency of the coating is usually low.
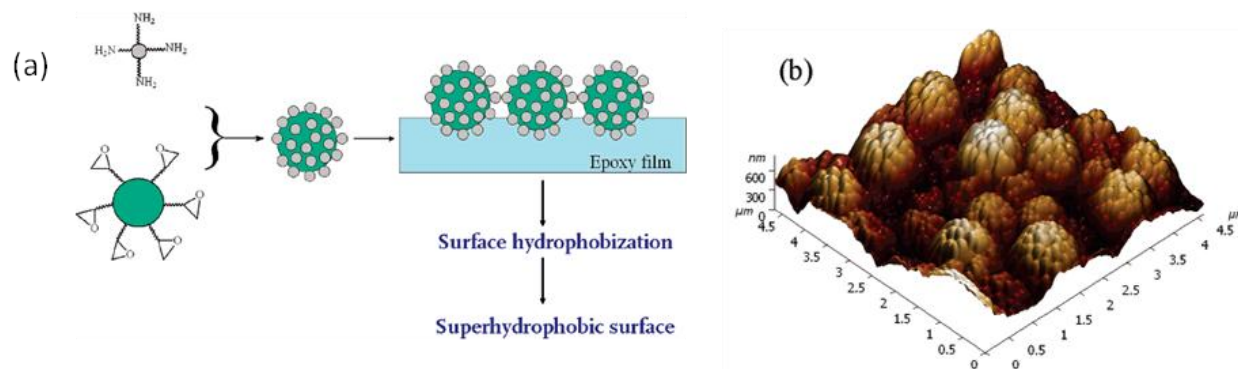
Figure 1.12 Preparation of superhydrophobic films based on raspberry-like particles (b) AFM 3D images for PDMS-covered epoxy-based film containing raspberry-like particles. (Reprinted from ref[12])

Etching nanograss

Plasma-based etching processes form an efficient way to roughen the surface by polishing the surface matrix. Due to the different reaction rate of the matrix substance to plasma, it can generate micro or nano roughness in a single step. J. P. Fernández-Blázquez *et al* reported that treating polyethylene terephthalate (PET) films by oxidative plasma allows to fabricate isolated nanofibrils and fibril bundles. With increasing etching ratios, the transition from fibrils to bundles was smooth and it was associated with a significant reduction in the overall top area fraction. When the etching time increased to 20 minutes a second organization level of roughness started to develop (Figure 1.13). Depending on the surface chemistry, after oxygen plasma treatment the films are hydrophilic and have a CA of 0°. This can be attributed to the incorporation of polar oxygen atoms to the surface during plasma treatment. However after storage for 25 days, the bulk polymer chains can diffuse to the surface and decrease the surface energy. As a consequence the nanograss PET film becomes superhydrophobic.

The advantage of this method is that it can generate uniform roughness at large scale. But it is quite energy consume and expensive.
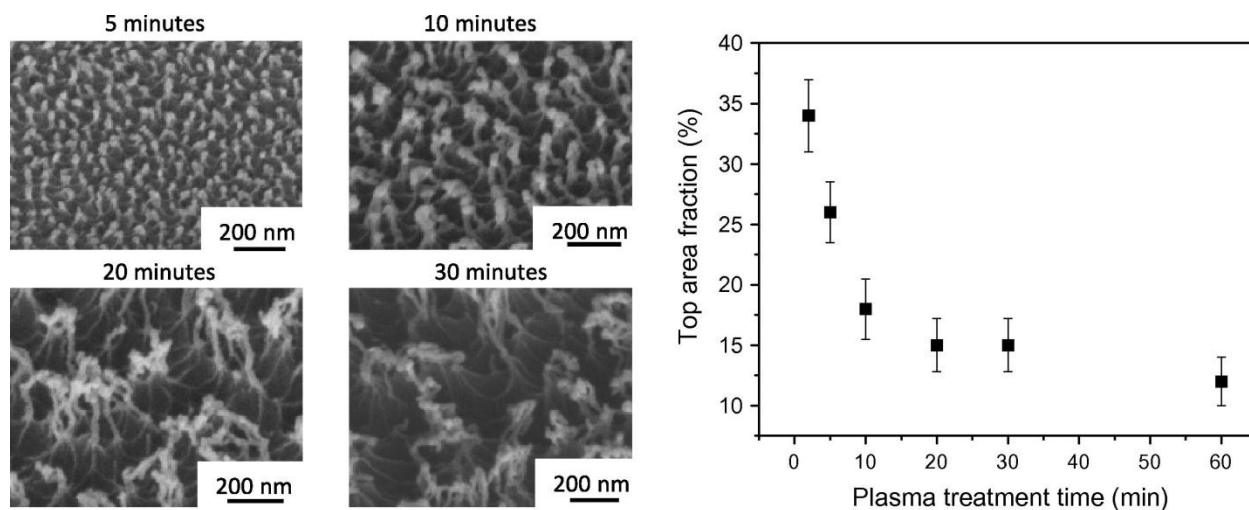
Figure 1.13 SEM images of the surface morphology of PET samples that were plasma treated for different times. The graph on the right side represents the top area fraction of the fibrils in these samples calculated from the SEM images (Reprinted from ref[15])

Electrospinning of fibers

Electrospinning has become a popular method to generate continuous ultrathin fibers with micrometer and sub-micrometer diameters from a variety of polymeric materials. Tuning the spinning materials and parameter, different scales of roughness can be achieved to create a superhydrophobic surface. Figure 1.14a illustrates the water/air/solid composite interface on fiber with different surface roughness. Fibers with concave and convex sub-scale roughness have less contact with water compare to fibers with smooth surface. M.L. Ma *et al* reported a way to fabricate porous poly(methyl methacrylate) (PMMA) fibers with an average fiber diameter of 1.7 μm by electrospinning from a chloroform solution, the ambient humidity is controlled at 44% humidity (Figure 1.14b). After coating a thin conformal PPFEMA layer by iCVD, the surface energy was decreased. Water drops have a contact angle of 163°.
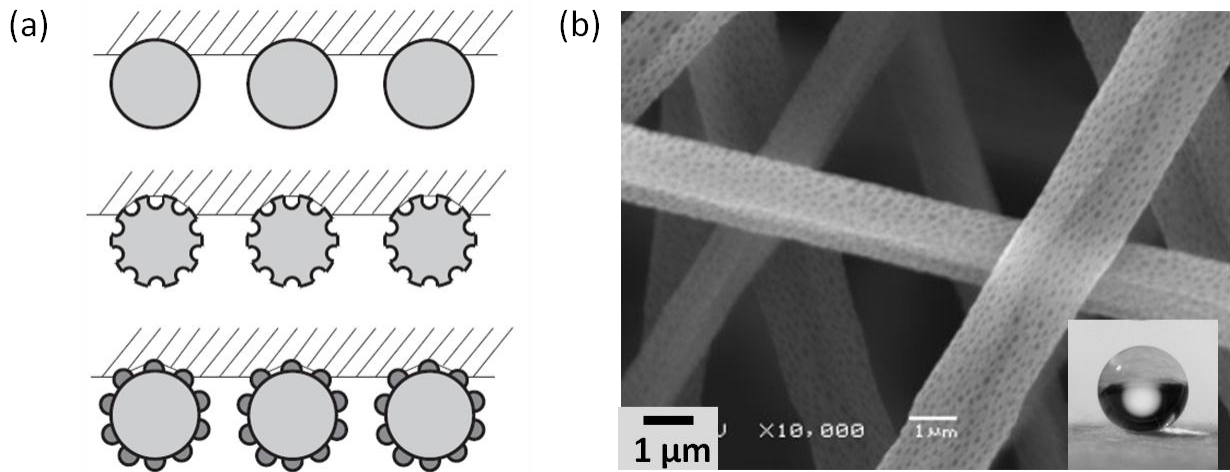
Figure 1.14 (a) Schematic representations the interface of the water/solid/air 3 phase contact line with different fibers surface morphology. The fibers are parallel and have a circular cross section. Their axes normal points to the page. The hatched region represents a portion of the water droplet lying on the fiber. (b) SEM images of as-spun porous PMMA fibers. (Reprinted from ref[16])

Electrospinning of fibers is an industrial applicable way to fabricate self-cleaning surface, but the ideally substrate for coating is on textile. Also the fibers are leak of optical property and thermal stability.

Lithography

In photolithographic approaches, a photoactive polymer layer is irradiated by light which passes through a featured mask. Subsequent developing and etching steps yield the desired patterned surfaces. Radiation source include UV, X-ray and e-beam. **N. J. Shirtcliffe** *et al* reported a lithography method by using SU-8 as photoresist, through controlling the mesh feature and the thickness of SU-8 layer. The wettability of the pattern surface can be tuned by changing the pillar height and diameter, as well as the distance between the pillars.(Figure 1.15)

(a)   (b)
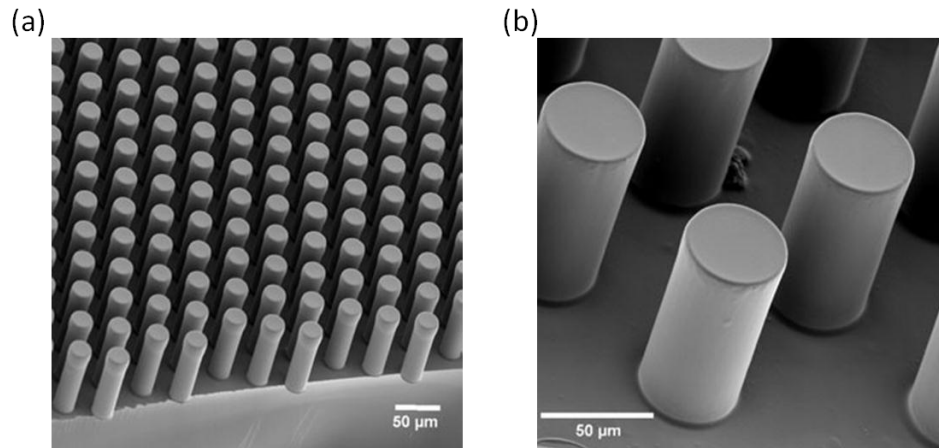
Figure 1.15 SEM of patterned SU-8 surfaces at different magnification (a) (Reprinted from ref[17])

Lithographic techniques can generate small, well-defined and uniform structure. This allows to design model surfaces to test and develop theories to improve the theoretical understanding of wetting. . However for industrial application, surfaces need to be processed fast, in large scale and cheap. This limits industrial applications of lithography to high end products.

Phase separation

A   B
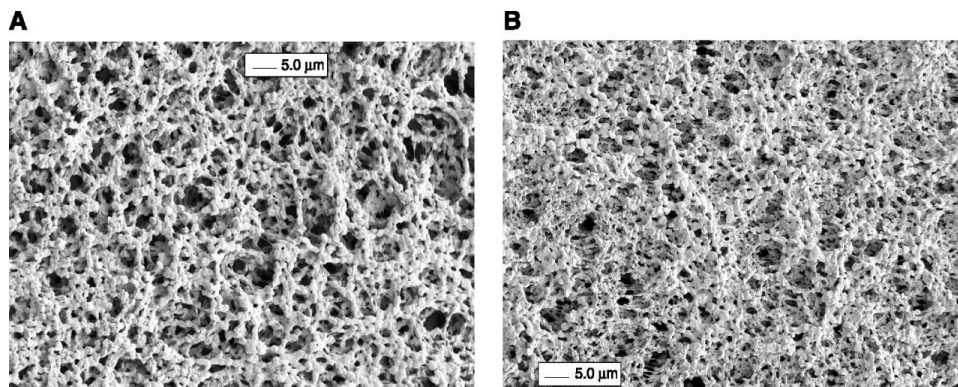
Figure 1.16 SEM pictures of i-PP obtained from a solution (20 mg/ml) in p-xylene on glass slides at drying temperatures of (A) 30°C and (B) 60°C. The i-PP was dissolved in p-xylene at 130°C and the solvent was evaporated in a vacuum oven at the specified temperatures. (Reprinted from ref[18])

Erbil *et al* used isotactic polypropylene (i-PP) for the preparation of superhydrophobic surfaces. They controlled the surface roughness by a suitable selection of solvents and temperature. In these experiments the good solvent p-xylene and the non-solvent MEK mixture was used. A series of samples were tested at different solute concentration, drying temperature, and different solvents. It was found that lowering the drying temperature led to loose network formation, which increased the water apparent contact angle. (Figure 1.16). This approach to form superhydrophobic coatings is simple and inexpensive, since polypropylene is a cheap polymer. By using this technique, a static contact angle of 170° for water is achieved.

Often phase separation of polymer blends results in a rough and porous films. However this method is also designed for organic substance, thus the coating shows poor temperature stability and ages.

1.2.2   Challenges of superhydrophobic surface

As discussed previously, most approaches to fabricate superhydrophobic surfaces are based on certain roughness, and surface is covered by low surface energy material. However, nano roughness can easy be destroyed by external force. Also the adhesion of the coating to the substrate is usually weak. The mechanical stability belongs to the most challenging problem for a self cleaning surface.

For some applications, thermal stability is also quite important. Many superhydrophobic coatings are polymer based. Polymers change their surface morphology when the temperature is above the glass transmission temperature, and the polymer starts to melt. At even higher temperature, the polymer structure even starts to degrade, and superhydrophobicity is lost.

High transparency is would extend the range of possible applications of superhydrophobic surfaces, for instance, window and solar cell. In general, transmittance decreases with increasing roughness, especially if the roughness exceeds the wavelength of light. So reducing the roughness below a certain value (typically less than 100 nm), to achieve high transparency is another challenge.

Impalement in cause of time is a problem for superhydrophobic surface. If the height of the roughness is low, most cases the robustness of the Cassie state is poor.

In possible applications, a deposited liquid drop may have the contaminations on surface, those contaminations will lowering of the surface tension. A drop with reduced liquid-air interfacial tension will penetrate into the structure. This can be sufficient to induce homogeneous wetting of the surface. As a matter of fact, surface that are oil repellent become more and more important.

1.3 Special wetting: superamphiphobicity

1.3.1 Difference between superhydrophobicity and superamiphobicity

Many surface in nature are water repellent, including various plant leaves[19] or water strider legs.[20] However, no natural surface exists which can repel liquids with much lower surface tension than water.
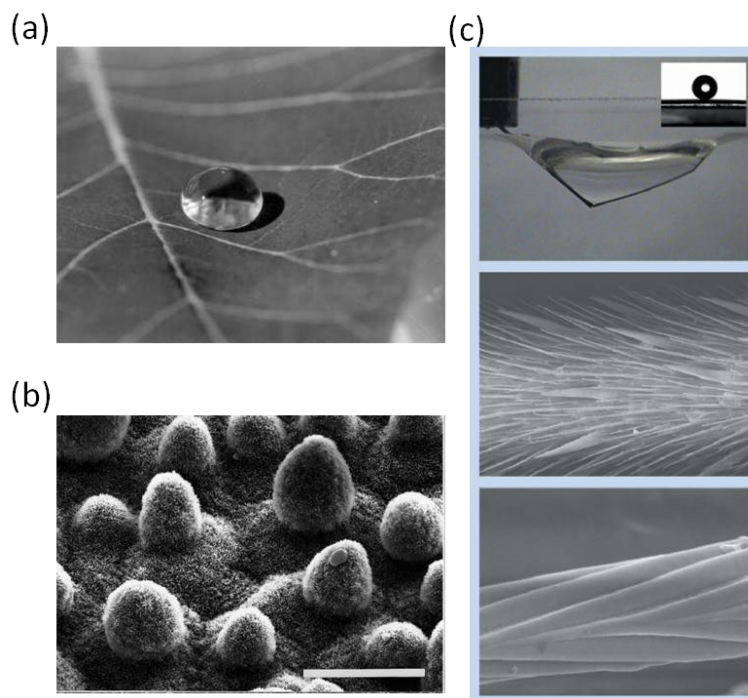
Figure 1.17 (a) A water droplet on a leaf of Cotinus coggygria. (b) SEM of Colocasia esculenta leaf. (c) The non-wetting leg of a water strider. Inset is a water droplet on a leg; this makes a

contact angle of 167 °. SEM images of a leg showing numerous oriented spindly microsetae and the fine nanoscale grooved structures (Reprinted from ref 8, 17, 18)

Superamphiphobic surfaces instead repel organic liquids, in addition to water. To design a superamphiphobic surface it is not sufficient to fabricate a low energy surface with a high roughness on the nano or micrometer scale. The fundamental difference between water and non-polar liquids is the contact angle on flat low-energy surfaces. Water can form a contact angle above 90° with these surfaces. In contrast, no flat surface exists (to our knowledge) that forms a contact angle above 90° with non-polar liquids. In water, mercury, and few other polar liquids, the interaction between the liquid molecules among themselves is so strong, that it requires high energy to create a solid-liquid interface. As a result, $\gamma_{SL} > \gamma_{SV}$ and Θ_0 can be higher than 90°. For organic liquids γ is typically 15 - 40 mN/m. Mainly van der Waals interactions act between the liquid and the hydrophobized substrate. Therefore γ_{SL} is low, $\gamma_{SV} - \gamma_{SL}$ is positive, and $\Theta_0 < 90°$. Thus, to create surfaces with an apparent contact angle above 150° and a low roll-off angle with non-polar liquids, microscopic overhanging structures that prevent the liquid from sliding down the asperities are necessary. (Figure 1.18)

(a)

Water CA on flat hydrophobic surface ~ 108°

Water   Water

Interface of water on textured surface

(b)

Hexadecane CA on flat hydrophobic surface ~ 64°

Oil   Oil

Interface of oil on textured surface
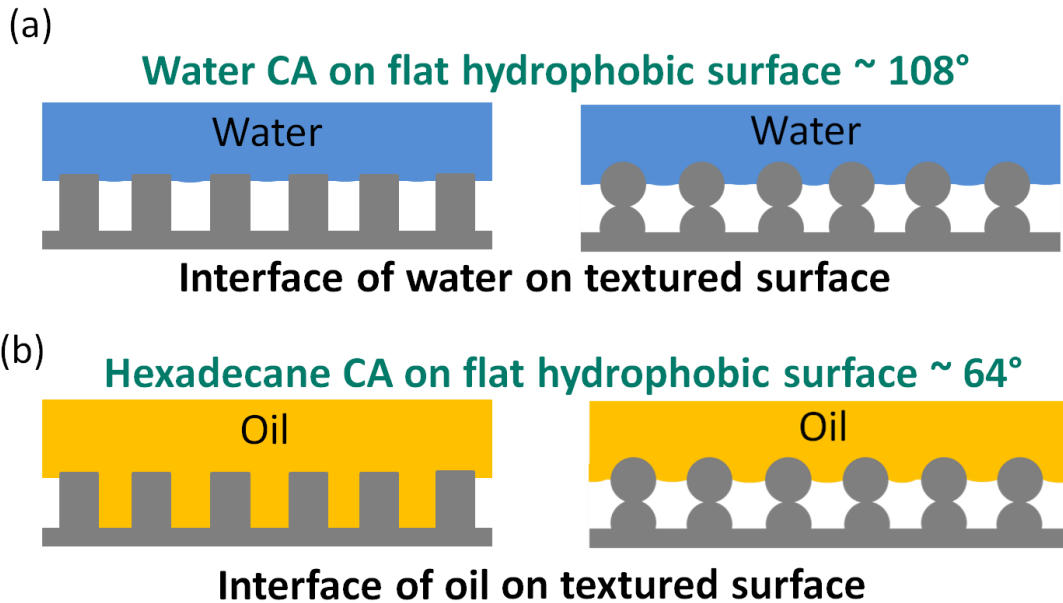
Figure 1.18 (a) A water/solid/air composite interface on different topography surface. (b) A oil/solid/air composite interface on different topography surface. The hydrophobic surface is fabricated by fluorination.

1.3.2   Experimental approaches to fabricate superamiphobic surfaces

Superhydrophobic surface require low surface energy materials and rough morphology, for superamphiphobic surface one additional key factor is required: overhang structure. Taking into account these requirements, many techniques have been developed to fabricate surfaces that are both, water and oil repellent[d21a, 21b-h]. In the following, I will discuss the progress steps of fabrication superamphiphobic surface. And introduce the fabrication technique and discuss their advantage and disadvantage.

In 1997, Kaoru Tsujii *et al* first successfully fabricated a surface which has a contact angle of 151° for oil droplet. They modified the surface morphology of an aluminium plate by anodic oxidization (Figure 1.19). Subsequently they grafted a fluorinated monoalkylphosphates to lower the surface energy.[22] The surface repels liquids which have a surface tension above 40 mN/m.

(a)

(b)
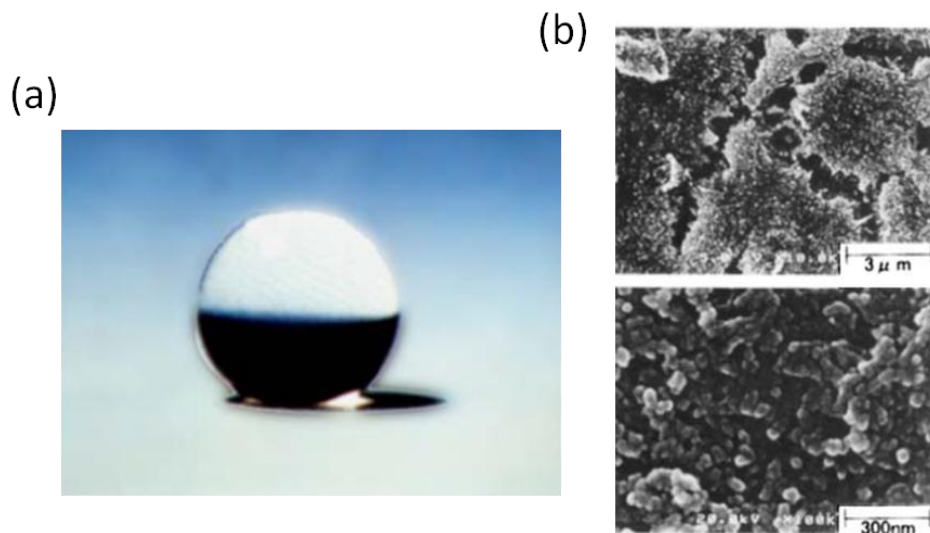
Figure 1.19 (a) A picture of a rapeseed oil droplet. The oil droplet rolls around even if the surface is tilted only slightly. (b) SEM images taken at two different magnifications, showing an anodically oxidized aluminum plate surface. (Reprinted from ref 20)

Anish Tuteja *et al* synthesized a class of hydrophobic polyhedral oligomeric silsesquioxane (POSS) molecules in which the rigid silsesquioxane cage is surrounded by perfluoro-alkyl groups. The surface energy of the matrix can be systematically changed by varying the mass fraction of fluoroPOSS molecules blend with PMMA (Figure 1.20a). After electrospinning, the fluoroPOSS molecular form fiber structure. The advancing and receding contact angle for hexadecane on this oleophoic surface is show in figure 1.20b. In this paper they also discussed the mechanism of overhang structure, discussing why overhangs can repel low surface tension liquid. However fibrous structure has a continues solid phase, which has much more contact area compare with isolate solid phase.
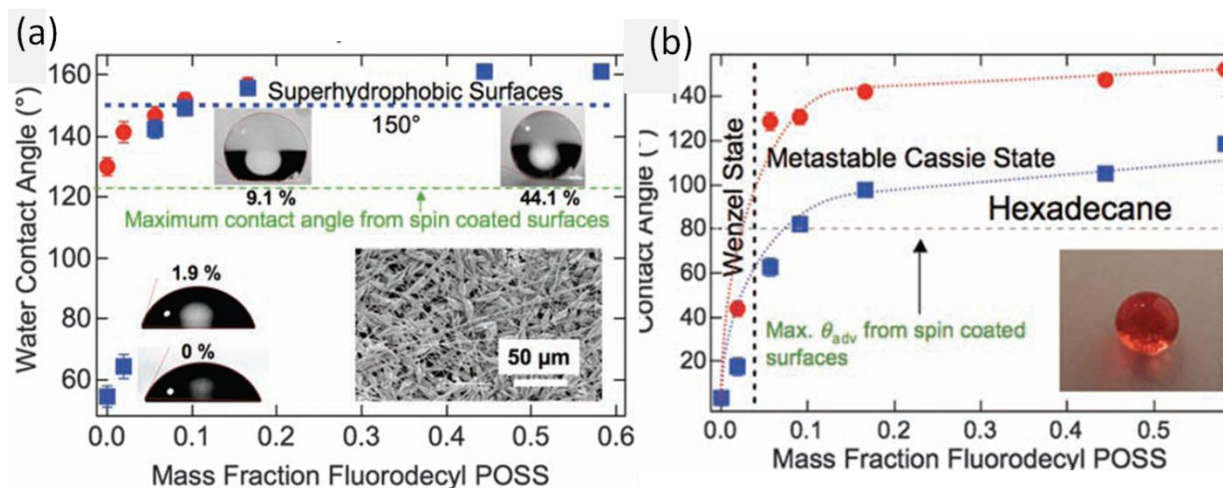
Figure 1.20 (a) Advancing contact angle and receding contact angle for water as a function of the mass fraction of fluorodecyl POSS. The inset shows the general molecular structure of fluoroPOSS molecules. (b) Advancing contact angle and receding contact angle for hexadecane, respectively, on the electrospun surfaces. The inset of (b) shows a drop of hexadecane (dyed with Oil Red O) on a 44 weight % fluorodecyl POSS electrospun surface. (Reprinted from ref[23])

Adam Steele *et al* fabricated a superoleophobic coating by spray casting a nanoparticle polymer composite suspensions. They used ZnO nanoparticles mixed with a waterborne perfluoroacrylic polymer solution and cosolvents. Acetone acts as an effective compatibilizing cosolvent to produce self-assembled textured nanocomposites.(Figure 1.21a) Figure 1.21b shows the static contact angle as function of nanoparticle / perfluoroalkyl methacrylic copolymer (PMC) mass fraction. At very high nanoparticle concentration, the polymer is completely coated with nanoparticles, forming a self-similar nanoscale roughness. The mass fraction of 3.3 is ideal for superoleophobicity (NC2) and a mass fraction of 1.7 is ideal for superhydrophobicity (NC1) which results in static contact angles of 157° and 168°, respectively. As can be seen from the SEM pictures, the surface morphology of this coating is not uniform, the distance between the surrounding asperities is varies strongly.
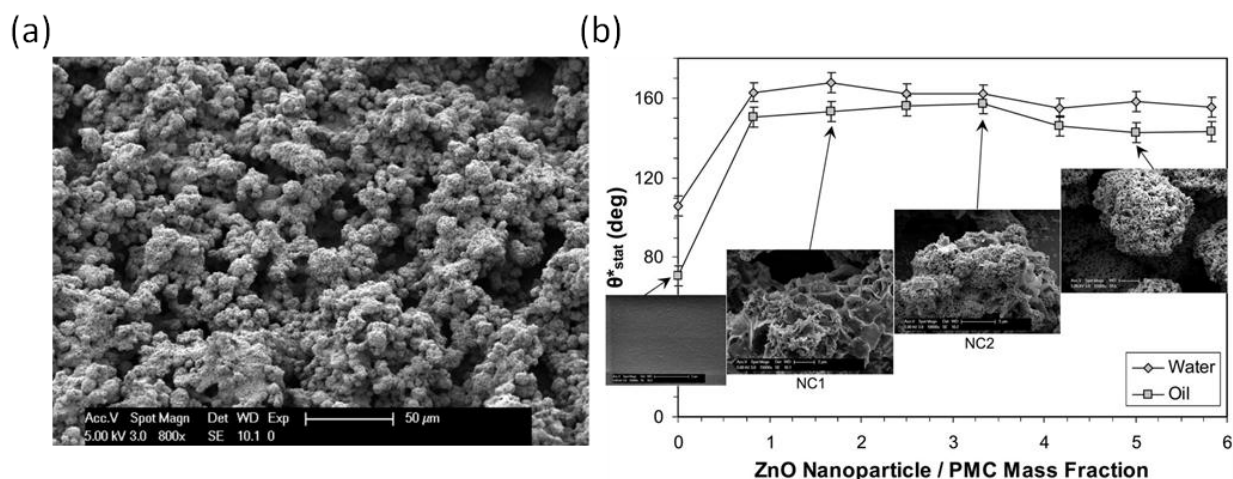
Figure 1.21 (a) Environmental SEM images of nanocomposite coatings showing microroughness and self-similarity. (b) Apparent static contact angle of 10 μL water or oil droplets as a function of different nanoparticle concentrations. (Reprinted from ref[24])

The previous technique to fabricate superoleophobic surface are all based on a combination of the geometry and low surface energy materials. The shape and the properties of the air-solid-liquid composite interface determine the stability of the superamphiphobic state.

In 2011, inspired by the pitcher plant, Tak-Sing Wong and Joanna Aizenberg, also later D. Quere *et al* reported a new mechanism to fabricate slippery surface.[25] The slipper surface also possess very good self-cleaning property compare with traditional superamphiphobic surface, it can

repellent the low surface tension liquid down to 17.1 mN/m. But the mechanism is completely different, liquids on the slipper surface are set on the liquid/liquid/air composite interface. This approach is based on the idea to trap a low surface energy liquid inside a texture. The deposited liquid droplets can float and slide on this composite substrate. Wong et al used a nano/ microstructured porous film as a substrate to lock the infused lubricating fluid (FC-70 which has a low surface energy) (Figure 1.22a). This composite surface repels various simple and complex liquids (water, hydrocarbons, crude oil and blood) and maintains a low sliding contact angle (Figure 1.22b). Since this surface is liquid based, the transparency is very good and it can quickly restore its liquid-repellency after physical damage (Figure 1.23ab). Air is not required as a composite interface. So it can also be used at high pressures (up to about 680 atm). (Figure 1.23c)
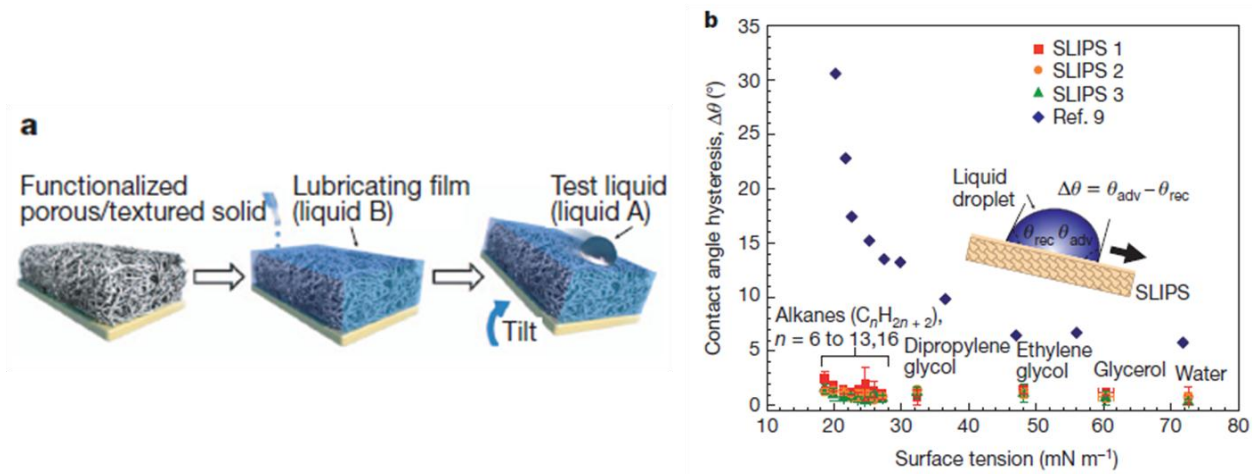
Figure 1.22 (a) Schematics showing the fabrication of a SLIPS substrate. (b) Comparison of contact angle hysteresis as a function of surface tension of test liquids (Reprinted from ref[26])
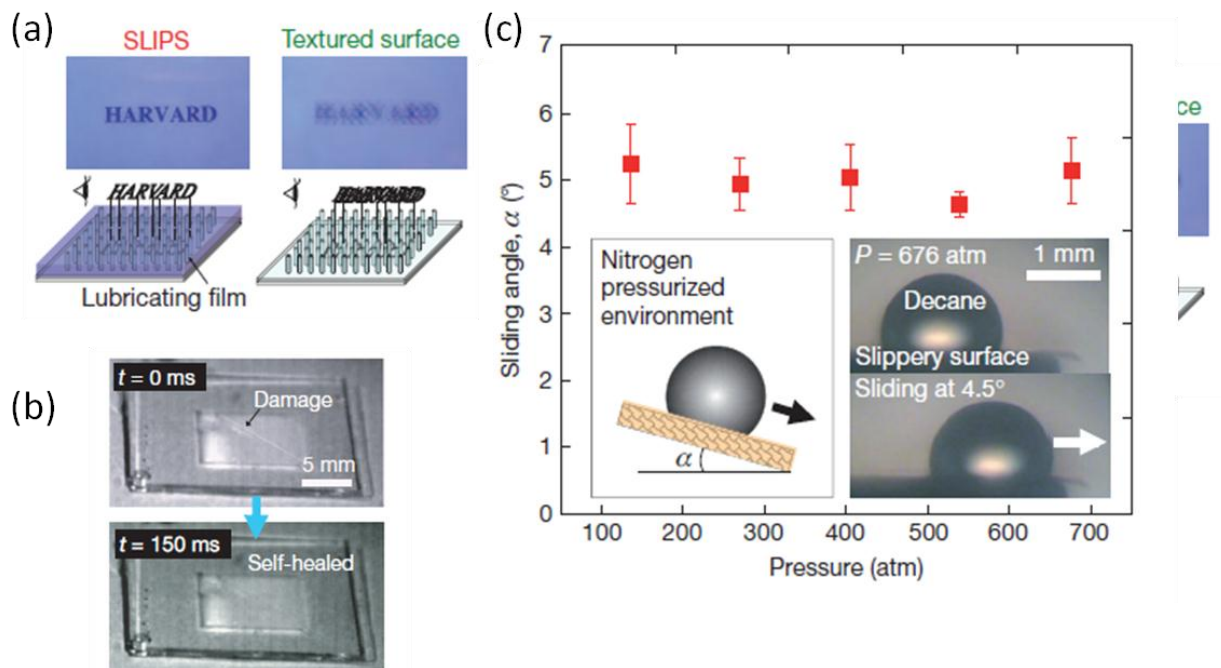
Figure 1.23 (a) Optical images showing enhanced optical transparency of an epoxy-resin-based SLIPS surface (left) as compared to the non-infused superhydrophobic nanostructured surface (right). (b) Time images showing the SLIPS to self-healing from physical damage by knife cutting. (c) The high pressure stability of SLIPS, as evident from the low sliding angle of a decane droplet at different pressure. (Reprinted from ref[26])

Slippery surface opens a new possibility to fabricate oil repellent surface. The liquid based surface has nice self-healing property compared with the solid based oil repellent surface. However there are still spaces for improvement. Titling of the substrate may induce leakage of the liquid. Also the stability of the slippery surface under shear by another liquid flow needs to be investigated.

1.3.3   Challenges of superamphiphobic surface

Although recently researcher understood that overhangs is a key factor to make superamphiphobic surface, still most methods to fabricate oil and water repellent surface are

complicated and expensive. Compared to the fabrication of rough surfaces, it is much more difficult to fabricate overhang structures. Furthermore, for industrial applications the method needs to be reproducible, cheap and scalable. This requires further improvements. So far most materials used to fabricate superamphiphobic surface are polymer based. Polymers have limited thermal stability. But the most challenging factor for industrial application is the mechanical durability of the surface. In general overhang structures show weaker mechanical resistance towards shearing than pillars or pyramidal shapes. During abrasion, not only the structure will change its geometry, but also the surface chemistry may change from hydrophobic to hydrophilic. To expand the range of possible applications of superamphiphobic surface to goggle, window and solar cell the surface needs to be transparent. A fabrication method would be desirable that has the potential to solve all problems which we have mentioned before. In the following chapters, I'm going to present my contribution to solve these problems step by step. Also we try to explore the new application of superamphiphobic surface, for helping understand how the surface tension and viscosity influence the drop impacting dynamics, and for synthesis polymeric micro particles.

Reference

1.   Shibuichi, S.; Yamamoto, T.; Onda, T.; Tsujii, K., Super Water- and Oil-Repellent Surfaces Resulting from Fractal Structure. *Journal of Colloid and Interface Science* 1998, *208* (1), 287-294.

2.   Butt, H.-J.; Graf, K.; Kappl, M., Contact Angle Phenomena and Wetting. In *Physics and Chemistry of Interfaces*, Wiley-VCH Verlag GmbH & Co. KGaA: 2004; pp 118-144.

3.   Wenzel, R. N., RESISTANCE OF SOLID SURFACES TO WETTING BY WATER. *Industrial & Engineering Chemistry* 1936, *28* (8), 988-994.

4.   Cassie, A. B. D.; Baxter, S., Wettability of porous surfaces. *Transactions of the Faraday Society* 1944, *40* (0), 546-551.

5.   Papadopoulos, P.; Deng, X.; Mammen, L.; Drotlef, D.-M.; Battagliarin, G.; Li, C.; Müllen, K.; Landfester, K.; del Campo, A.; Butt, H.-J. r., Wetting on the microscale: Shape of a liquid drop on a microstructured surface at different length scales. *Langmuir* 2012, *28* (22), 8392-8398.

6.   Callies, M.; Quere, D., On water repellency. *Soft Matter* 2005, *1* (1), 55-61.

7.   Butt, H.-J.; Semprebon, C.; Papadopoulos, P.; Vollmer, D.; Brinkmann, M.; Ciccotti, M., Design principles for superamphiphobic surfaces. *Soft Matter* 2013, *9* (2), 418-428.

8.   de Gennes, P. G.; Brochard-Wyard, F.; Quéré, D.; Reisinger, A., *Capillarity and wetting phenomena : drops, bubbles, pearls, waves*. Springer: New York [etc.], 2004.

9.   Furmidge, C. G. L., Studies at phase interfaces. I. The sliding of liquid drops on solid surfaces and a theory for spray retention. *Journal of Colloid Science* 1962, *17* (4), 309-324.

10.   Papadopoulos, P.; Mammen, L.; Deng, X.; Vollmer, D.; Butt, H.-J., How superhydrophobicity breaks down. *Proceedings of the National Academy of Sciences* 2013, *110* (9), 3254-3258.

11.   D'Acunzi, M., *Core-shell Particles and Their Application for Superhydrophobic Surfaces*. 2010.

12.   Bico, J.; Marzolin, C.; Quere, D., Pearl drops. *Europhysics Letters* 1999, *47* (2), 220-226.

13.   Sun, M.; Luo, C.; Xu, L.; Ji, H.; Ouyang, Q.; Yu, D.; Chen, Y., Artificial Lotus Leaf by Nanocasting. *Langmuir* 2005, *21* (19), 8978-8981.

14.   Ming, W.; Wu, D.; van Benthem, R.; With, G. d., Superhydrophobic films from raspberry-like particles. *Nano letters* 2005, *5* (11), 2298-2301.

15.   Fernández-Blázquez, J. P.; Fell, D.; Bonaccurso, E.; Campo, A. d., Superhydrophilic and superhydrophobic nanostructured surfaces via plasma treatment. *Journal of Colloid and Interface Science* 2011, *357* (1), 234-238.

16.   Ma, M.; Gupta, M.; Li, Z.; Zhai, L.; Gleason, K. K.; Cohen, R. E.; Rubner, M. F.; Rutledge, G. C., Decorated electrospun fibers exhibiting superhydrophobicity. *Advanced Materials* 2007, *19* (2), 255-259.

17.   Shirtcliffe, N. J.; Aqil, S.; Evans, C.; McHale, G.; Newton, M. I.; Perry, C. C.; Roach, P., The use of high aspect ratio photoresist (SU-8) for super-hydrophobic pattern prototyping. *Journal of Micromechanics and Microengineering* 2004, *14* (10), 1384.

18.   Erbil, H. Y.; Demirel, A. L.; Avcı, Y.; Mert, O., Transformation of a Simple Plastic into a Superhydrophobic Surface. *Science* 2003, *299* (5611), 1377-1380.

19.   (a) Barthlott, W.; Neinhuis, C., Purity of the sacred lotus, or escape from contamination in biological surfaces. *Planta* 1997, *202* (1), 1-8; (b) Herminghaus, S., Roughness-induced non-wetting. *EPL (Europhysics Letters)* 2007, *52* (2), 165.

20.   Gao, X.; Jiang, L., Biophysics: water-repellent legs of water striders. *Nature* 2004, *432* (7013), 36-36.

21.   (a) Liu, M.; Wang, S.; Wei, Z.; Song, Y.; Jiang, L., Bioinspired design of a superoleophobic and low adhesive water/solid interface. *Advanced Materials* 2008, *21* (6), 665-669; (b) Im, M.; Im, H.; Lee, J.-H.; Yoon, J.-B.; Choi, Y.-K., A robust superhydrophobic and superoleophobic surface with inverse-trapezoidal microstructures on a large transparent flexible substrate. *Soft Matter* 2010, *6* (7), 1401-1404; (c) Jin, H.; Kettunen, M.; Laiho, A.; Pynnönen, H.; Paltakari, J.; Marmur, A.; Ikkala, O.; Ras, R. H., Superhydrophobic and superoleophobic nanocellulose aerogel membranes as bioinspired cargo carriers on water and oil. *Langmuir* 2011, *27* (5), 1930-1934; (d) Joly, L.; Biben, T., Wetting and friction on superoleophobic surfaces. *Soft Matter* 2009, *5* (13), 2549-2557; (e) Zhang, J.; Seeger, S., Superoleophobic coatings with ultralow sliding angles based on silicone nanofilaments. *Angewandte Chemie International Edition* 2011, *50* (29), 6652-6656; (f) Wang, H.; Xue, Y.; Ding, J.; Feng, L.; Wang, X.; Lin, T., Durable, Self-Healing Superhydrophobic and Superoleophobic Surfaces from Fluorinated-Decyl Polyhedral Oligomeric Silsesquioxane and Hydrolyzed Fluorinated Alkyl Silane. *Angewandte Chemie International Edition* 2011, *50* (48), 11433-11436; (g) Srinivasan, S.; Chhatre, S. S.; Mabry, J. M.; Cohen, R. E.; McKinley, G. H., Solution spraying of poly (methyl methacrylate) blends to fabricate microtextured, superoleophobic surfaces. *Polymer* 2011, *52* (14), 3209-3218; (h) Yang, J.; Zhang, Z.; Xu, X.; Zhu, X.; Men, X.; Zhou, X., Superhydrophilic–superoleophobic coatings. *Journal of Materials Chemistry* 2012, *22* (7), 2834-2837.

22.   Tsujii, K.; Yamamoto, T.; Onda, T.; Shibuichi, S., Super Oil-Repellent Surfaces. *Angewandte Chemie International Edition in English* 1997, *36* (9), 1011-1012.

23.   Tuteja, A.; Choi, W.; Ma, M.; Mabry, J. M.; Mazzella, S. A.; Rutledge, G. C.; McKinley, G. H.; Cohen, R. E., Designing superoleophobic surfaces. *Science* 2007, *318* (5856), 1618-1622.

24.   Steele, A.; Bayer, I.; Loth, E., Inherently superoleophobic nanocomposite coatings by spray atomization. *Nano letters* 2008, *9* (1), 501-505.

25.   Lafuma, A.; Quéré, D., Slippery pre-suffused surfaces. *EPL (Europhysics Letters)* 2011, *96* (5), 56001.

26.   Wong, T.-S.; Kang, S. H.; Tang, S. K.; Smythe, E. J.; Hatton, B. D.; Grinthal, A.; Aizenberg, J., Bioinspired self-repairing slippery surfaces with pressure-stable omniphobicity. *Nature* 2011, *477* (7365), 443-447.

27.   Barbieri, L.; Wagner, E.; Hoffmann, P., Water wetting transition parameters of perfluorinated substrates with periodically distributed flat-top microscale obstacles. *Langmuir* 2007, *23* (4) 1723-1734.

Abbreviations

AA	acrylic acid
AFM	atomic force microscope
APS	3-aminopropyltriethoxysilane
CLSM	confocal laser scanning microscopy
CVD	chemical vapor deposition
FIB	focued ion beam
µm	micrometer
nm	nanometer
PAA	poly(acrylic acid)
PAH	poly(allylamine hydrochloride)
par.	paragraph
PS	polystyrene
PTEF	polytetrafluoroethylene
PVP	polyvinylpyrrolidone
RMS	root mean square
rpm	round per minute
SEM	scanning electron microscopy
TEM	transmission electron microscopy
THF	tetrahydrofuran

Chapter 2: Transparent, thermally stable and mechanically robust superhydrophobic surfaces made from porous silica capsules

Xu Deng, Lena Mammen, Yanfei Zhao, Philipp Lellig, Klaus Müllen, Chen Li, Hans-Jürgen Butt, and Doris Vollmer*

Max Planck Institute for Polymer Research, Ackermannweg 10, D-55128, Mainz (Germany)

Superhydrophobic surfaces are advantageous for a cost-effective maintenance of a variety of surfaces.[1] The combination of micro and nano-sized roughness increases the contact angle of water such that water droplets cannot adhere but roll off.[2] Therefore, superhydrophobic coatings are self-cleaning and anticorrosive. Lately, many artificial surfaces have been investigated with regard to their wetting dynamics[3] as well as their chemical, mechanical,[4] and thermal stability.[5] If the superhydrophobic surface were even transparent, the range of possible applications could be expanded to glass-based substrates such as goggles or windshields[6] and, equally important, prevent an efficiency degradation of solar cells by pollution accumulation.[7] Clearly, the coatings must be easy to fabricate, mechanically resistant, and long-term stable. So far, none of the existing methods fulfilled all these requirements. Mechanical robustness is particularly critical because the dual scale roughness can easily be destroyed irreversibly[8] leading to a rapid decrease of the contact angle and an increase of contact angle hysteresis.

Herein, we use porous silica capsules as key components of lotus leaf-like super-hydrophobic surfaces. The latter are highly transparent as well as mechanically and thermally stable. When used as transparent coatings for organic solar cells they leave their performance unaffected.

Raspberry-like particles are promising constituents to prepare superhydrophobic surfaces.[9] D'Acunzi developed a procedure to grow silica particles on a polystyrene core, permitting to control both, the number and size of attached silica particles.[10] Micrometer sized polystyrene (PS) particles are synthesized by soap free emulsion polymerization and taken as core particles for the successive Stöber reaction. The number of silica particles attached to the polystyrene core can be tuned by the amount of acrylic acid added to the soap-free emulsion polymerization. The size of the silica particles can be controlled by the amount of tetraethoxysilane (TES) used in the Stöber reaction. Here, an amount of TES is taken to get about 50 nm sized silica particles and an acrylic acid concentration that the silica particles partially grow together during the Stöber-reaction, forming a three-dimensional porous shell (see Fig. 1b).
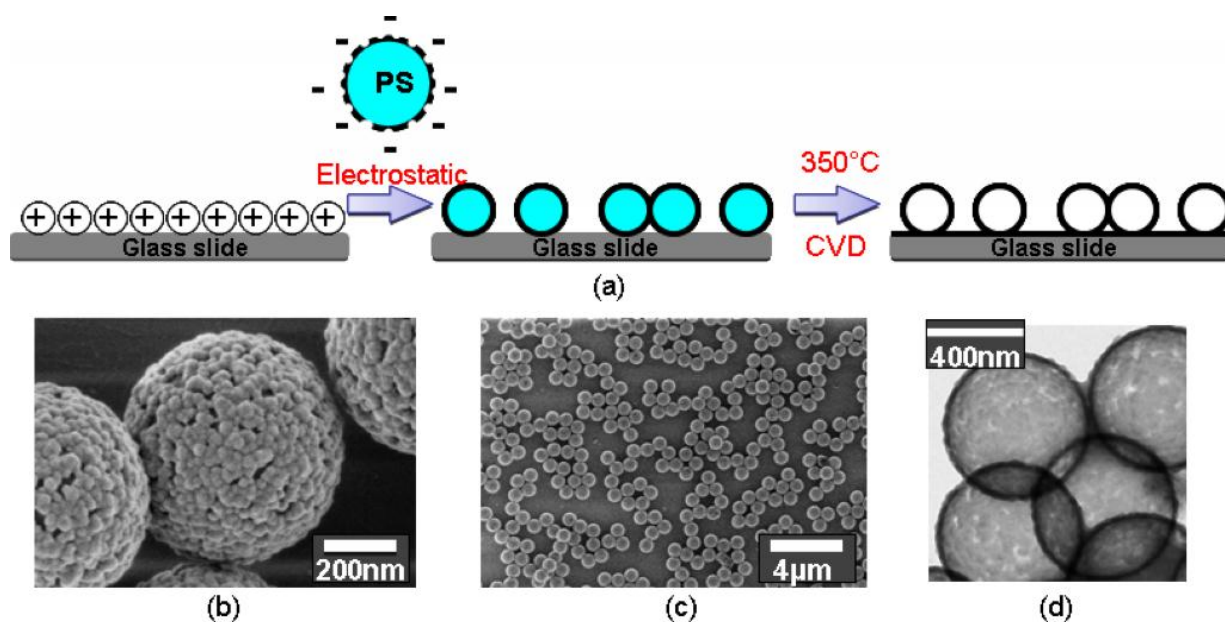
Figure 1. (a) Sketch of the procedure taken to prepare transparent superhydrophobic surfaces. (b) SEM micrographs of polystyrene particles coated with nanometer-sized silica spheres. (c) After dip coating the glass substrate is partially covered with raspberry-like particles. (d) TEM image taken after the PS core has been removed by calcination. Despite the high porosity (white patches) of the silica shell (dark rim) it remains intact.

To prepare superhydrophobic surfaces (Fig 1a), amine-terminated glass plates are treated with hydrochloric acid.[11] The positively charged plates are immersed in a dispersion of negatively-charged raspberry-like particles and electrostatic interactions are responsible for the adhesion of the particles at the surface. Excess particles are removed by rinsing the substrate with Milli-Q water, giving rise to a large scale homogeneous but locally irregular coating of the glass substrate with raspberry-like particles (Fig. 1c). To render the monolayer transparent, the PS cores are removed by thermal degradation (Fig. 1d).
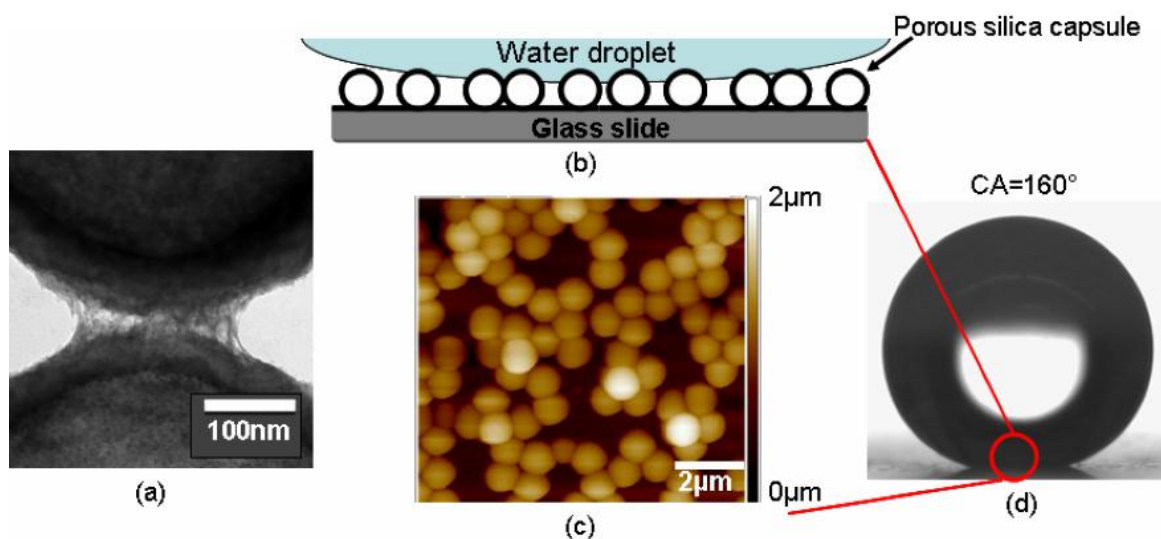
Figure 2. (a) High resolution TEM image of two neighboring silica capsules connected by a silica bridge that formed during chemical vapor deposition of tetraethoxysilane. (b) Sketch of the solid-liquid-air three phase contact line. The spheres picture the capsules. (c) AFM height image of a superhydrophobic surface. The flat glass substrate appears dark brown, the particles forming the first layer light brown and those forming a second layer as white. Scanning size: 10μm×10μm. (d) Photograph of a 3μl water droplet deposited on a superhydrophobic surface. The surface shows a static contact angle CA of 160° and a sliding angle of 5°.

So far this coating suffers from poor mechanical stability, because the particles are bound to each other and to the substrate only by van der Waals interactions. To improve the mechanical stability chemical vapor deposition (CVD) of tetraethoxysilane in the presence of ammonia is

performed. Similar to a Stöber reaction, silica is formed by hydrolysis and condensation of tetraethoxysilane catalysed by ammonia. Transmission electron microscopy (TEM) revealed that after CVD neighboring particles are chemically bound to each other and to the surface via silica bridges (Fig. 2 a). Atomic force microscopy (AFM) and scanning electron microscopy (SEM) imaging show that some particles are fixed to the first layer, giving rise to asperities with a height between 0.8 μm and 1.5 μm (Fig. 1c, 2c). This further increases microscale roughness. After hydrophobization of the surface by CVD of a semi-fluorosilane the surface exhibits remarkable superhydrophobicity with a static contact angle (CA) of 160° and a sliding angle for water droplets below 5° (Fig. 2d). One concludes from these findings that the water droplets are sitting on top of the microstructure with air pockets remaining between the silica capsules and water, i.e. the droplets are in the Cassie state (Fig. 2c).[12]

To demonstrate the extraordinary water repellency of the coating, tiny amounts of water (0.02 μl to 0.09 μl) are repeatedly added to a 4 μl large water drop deposited on a superhydrophobic surface. Merging of both drops reduces the overall surface energy.[13] The released energy is converted into kinetic energy, resulting in visible vibrations of the drop together with a detachment of the drop from the substrate (see supplemental video S1). The surface is not only water repellent but also self-cleaning as demonstrated by water drops falling from 6.5 cm height on a sand "polluted" superhydrophobic surface (supplemental video S2). The sand grains are partially flushed away and partially enwrapped into the water upon impacting the surface. After the drops rebounded and roll off the impacting area is clean.
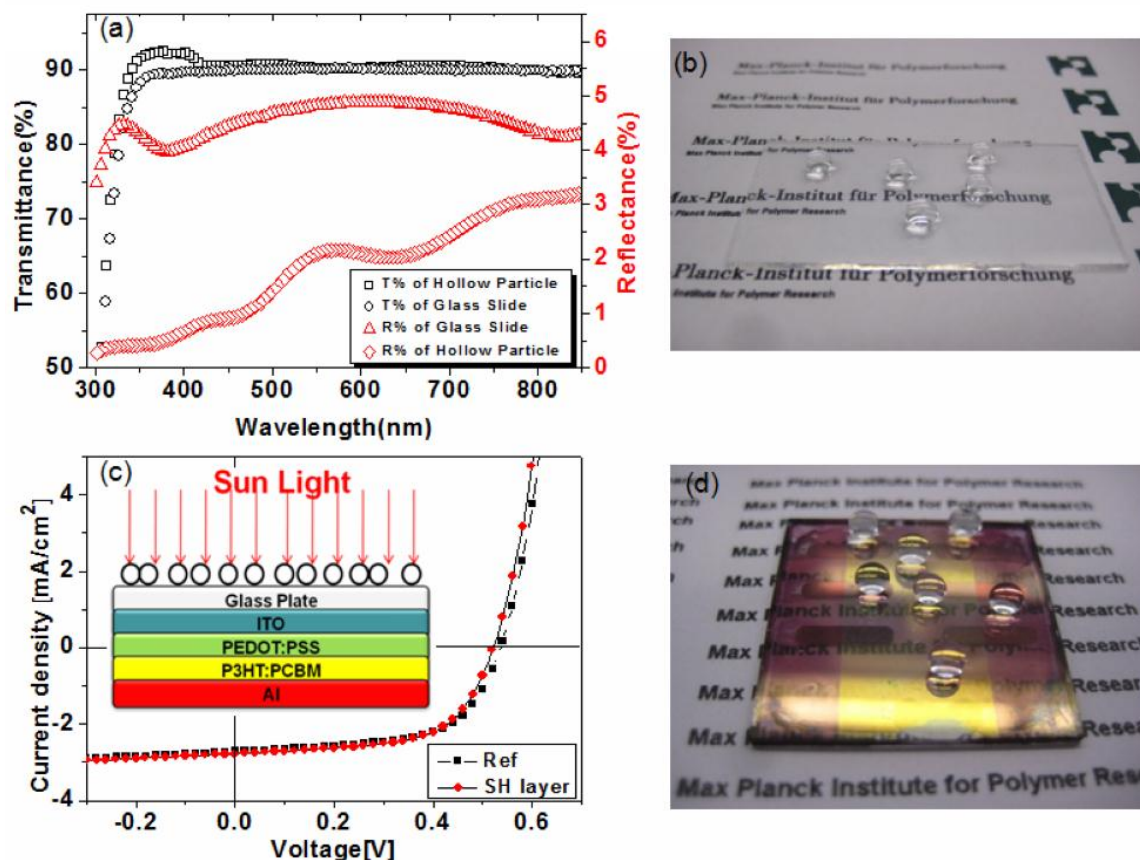
Figure 3. (a) Transmittance and reflectance spectra of a transparent superhydrophobic surface compared to a bare glass slide. The specular reflection was measured at an incidence angle of 15°. (b) Photograph of water droplets deposited on a superhydrophobic glass substrate. (c) Comparison of current-voltage curves of P3HT: PCBM organic solar cells prepared on a glass substrate coated with or without a monolayer of porous silica capsules. The inset shows a sketch of the organic solar cell. (d) Water droplets deposited on the solar cell. The efficiency measurements do not affect its superhydrophobicity.

Self-cleaning is desirable for many applications, including windows and solar cells. However, both applications need the coatings to be transparent. In general, transmittance decreases with increasing roughness, especially if the roughness exceeds the wavelength of light.[14] Although the porous silica capsules used herein are micrometer sized, the thickness of their porous shells is about 50 nm. Destructive interference between light reflected from the particle-substrate and the air-particle interfaces can give rise to low reflectivity, respectively to

41

high transmission.[15] Depending on the particle diameter, shell thickness, and refractive index, the transmittance of the coating can increase or decrease. According to the UV-Vis spectra, the transmittance of the superhydrophobic coating is enhanced in the short (330 nm to 410 nm) and essentially unchanged in the long-wavelength range as compared to bare glass slides (Fig. 3a, left axis). The increased transmittance is going in line with a strongly reduced reflectivity for short wavelengths. Remarkably enough, the whole spectrum shows a reduced reflectivity as compared to bare glass and is decreased in most of the visible range by more than a factor of two (Fig. 3a, right axis). The high transparency of the substrate is reflected in the good readability of the letters underneath and its superhydrophobicity is evidenced by the high contact and low sliding angle of water droplets carefully deposited (Fig. 3b).

The self-cleaning properties and good light transmission are beneficial for solar cell applications if the coating can be easily applied and does not affect the efficiency. To investigate this, organic solar cells are built on bare and superhydrophobic glass substrates (Inset of Fig. 3c).[16] The current-voltage curves are identical within experimental accuracy (Fig. 3c), i.e. the overall power conversion efficiency ($\eta\%$) of 3.9% is unaffected by the coating (details in Table S1). On the other hand, also the contact and sliding angle are not changed by the preparation of the solar cell (Fig. 3d). Both values are identical when measured before building the solar cell and after performing the efficiency test.

In many applications surfaces are exposed to heat,[17] i.e. the coating must keep its performance after heating. To determine the thermal resistance of the superhydrophobic surfaces, the samples are annealed at temperatures from 20°C to 400°C for 10 hours, respectively. The sliding and static contact angle remain constant for temperatures up to 350 °C (Fig. 4 c), documenting the excellent thermal stability of the hydrophobized silica shells.
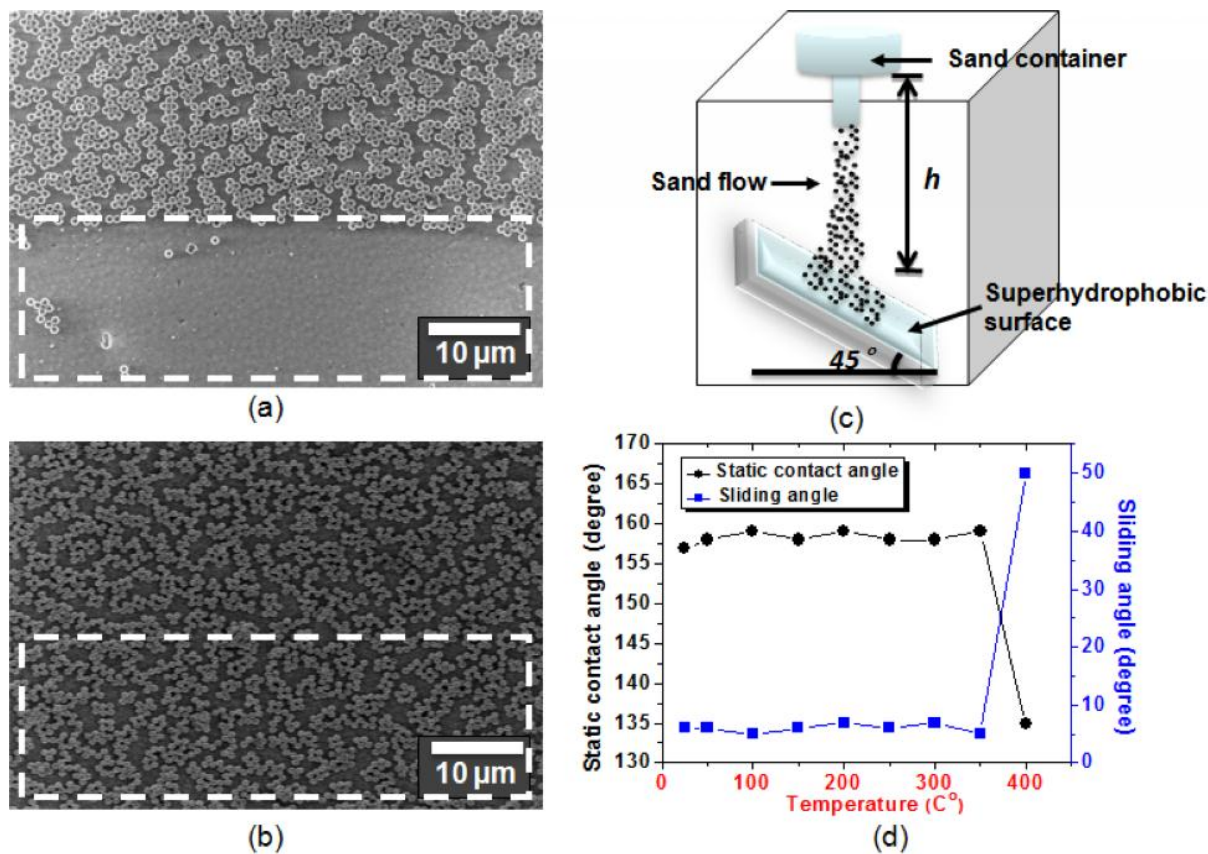
Figure 4. SEM images of superhydrophobic surfaces that were partially exposed to double sided tape (white boxes indicate the exposed areas). (a) If the particles stick to the surface by van der Waals interaction only, they can easily be removed. (b) Particles can't be removed by double sided tape after binding them chemically to the surface by silica bridges. (c) Sketch of the setup used to determine the stability of the surface against sand impact. (d) Static contact angle and sliding angle measured after annealing the samples for 10 hours at different temperatures. The surface remains superhydrophobic until annealing at 350°C.

To quantify the mechanical stability of the surface two complementary tests were performed. Firstly, double sided adhesive tape is pressed with approx 10 kPa to the surfaces, both, before and after performing CVD of TES. If the capsules are attached to the surface by van der Waals interactions only a sharp boundary is visible, separating areas that are and are not exposed to tape. After peeling the tape off, the area underneath it is almost particle free, substantiating the poor adhesion of the particles to the substrate (white box in Fig. 4a). Contrary,

if CVD of TES is performed beforehand peeling the tape off does not change the particle coverage (Fig. 4b).

In a second test, sand gains are impacted on a superhydrophobic surface and the minimal height is determined at which the porous silica particles burst. Bursting leads to an increase of the sliding angle and finally to a loss of superhydrophobicity. If 100 to 300 μm sized sand grains impact on a superhydrophobic surface the shells remain intact for impact heights, h, up to 30 cm. A sand abrasion test is shown in the supplemental video S3. After the sand abrasion the surface remained superhydrophobic, i.e. water droplets placed on the surface can bounce and slide off easily. For h significantly larger than 30 cm fractured shells are found (Fig. S3). The stability of our surfaces against bursting can be quantified, by calculating the impact energy of a sand grain: $W_s = m_s\, g\, h = 4/3\ \pi\ \rho\ R_s^3\, g\, h = 2.4\ 10^{-8}$ J. Here, ρ is the density of silica ($\rho \approx 2$ g/cm^3), g the acceleration of gravity, and R_s the radius of the sand grains ($R_s \approx 100$ μm). This energy is distributed amongst the particles underneath the impacting particle. To estimate the impacting area, it is assumed that the capsules break for deformation above $z = 25$ nm, supported by previous AFM experiments on similar sized silica capsules.[18] Thus, the impacting area, A_s, is $A_s = 2\ \pi\ R_s\ z = 15$ μm^2. The average coverage density of the superhydrophobic substrate with particles (see Fig. 3a, 3b) is $A_p = 0.9\ /\ \mu m^2$, i.e. the energy is distributed among N = 17 capsules ($N = A_s\ /\ A_p$). This implies that a porous capsule withstands an impact energy, W_p, of $W_p = W_s\ /\ N = 1.6\ 10^{-9}$ J. This is even a lower limit because we used the minimal radius R_s and assumed an equal distribution of the impact energy on all 17 capsules.

To quantify the stability of our surfaces towards an impact of aerosol particles we estimate the maximally allowed impact velocity, v_A. The latter depends on the radius R_A of aerosol particles, $W_s = 0.5\ m_A\ v_A^2$, were $m_A = 4/3\ \pi\ \rho\ R_A^3$ denotes the mass of aerosol particles. Considering that the radius of aerosol particles hardly exceed $R_A = 10 \mu m$[19] and assuming a density of $\rho = 2$ g/cm^3, our superhydrophobic surface stands impact velocities up to $v_A = [(2\ W_s)\ /\ (4/3\ \pi\ \rho\ R_A^3)]^{0.5} \approx 70$ km/h. In case of smaller sized particles the impact velocity may be even orders of magnitude higher, i.e. this coating may allow the step out from laboratory to outdoor applications.

In conclusion, a simple method to fabricate a superhydrophobic coating based on porous silica capsules is presented. The superhydrophobic coating shows a static contact angle of 160°

and sliding angle less than 5°. Moreover it is thermally stable up to 350°C. The superhydrophobic coating does not diminish the efficiency of organic solar cells, also due to its excellent transparency. On the other hand, it will prevent foiling which would decrease the efficiency of solar cells by more than 10% in course of time. Further, the coating retains it's superhydrophobicity under adhesion tape peeling and sand abrasion.

Experimental section:

Surface preparation: Polystyrene spheres were synthesized by soap-free emulsion polymerization. The PS particles (1.5 g, diameter = 800 nm) were dispersed in ethanol (80 ml). Ammonia (6.6 ml) and a mixture of TES and ethanol (2 ml TES in 18 ml ethanol) were added under stirring at 250 rpm at room temperature. After 1 day the composite particles were washed in ethanol and transferred to water. Positively charged glass slides were dipped in a suspension (5 g particles dispersed in 1 L water) for 30 minutes and then rinsed in water. The slides covered with particles were dried in air and annealed at 350°C for 2 hours to remove the polystyrene core. Thereafter, the silica capsules were placed in an exsiccator together with 2 vessels containing 1ml TES and 1ml ammonia, respectively. CVD of TES was performed for 24 hours. Finally, the coatings are hydrophobized by placing 1 ml of a semi-fluorosilane in an exsiccator for 3 hours along with the sample. Further details can be found in the supporting information.

1.   Shibuichi, S.; Yamamoto, T.; Onda, T.; Tsujii, K., Super Water- and Oil-Repellent Surfaces Resulting from Fractal Structure. *Journal of Colloid and Interface Science* **1998,** *208* (1), 287-294.

2.   Butt, H.-J.; Graf, K.; Kappl, M., Contact Angle Phenomena and Wetting. In *Physics and Chemistry of Interfaces*, Wiley-VCH Verlag GmbH & Co. KGaA: 2004; pp 118-144.

3.   Wenzel, R. N., RESISTANCE OF SOLID SURFACES TO WETTING BY WATER. *Industrial & Engineering Chemistry* **1936,** *28* (8), 988-994.

4.   Cassie, A. B. D.; Baxter, S., Wettability of porous surfaces. *Transactions of the Faraday Society* **1944,** *40* (0), 546-551.

5.   Callies, M.; Quere, D., On water repellency. *Soft Matter* **2005,** *1* (1), 55-61.

6.   de Gennes, P. G.; Brochard-Wyard, F.; Quéré, D.; Reisinger, A., *Capillarity and wetting phenomena : drops, bubbles, pearls, waves*. Springer: New York [etc.], 2004.

7.   Furmidge, C. G. L., Studies at phase interfaces. I. The sliding of liquid drops on solid surfaces and a theory for spray retention. *Journal of Colloid Science* **1962,** *17* (4), 309-324.

8.   Barthlott, W.; Neinhuis, C., Purity of the sacred lotus, or escape from contamination in biological surfaces. *Planta* **1997,** *202* (1), 1-8.

9.   D'Acunzi, M., *Core-shell Particles and Their Application for Superhydrophobic Surfaces*. 2010.

10.   Bico, J.; Marzolin, C.; Quere, D., Pearl drops. *Europhysics Letters* **1999,** *47* (2), 220-226.

11.   Sun, M.; Luo, C.; Xu, L.; Ji, H.; Ouyang, Q.; Yu, D.; Chen, Y., Artificial Lotus Leaf by Nanocasting. *Langmuir* **2005,** *21* (19), 8978-8981.

12.   Ming, W.; Wu, D.; van Benthem, R.; With, G. d., Superhydrophobic films from raspberry-like particles. *Nano letters* **2005,** *5* (11), 2298-2301.

13.   Fernández-Blázquez, J. P.; Fell, D.; Bonaccurso, E.; Campo, A. d., Superhydrophilic and superhydrophobic nanostructured surfaces via plasma treatment. *Journal of Colloid and Interface Science* **2011,** *357* (1), 234-238.

14.   Ma, M.; Gupta, M.; Li, Z.; Zhai, L.; Gleason, K. K.; Cohen, R. E.; Rubner, M. F.; Rutledge, G. C., Decorated electrospun fibers exhibiting superhydrophobicity. *Advanced Materials* **2007,** *19* (2), 255-259.

15.   Shirtcliffe, N. J.; Aqil, S.; Evans, C.; McHale, G.; Newton, M. I.; Perry, C. C.; Roach, P., The use of high aspect ratio photoresist (SU-8) for super-hydrophobic pattern prototyping. *Journal of Micromechanics and Microengineering* **2004,** *14* (10), 1384.

16.   Erbil, H. Y.; Demirel, A. L.; Avcı, Y.; Mert, O., Transformation of a Simple Plastic into a Superhydrophobic Surface. *Science* **2003,** *299* (5611), 1377-1380.

17.   (a) Lafuma, A.; Quere, D., Superhydrophobic states. *Nat Mater* **2003,** *2* (7), 457-460; (b) Liu, G.; Craig, V. S. J., Macroscopically flat and smooth superhydrophobic surfaces: Heating induced wetting transitions up to the Leidenfrost temperature. *Faraday Discussions* **2010,** *146*, 141-151; (c) Feng, X. J.; Jiang, L., Design and creation of superwetting/antiwetting surfaces. *Advanced Materials* **2006,** *18*, 3063-3078; (d) Kim, S. H.; Lee, S. Y.; Yang, S. M., Janus Microspheres for a Highly Flexible and Impregnable Water-Repelling Interface. *Angew. Chem. Int. Ed.* **2010,** *49* (14), 2535-2538.

18.   (a) Barthlott, W.; Schimmel, T.; Wiersch, S.; Koch, K.; Brede, M.; Barczewski, M.; Walheim, S.; Weis, A.; Kaltenmaier, A.; Leder, A.; Bohn, H. F., The Salvinia Paradox: Superhydrophobic Surfaces with Hydrophilic Pins for Air Retention Under Water. *Advanced Materials* **2010,** *22* (21), 2325-2328; (b) Gao, L. C.; McCarthy, T. J., The "lotus effect" explained: Two reasons why two length scales of topography are important. *Langmuir* **2006,** *22* (7), 2966-2967.

19.   (a) Gao, Y.; Cheng, M.; Wang, B.; Feng, Z.; Shi, F., Diving–Surfacing Cycle Within a Stimulus-responsive Smart Device Towards Developing Functionally Cooperating Systems. *Advanced Materials* **2010,** *22* (45), 5125-5128; (b) Manukyan, G.; Oh, J. M.; van den Ende, D.; Lammertink, R. G. H.; Mugele, F., Electrical Switching of Wetting States on Superhydrophobic Surfaces: A Route Towards Reversible Cassie-to-Wenzel Transitions. *Physical Review Letters* **2011,** *106* (1), 014501; (c) Li, C.; Guo, R. W.; Jiang, X.; Hu, S. X.; Li, L.; Cao, X. Y.; Yang, H.; Song, Y. L.; Ma, Y. M.; Jiang, L., Reversible Switching of Water-Droplet Mobility on a Superhydrophobic Surface Based on a Phase Transition of a Side-Chain Liquid-Crystal Polymer. *Advanced Materials* **2009,** *21* (42), 4254-+; (d) Zhao, N.; Xie, Q. D.; Kuang, X.; Wang, S. Q.; Li, Y. F.; Lu, X. Y.; Tan, S. X.; Shen, J.; Zhang, X. L.; Zhang, Y.; Xu, J.; Han, C. C., A novel ultra-hydrophobic surface: Statically non-wetting but dynamically non-sliding. *Advanced Functional Materials* **2007,** *17*, 2739-2745.

20.   (a) Xiu, Y. H.; Liu, Y.; Hess, D. W.; Wong, C. P., Mechanically robust superhydrophobicity on hierarchically structured Si surfaces. *Nanotechnology* **2010,** *21* (15); (b) Ling, X. Y.; Phang, I. Y.; Vancso, G. J.; Huskens, J.; Reinhoudt, D. N., Stable and Transparent Superhydrophobic Nanoparticle Films. *Langmuir* **2009,** *25* (5), 3260-3263; (c) Zhang, X.; Shi, F.; Niu, J.; Jiang, Y. G.; Wang, Z. Q., Superhydrophobic surfaces: from structural control to functional application. *Journal of Materials Chemistry* **2008,** *18* (6), 621-633.

21.   Sarkar, S.; Chunder, A.; Fei, W. F.; An, L. N.; Zhai, L., Superhydrophobic mats of polymer-derived ceramic fibers. *Journal of the American Ceramic Society* **2008,** *91* (8), 2751-2755.

22.   (a) Nakajima, A.; Fujishima, A.; Hashimoto, K.; Watanabe, T., Preparation of transparent superhydrophobic boehmite and silica films by sublimation of aluminum acetylacetonate. *Advanced Materials* **1999,** *11* (16), 1365-1368; (b) Tadanaga, K.; Katata, N.; Minami, T., Super-water-repellent Al2O3 coating films with high transparency. *Journal of the American Ceramic Society* **1997,** *80* (4), 1040-1042; (c) Li, Y.; Liu, F.; Sun, J. Q., A facile layer-by-layer deposition process for the fabrication of highly transparent superhydrophobic coatings. *Chemical Communications* **2009,** (19), 2730-2732; (d) Lee, S. G.; Lee, D. Y.; Lim, H. S.; Lee, D. H.; Lee, S.; Cho, K., Switchable Transparency and Wetting of Elastomeric Smart Windows. *Advanced Materials* **2010,** *22* (44), 5013-5017.

23.   (a) Park, Y.-B.; Im, H.; Im, M.; Choi, Y.-K., Self-cleaning effect of highly water-repellent microshell structures for solar cell applications. *Journal of Materials Chemistry* **2011**; (b) Choi, S. J.; Huh, S. Y., Direct Structuring of a Biomimetic Anti-Reflective, Self-Cleaning Surface for Light Harvesting in Organic Solar Cells. *Macromolecular Rapid Communications* **2010,** *31* (6), 539-544; (c) Zhu, J.; Hsu, C. M.; Yu, Z. F.; Fan, S. H.; Cui, Y., Nanodome Solar Cells with Efficient Light Management and Self-Cleaning. *Nano Letters* **2010,** *10* (6), 1979-1984.

24.   Verho, T.; Bower, C.; Andrew, P.; Franssila, S.; Ikkala, O.; Ras, R. H. A., Mechanically Durable Superhydrophobic Surfaces. *Advanced Materials* **2010**, n/a-n/a.

25.   Ming, W.; Wu, D.; van Benthem, R.; de With, G., Superhydrophobic films from raspberry-like particles. *Nano Letters* **2005,** *5* (11), 2298-2301.

26.   D'Acunzi, M.; Mammen, L.; Singh, M.; Deng, X.; Roth, M.; Auernhammer, G. K.; Butt, H. J.; Vollmer, D., Superhydrophobic surfaces by hybrid raspberry-like particles. *Faraday Discussions* **2010,** *146*, 35-48.

27.   Tsai, H. J.; Lee, Y. L., Facile method to fabricate raspberry-like particulate films for superhydrophobic surfaces. *Langmuir* **2007,** *23*, 12687-12692.

28.   (a) Callies, M.; Quere, D., On water repellency. *Soft Matter* **2005,** *1*, 55-61; (b) Cassie, A. B. D., Contact angles. *Discussions of the Faraday Society* **1948,** *3*, 11-16.

29.   Boreyko, J. B.; Chen, C. H., Self-Propelled Dropwise Condensate on Superhydrophobic Surfaces. *Physical Review Letters* **2009,** *103* (18).

30.   Li, Y. F.; Zhang, J. H.; Zhu, S. J.; Dong, H. P.; Jia, F.; Wang, Z. H.; Sun, Z. Q.; Zhang, L.; Li, Y.; Li, H. B.; Xu, W. Q.; Yang, B., Biomimetic Surfaces for High-Performance Optics. *Advanced Materials* **2009,** *21* (46), 4731-+.

31.   Bravo, J.; Zhai, L.; Wu, Z. Z.; Cohen, R. E.; Rubner, M. F., Transparent superhydrophobic films based on silica nanoparticles. *Langmuir* **2007,** *23* (13), 7293-7298.

32.   Ma, W.; Yang, C.; Gong, X.; Lee, K.; Heeger, A. J., Thermally Stable, Efficient Polymer Solar Cells with Nanoscale Control of the Interpenetrating Network Morphology. *Advanced Functional Materials* **2005,** *15* (10), 1617-1622.

33.   Janssen, R. A. J.; Hummelen, J. C.; Saricifti, N. S., Polymer-fullerene bulk heterojunction solar cells. *Mrs Bulletin* **2005,** *30* (1), 33-36.

34.   Zhang, L.; D'Acunzi, M.; Kappl, M.; Auernhammer, G. K.; Vollmer, D.; van Kats, C. M.; van Blaaderen, A., Hollow Silica Spheres: Synthesis and Mechanical Properties. *Langmuir* **2009,** *25* (5), 2711-2717.

35.   Ahmed, A. S.; Ali, A. A.; Alhaider, M. A., MEASUREMENT OF ATMOSPHERIC PARTICLE-SIZE DISTRIBUTION DURING SAND DUSTSTORM IN RIYADH, SAUDI-ARABIA. *Atmospheric Environment* **1987,** *21* (12), 2723-2725.

Supporting Information

1. **Experimental method**

1.1 *Materials*

The chemicals were ordered from the following sources: tetraethoxysilane (TES) (Acros Organics, 98%), ammonia (VWR, 28%), (tridecafluoro-1,1,2,2-tetrahydrooctyl)-1-trichlorosilane

(Sigma Aldrich, 97%) and (3-aminopropyl) trimethoxysilane, 3-AMDS(Fluka, Germany). All chemicals and solvents were used without further purification. Adhesive tape (3M) was obtained from a commercial source.

1.2 *Silanization*

Silanization was performed at room temperature by placing the particle-coated substrate and a small glass vessel containing 1 ml of (tridecafluoro-1,1,2,2-tetrahydrooctyl)-1-trichlorosilane in a closed desiccator for 3 h. To increase the vapour pressure of silane the desiccator was evacuated for a few minutes every half an hour. Afterwards the vessel containing the silane was removed from the desiccator and a vacuum was applied for one hour in order to remove unreacted silane residues.

1.3 Solar cell fabrication

The organic solar cells were built on a cleaned glass substrate. On one side indium tin oxide (ITO) was deposited and the other side was coated with porous hollow particles (according to 1.4). Then the active layers were carefully fabricated on the ITO coated side following well-known procedures.[29]

1.4 Characterization

The morphology of the particles and the monolayer were characterized by Scanning Electron Microscopy (LEO 1530 Gemini, Germany) and Atomic Force Spectroscopy (Veeco Metrology Group, NY). Particles and silica bridges were imaged by Transmission Electron Microscopy (FEI; 200 kV). Static contact angle and sliding angle were measured with a contact angle meter, Dataphysics OCA35 (Data Physics Instruments GmbH, Germany). Reflectivity and transmission were measured using an ultraviolet-visible spectrometer (Lambda 900, Perkin Elmer) in double-beam mode, using an uncovered glass slide as a reference. The solar cells were tested in an ambient atmosphere of nitrogen. Solar light was simulated using a 575 W metal halide lamp (Lichttechnik, Germany), in combination with an ODF filter, to produce a spectral distribution close to global radiation AM 1.5 G. The light intensity of the simulated solar light was set to 200 W/m^2. Incident light was focused on an effective area. Current-voltage (I-V) curves were recorded with a Keithley 236 Source-Measure Unit (Keithley Instruments Inc.,USA). A standard

silicon diode was used to calibrate the incident light intensity for the calibration of the simulated solar light with measuring range of 200 W/m^2.

For the sand abrasion test 30 g of commercial sand (diameter: 100 µm to 300 µm) impacted the surface from a height of 30 cm, while the substrate was held at 45° to the horizontal surface. A predictive description of particle breakage is not yet available because breakage is history dependent.[1] For example, the number of micro-cracks and dislocations increase due to previous stressing events. Therefore, it is more common to study breakage probabilities which depend on the loading rate and the properties of the primary particles such as particle size. For solid particles the breakage probability is given by the product of the initial particle size, the number of impacts, the total mass specific net impact energy and a parameter characterizing the strength of a material.[2]

[1] S. Aman, J. Tomas, H. Kalman, Chem. Eng. Sci. **2010**, *65*, 1503.
[2] L. Vogel, W. Peukert, Chem. Eng. Sci. **2005**, *60*, 5164.
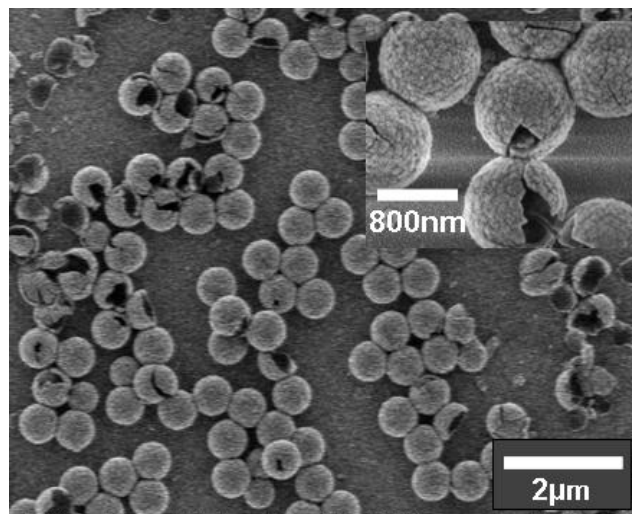
Fig.S2

Fig.S1 SEM image of superhydrophobic surface after sand falling from 40 cm height; Inset: high magnification of the surface after sand abrasion. Below 30 cm no broken particles were found.
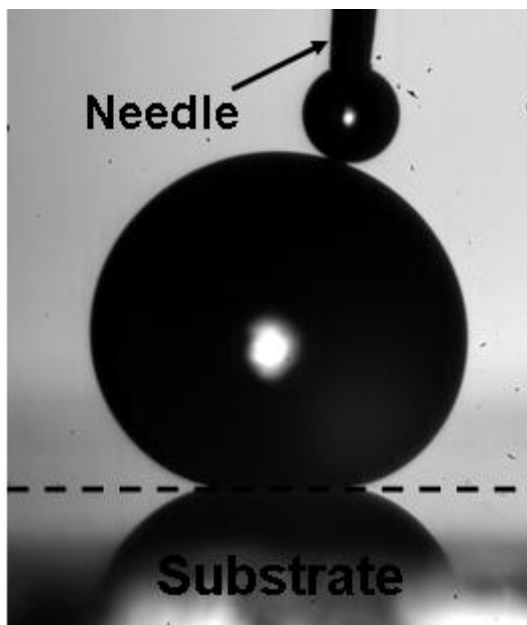
Fig.S2 Image of two water drops just before coalescence. The large droplet (4 μl) is resting on a superhydrophobic substrate and the smaller one is attached to a needle. See videoS1 for the full coalescence kinetics.

Table 1(a, b). The sun light conversion performance of organic solar cells with and without superhydrophobic coating.

Solar Cell (0.2 sun)	Isc (mA/cm^2)	Voc (V)	FF	η(%)
Ref (Without coating)	2.71	0.54	0.61	3.93%
SH layer (Coated with porous silica capsules)	2.77	0.52	0.61	3.91%

(a)

Solar Cell (1 sun)	Isc (mA/cm^2)	Voc (V)	FF	η(%)
Ref (Without coating)	8.83	0.59	0.62	3.68%

SH layer (Coated with porous silica capsules)	9.34	0.57	0.60	3.64%

(b)

To measurements of the performance of the solar cells were done for 0.2 sun and 1 sun respectively. The short-circuit current, I_{SC}, and the open-circuit voltage, V_{OC}, are the maximum current and voltage respectively. The fill factor, FF, is the ratio of the maximum power to the product of V_{oc} and I_{sc}.

Chapter 3: Transformation of black candle soot into a transparent robust superamphiphobic coating

Xu Deng,[1,2] Lena Mammen,[1] Hans-Jürgen Butt,[1] Doris Vollmer[1]*

[1]Max Planck Institute for Polymer Research, Ackermannweg 10, D-55128, Mainz

[2]Center of Smart Interfaces, Technical University Darmstadt, 64287 Darmstadt (Germany)

Coating is an essential step in adjusting the surface properties of materials. Superhydrophobic coatings with contact angles greater than 150° and roll off angles below 10° for water have been developed, based on low energy surfaces and roughness on the nano- and micrometer scales. However, these surfaces are still wetted by organic liquids such as surfactant-based solutions, alcohols, or alkanes. Coatings that are simultaneously superhydrophobic and superoleophobic are rare. We designed an easily fabricated, transparent, and oil-rebounding superamphiphobic coating. A porous deposit of candle soot was coated with a 25 nm thick silica shell. The black coating became transparent after calcination at 600°C. After silanization the coating is superamphiphobic and remained so even after its top layer was damaged by sand impingement.

A major goal in coating research is to design self-cleaning surfaces (*1-4*). Many surfaces in nature are superhydrophobic – for example lotus leaves (*5*). Mimicking their surface morphology led to the development of a number of artificial superhydrophobic surfaces (*6-7*), opening many applications in industrial and biological processes (*8-13*). Microscopic pockets of air are trapped beneath the water drops (*14-17*). This composite interface leads to an increase in the macroscopic contact angle and a reduced contact angle hysteresis, enabling water drops to roll

off easily, taking dirt with them. However, the addition of an organic liquid such as alcohol or oil, decreases the interfacial tension sufficiently to induce homogeneous wetting of the surface. Drops, initially resting on air pockets (Cassie state), pass the transition to complete wetting (Wenzel state) (*14*). No naturally occurring surface is known to show a contact angle θ of greater than 150° and roll off angles below 10° for water and organic liquids. These superhydrophobic and superoleophobic surfaces are called superamphiphobic (*18*).

In contrast to superhydrophobicity, the term "superamphiphobicity" is not uniquely defined in particular with respect to the liquid used (*19-22*). According to Young's equation, $\cos\Theta = (\gamma_{SV}-\gamma_{SL})/\gamma_{LV}$, the lower the surface tension the higher the tendency of a liquid to spread on a solid surface (*22-23*). Here, Θ is the macroscopic contact angle, γ_{SV} is the surface tension of the solid and γ_{SL} is the interfacial tension of the solid liquid interface. For organic liquids ($30 \leq \gamma_{LV} \leq 18$ mN/m) mainly van der Waals interaction act between the molecules. Therefore, $\gamma_{SV}-\gamma_{SL}$ is positive and on planar surfaces $\Theta < 90°$. Similarly, the contact angle on rough surfaces depends on the surface tensions, because roughness amplifies the wetting properties.

The key factors for superamphiphobicity are not clear yet. For water repellency, surface roughness and low surface energy are essential (*14*). To fabricate superamphiphobic surfaces overhangs, re-entrant geometry, or convex curvature is also important (*19-25*). The complex interplay between surface roughness, low surface energy and topography has made it difficult and expensive to fabricate superamphiphobic surfaces. Tuteja *et al.* showed that careful design of the topography of a surface allows to construct surfaces with a contact angle for hexadecane close to 160°, although the flat surface was oleophilic (*19, 23*). They explained their exceptional oil-repellency by overhang structures and re-entrant geometry.

Here we demonstrate a simple way to make robust, transparent, superamphiphobic coatings. The surface to be coated, in our case a glass slide, is held above a flame of a paraffin candle (Fig. 1A). Deposition of a soot layer turns the glass black. Scanning electron microscopy reveals that the soot consists of carbon particles with a typical diameter of 30 - 40 nm, forming a loose, fractal-like network (Fig. 1B,C) (*26*). A water drop gently deposited on the surface shows a contact angle above 160° and rolls off easily, demonstrating the surface's superhydrophobicity (*27*). However, the structure is fragile as the particle-particle interactions are only physical and weak. When water rolls off the surface, the drop carries soot particles with it until almost all of the soot deposit is removed and the drop undergoes a wetting transition (Movie. S1).
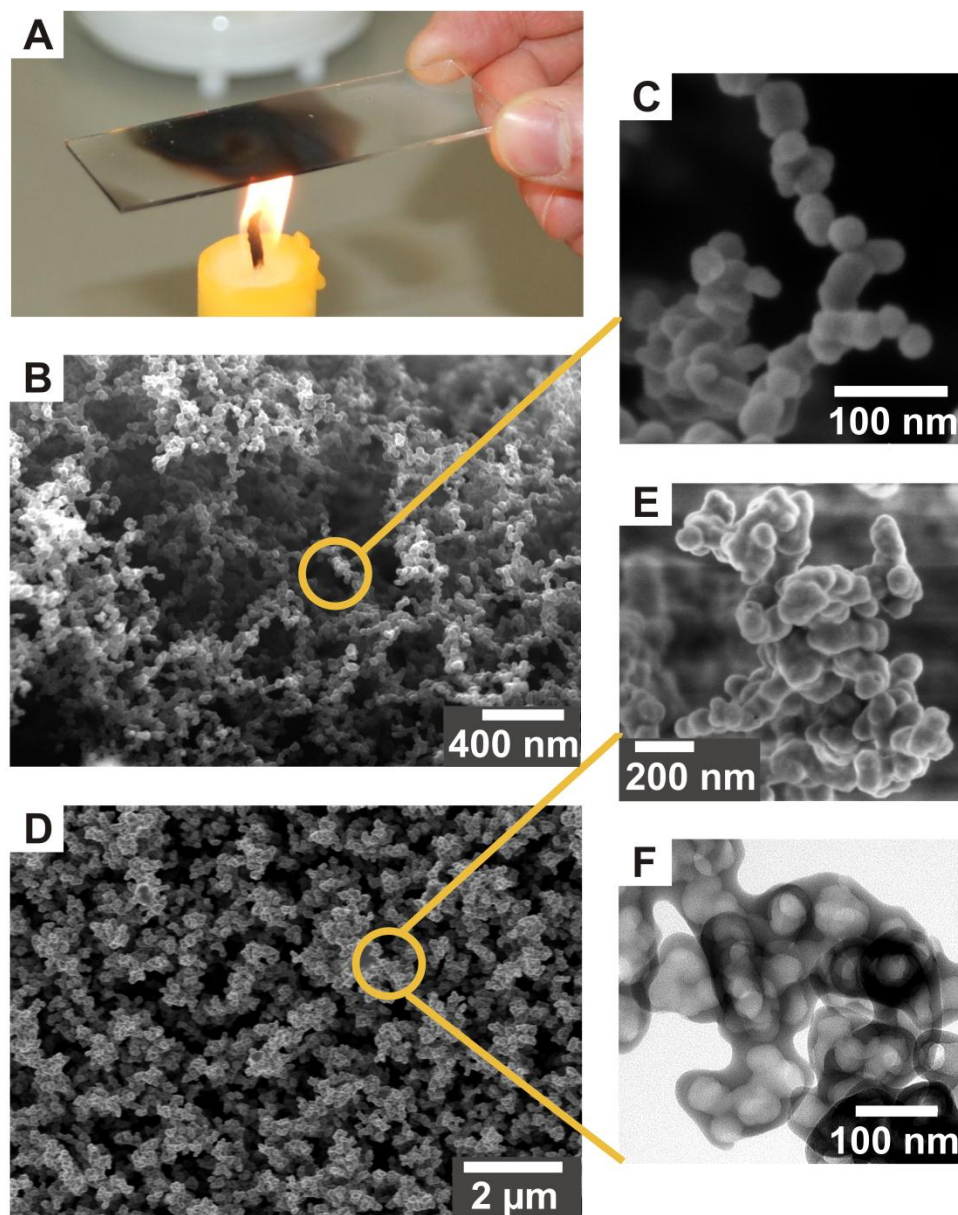
Fig. 1. Morphology of porous structure. (**A**) Photograph depicting sample preparation. A glass slide is held in the flame of a candle until a few μm thick soot layer is deposited. (**B**) Scanning electron microscope (SEM) image of the soot deposit. **C,** High resolution SEM image showing a single particle chain made up of almost spherical carbon beads of 40±10 nm diameter. (**D**) SEM image of the deposit after coating with a silica shell (see Fig. S2 for a cross section of the deposit). (**E**) High resolution SEM image of a cluster after removing the carbon core by heating for 2 h at 600 °C. (**F**) High resolution transmission electron microscopy image of a cluster after

calcination, revealing the silica coating with holes that were previously filled with carbon particles. The silica shell is 20 ± 5 nm thick.

Inspired by the promising morphology of soot, we developed a technique to coat the soot layer with a silica shell making use of chemical vapor deposition (CVD) of tetraethoxysilane (TES) catalyzed by ammonia. The soot-coated substrates are placed in a desiccator together with two open glass vessels containing tetraethoxysilane (TES) and ammonia, respectively (Fig. S1). Similar to a Stöber reaction, silica is formed by hydrolysis and condensation of TES. The shell thickness can be tuned by the duration of CVD. After 24 h the particles are coated by a 20 ± 5 nm thick silica shell (Fig. 1D,E). Calcinating the hybrid carbon/silica network at 600°C for 2 h in air causes combustion of the carbon core (Fig. 1F) and a decrease in the shell thickness, while the layer keeps its roughness and network texture. Only isolated chains of particles, which are not linked in the network, broke during calcination (Fig. 1B). To reduce the surface energy, the hydrophilic silica shells were coated with a semi-fluorinated silane by CVD. Therefore, the substrates and an open beaker with the volatile silane were put in a desiccator for 3 h. After CVD a water drop placed on top of the coating formed a static contact angle of $165° \pm 1°$ (Fig. 2A), with a roll-off angle lower than 1°. Owing to the extremely low adhesion of the coating to water, it was difficult to deposit water drops, because they immediately rolled off (Movie. S2). When drops of organic liquid were deposited, the static contact angles ranged from 154° for tetradecane up to 162° for diiodomethane, (Fig. 2B, Table 1, and Fig. S3). The maximal roll-off angle was 5°, even for tetradecane with a surface tension of 26 mN/m.

Liquid	Surface tension [mN/m]	flat surface SCA°	superamphiphobic surface	
			SCA°	Roll off angle°
water	72.1	108 ± 1	165 ± 1	1 ± 1
diiodomethane	50.9	91 ± 1	161 ± 1	2 ± 1
ethylene glycol	47.3	89 ± 1	160 ± 1	2 ± 1
peanut oil	34.5	70 ± 1	158 ± 1	4 ± 1
olive oil	32.0	69 ± 1	157 ± 1	4 ± 1
hexadecane	27.5	64 ± 1	156 ± 1	5 ± 1
tetradecane	26.5	54 ± 1	154 ± 1	5 ± 1

Table 1. Comparison of the static contact angle (SCA) and roll-off angle of drops with different surface tension, deposited on a flat fluorinated glass substrate and on a superamphiphobic coating.
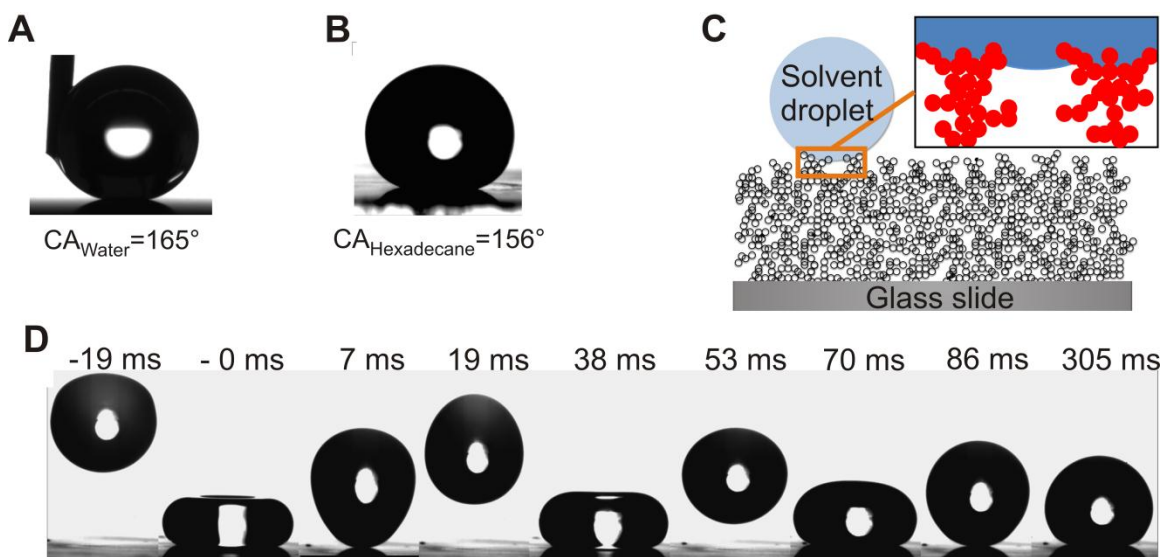

Fig. 2. Superamphiphobicity of the surface. A 2 µl water drop (A) and 5 µl hexadecane drop (B) deposited on the surface possess a static contact angle of 165°±1° and 156° ± 1°, respectively. (**C**) Cartoon of a liquid drop deposited on the fractal-like composite interface. (**D**) Time resolved bouncing of a 5 µl hexadecane drop on a super-amphiphobic surface. Just before impinging the drop's kinetic energy exceeds its interfacial energy by 2.4, i.e. the Weber number is 2.4 (*28*).

Hexadecane drops, radius of 1 mm, impinging with a velocity up to $v = 1$ m/s did not penetrate into the layer. The drop's kinetic energy was transformed into vibrational energy allowing the drop to rebound twice, before it underwent damped oscillations and finally rested on the surface in the Cassie state (Fig. 2D, S4, S5, Table S1) (*28-30*). The coating retained its superamphiphobicity even after impinging of at least thousands of water drops of a radius of 1.3 mm with a velocity of 1.4 m/s (Fig. S6), or flushing the coating with water for several hours.

At velocities between 1 - 1.5 m/s the drop started to penetrate into the coating. As a result a satellite drop was left on the surface after rebound. Typically at the second impact the satellite drop merged with the primary drop and rolled off, Fig. S5.

Self-cleaning properties for water and alkane were verified by depositing drops of either liquid on a superamphiphobic layer and monitoring the taking up of contaminants (Fig. S7).
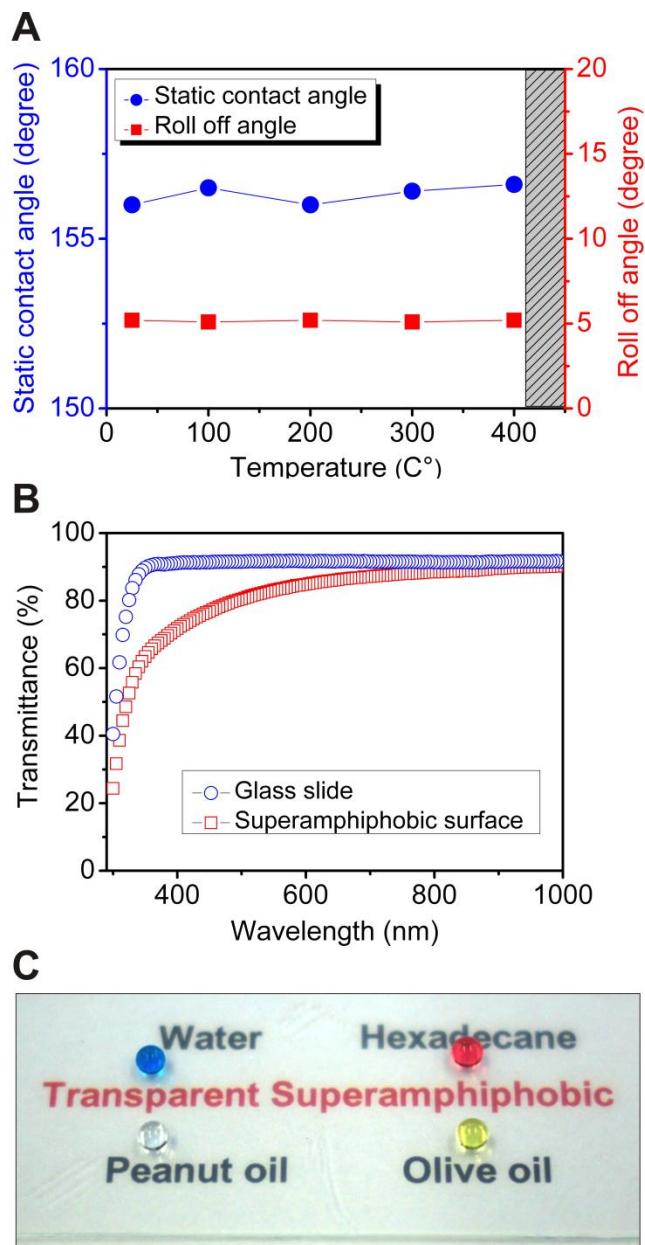

Fig. 3. Thermal stability and light transmittance of a superamphiphobic surface. (A) Static contact and roll-off angle of hexadecane measured after annealing the samples for 1 h at various temperatures. The surface loses its super-amphiphobicity after annealing at temperatures above

400 °C due to thermal degradation of the fluorosilane (shadow area). (**B**) UV-Vis transmittance spectra of a 3 μm thick superamphiphobic surface compared to pristine glass. (**C**) Photograph of dyed water (γ_{lv} = 72.1 mN/m; blue), peanut oil (γ_{lv} = 34.5 mN/m; white), olive oil (γ_{lv} = 32.0 mN/m; yellow), and dyed hexadecane drop (γ_{lv} = 27.5 mN/m; red) deposited on a superamphiphobic glass slide. The coated slide was placed on labeled paper.

For applications on glass surfaces such as goggles, touch screens, or difficult-to-access windows, the superamphiphobic coating needs to be thermally stable, transparent, and mechanically robust. To quantify the thermal stability, the coatings were annealed at temperatures up to 450°C for 1 h. The static contact and roll-off angle remained constant up to 400°C (Fig. 3A). Annealing at even higher temperatures decomposed the fluorosilane. The silica network remained almost unaltered until annealing up to 1000°C (Fig. S8). Annealed coatings can recover their superamphiphobicity after repeating CVD of a fluorosilane. After calcination of the black carbon template, the silica network has a shell thickness well below the wavelength of light. Such thin shells are highly transparent, as verified by UV-VIS (Fig. 3B). The transmittance of a 3 μm thick coating is reduced by less than 10 % compared to pristine glass for a wavelength above 500 nm. This transparency is reflected in the easy readability of the letters underneath the coated glass plate and its superamphiphobicity is depicted in the high contact angle for a wide variety of liquid drops (Fig. 3C).
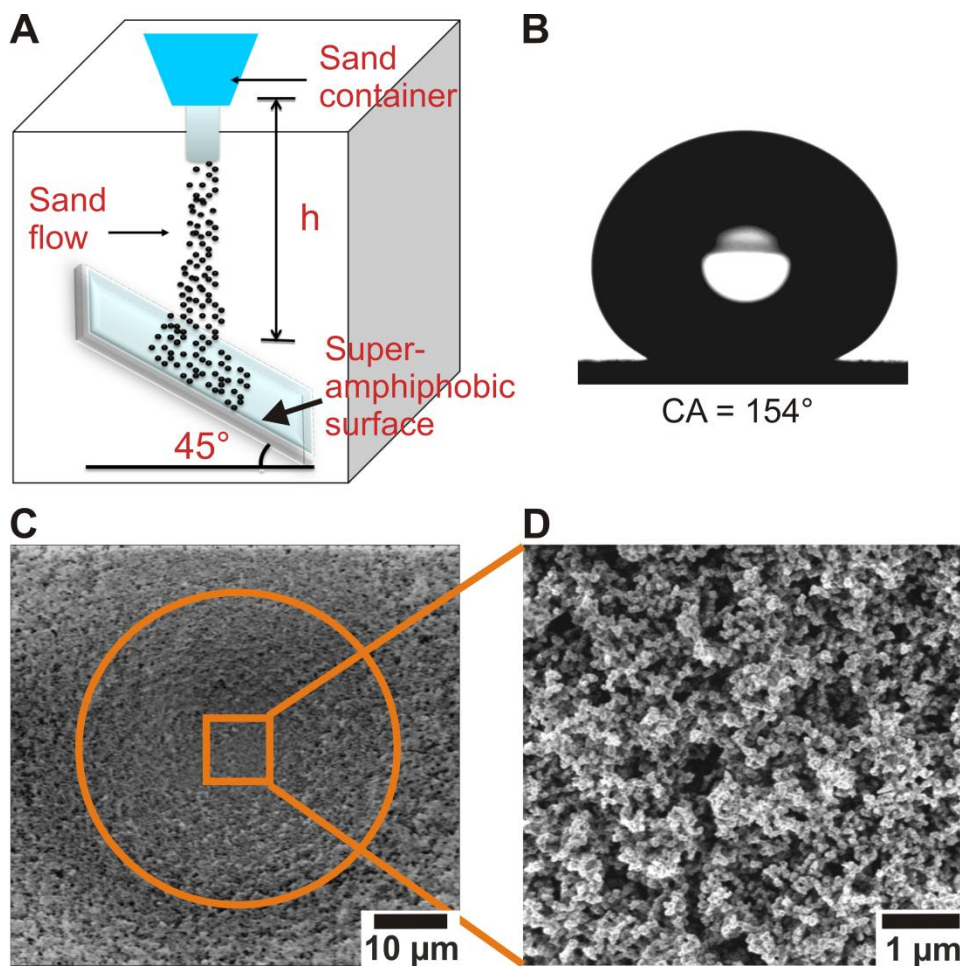
Fig. 4. Mechanical resistant quantified by sand abrasion. (**A**) Schematic drawing of a sand abrasion experiments. (**B**) Hexadecane drop deposited on the coating after 20 g sand abrasion from 40 cm height. The 100 to 300 μm sized grains have a velocity of 11 km/h just before impingement. After impingement drops rolls off after tilting the substrate by 5°. (**C**) SEM image of a spherical crater (orange circle) after sand abrasion. (**D**) SEM image of the surface topography inside the cavity.

In outdoor applications superamphiphobic surfaces need to survive harsh conditions. To investigate the mechanical resistance, water drop impact and sand abrasion tests were performed. Sand grains, 100 to 300 μm in diameter impinged the surface from a height of 10 ~ 40 cm, corresponding to an impinging energy of $1\text{-}90{\times}10^{-8}$ J per grain (Fig. 4A). The silica shells were not sufficiently robust to completely sustain sand impact. A cave formed underneath the impacting area (Fig. 4C). However, zooming into the cave revealed an almost unaltered sub-

micrometer morphology (Fig. 4D). Owing to the coating's self-similarity, the surface kept its superamphiphobicity until the layer was removed after extended impact. The mechanical durability depends on the amount of sand impinging per unit of time and area, the size of the grains, the height of fall, and the thickness of the silica shell. The mechanical stability increases with the thickness of the silica shell, but at the expense of the coating's transparency. The surface retains its superamphiphobicity for 5 min sand abrasion from a height of 25 cm (2 m/s). (Movie S3). While the coating can be eroded through wear and abrasion it keeps its superamphiphobicity as along as its thickness remains above 1 μm (Fig. S11).

The coating consists of a fractal-like assembly of nano-spheres. With increasing duration of CVD of TES or annealing above 1100°C the necks between particles fill with silica and more rod-like shapes evolve, which reduces the superamphiphobicity (Fig. S8, S10). This can be understood from Nosonovsky's prediction that convex small-scale roughness can provide a sufficient energy barrier against wetting (*22, 31*), thus rendering superamphiphobicity possible. A spherical shape should provide a higher energy barrier against wetting than a rod-like shape (Figs. S8, S10).

Our easy to fabricate oil and water repellent coating is made from soot encased by a silica shell. The coating is sufficiently oil repellent to cause rebounding of impacting drops of hexadecane. Even low surface tension drops of tetradecane roll off easily when tilting the surface by 5°, taking impurities along. The surface keeps its superamphiphobicity after annealing at 400 °C. The coating is transparent and can be applied to a variety of heat resistant surfaces, such as aluminum, copper, or stainless steel.

References and Notes

1.   H. Y. Erbil, A. L. Demirel, Y. Avci, O. Mert, *Science* **299**, 1377 (2003).
2.   X. F. Gao, L. Jiang, *Nature* **432**, 36 (2004).
3.   X. M. Li, D. Reinhoudt, M. Crego-Calama, *Chem. Soc. Rev.* **36**, 1350 (2007).
4.   R. Blossey, *Nat. Mater.* **2**, 301 (2003).
5.   W. Barthlott, C. Neinhuis, *Planta* **202**, 1 (1997).
6.   L. C. Gao, T. J. McCarthy, *Langmuir* **22**, 2966 (2006).
7.   X. Deng *et al.*, *Adv. Mater.* **23**, 2962 (2011).
8.   J. Genzer, K. Efimenko, *Science* **290**, 2130 (2000).

9.   S. H. Kim, S. Y. Lee, S. M. Yang, *Angew. Chem. Int. Ed.* **49**, 2535 (2010).

10.   Z. Yoshimitsu, A. Nakajima, T. Watanabe, K. Hashimoto, *Langmuir* **18**, 5818 (2002).

11.   G. McHale, M. I. Newton, N. J. Shirtcliffe, *Soft Matter* **6**, 714 (2010).

12.   S. Shibuichi, T. Onda, N. Satoh, K. Tsujii, *J. Phys. Chem.* **100**, 19512 (1996).

13.   S. Singh, J. Houston, F. van Swol, C. J. Brinker, *Nature* **442**, 526 (2006).

14.   A. B. D. Cassie, S. Baxter, *Trans. Faraday Soc.* **40**, 0546 (1944).

15.   A. Lafuma, D. Quere, *Nat. Mater.* **2**, 457 (2003).

16.   G. Manukyan, J. M. Oh, D. van den Ende, R. G. H. Lammertink, F. Mugele, *Phys. Rev. Lett.* **106**, 014501 (2011).

17.   S. Herminghaus, *Europhys. Lett.* **52**, 165 (2000).

18.   Q. Xie *et al.*, *Adv. Mater.* **16**, 302 (2004).

19.   A. Tuteja, W. J. Choi, G. H. McKinley, R. E. Cohen, M. F. Rubner, *MRS Bull.* **33**, 752 (2008).

20.   A. Steele, I. Bayer, E. Loth, *Nano Lett.* **9**, 501 (2008).

21.   R. T. R. Kumar, K. B. Mogensen, P. Boggild, *J. Phys. Chem. C* **114**, 2936 (2010).

22.   L. Joly, T. Biben, *Soft Matter* **5**, 2549 (2009).

23.   A. Tuteja *et al.*, *Science* **318**, 1618 (2007).

24.   A. Ahuja *et al.*, *Langmuir* **24**, 9 (2008).

25.   L. Cao, T. P. Price, M. Weiss, D. Gao, *Langmuir* **24**, 1640 (2008).

26.   C. M. Megaridis, R. A. Dobbins, *Combust. Sci. Technol* **71**, 95 (1990).

27.   M. Callies, D. Quere, *Soft Matter* **1**, 55 (2005).

28.   D. Bartolo *et al.*, *Europhys. Lett.* **74**, 299 (2006).

29.   A. Tuteja, W. Choi, J. M. Mabry, G. H. McKinley, R. E. Cohen, *Proc. Natl. Acad. Sci. U. S. A.* **105**, 18200 (2008).

30.   D. Richard, C. Clanet, D. Quere, *Nature* **417**, 811 (2002).

31.   M. Nosonovsky, *Langmuir* **23**, 3157 (2007).

Supporting Information

Materials and Methods

Materials:

Tetraethoxysilane (TES) (Acros Organics, 98%), ammonia (VWR, 28%), (tridecafluoro-1,1,2,2-tetrahydrooctyl)-1-trichlorosilane (Sigma Aldrich, 97%), milli-Q water, diiodomethane, ethylene glycol, penaut oil (commercial), olive oil (commercial), hexadecane and tetradecane were used without further purification.

Characterization:

The morphology of the soot particles and the coating were characterized by low-voltage Scanning Electron Microscopy (LEO 1530 Gemini, Germany, and SU8000, Hitachi, Japan). After calcination the hollow silica networks were imaged by Transmission Electron Microscopy (FEI, 200 kV). Static, advancing, receding, and roll off angles were measured with a contact angle meter, Dataphysics OCA35 (Data Physics Instruments GmbH, Germany). Transmission was measured using an ultraviolet-visible spectrometer (Lambda 900, Perkin Elmer) in double-beam mode, using an uncovered glass slide as a reference. High speed movies were taken with a high speed camera (Photron, Fastcam SA1).

Methods:

Chemical vapor deposition of TES: The soot coated substrates (glass or silicon) were placed in a desiccator together with two small glass vessels containing about 2 ml of tetraethoxysilane (TES) and ammonia, respectively (Fig. S1). The desiccator was closed again and chemical vapor deposition (CVD) of TES was carried out for 24 h, if not stated otherwise. Similar to a Stöber reaction, silica is formed by hydrolysis and condensation of TES catalysed by ammonia.
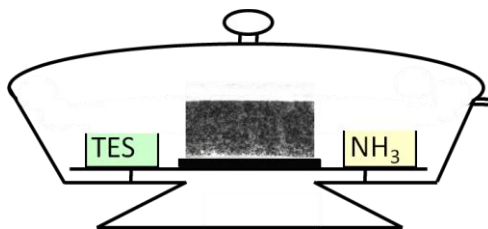
Fig. S1. Sketch of a desiccator together with the soot coated substrate (middle) and two glass vessels, containing tetraethoxysilane (TES) and ammonia (NH_3), respectively.

After calcination of the fractal-like carbon/silica network at 600°C for 2 h in air, the hydrophilic silica coating is hollow. To transform it into a superamphiphobic coating chemical vapor deposition (CVD) of a semi-fluorinated silane on the films was performed. Therefore, the coated substrate and a small glass vessel containing about 0.1 ml of silane were put in a desiccator for 3 h. To increase the vapor pressure of silane the desiccator was evacuated for a few minutes. Afterwards the vessel containing the silane was removed from the desiccator and vacuum was applied for one hour in order to remove unreacted silane residues.

The thickness of the coating increases with the amount of deposited soot. The average soot density is independent of height, i.e. the porous layer is uniform. The homogeneity of the deposition is reflected in the sharpness of the soot – air interface (Fig. S2). SEM images of the cross section of the coating underpin the coating's self-similarity.
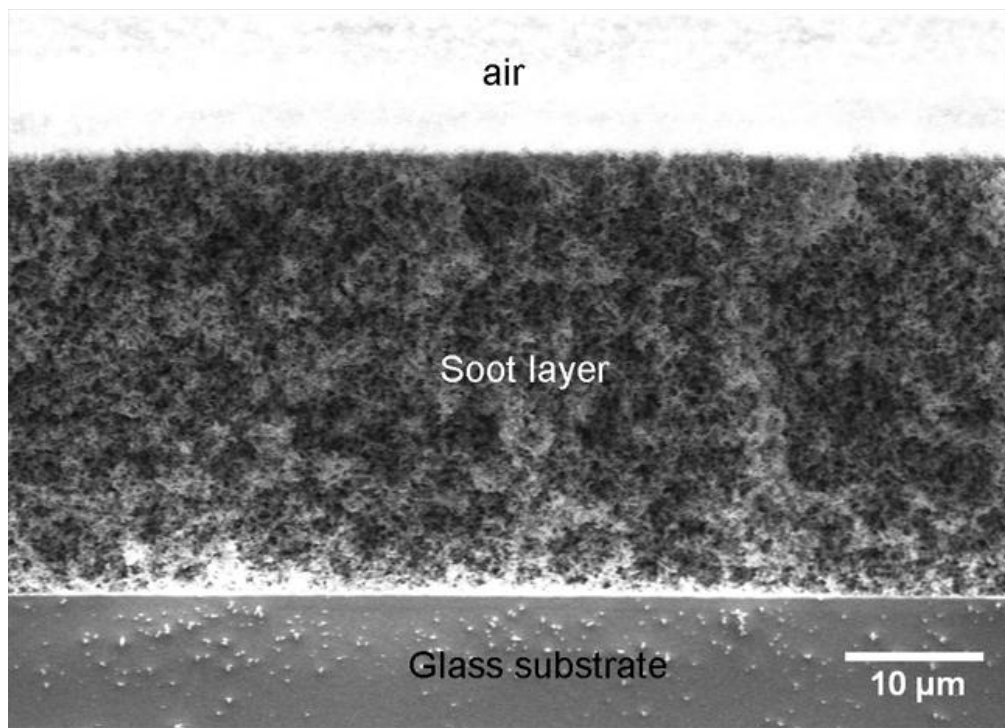
Fig. S2. SEM image of a cross section of a superamphiphobic film. After holding the glass substrate for 25 s in a candle flame 33 ± 3 μm thick soot was deposited. For mechanical stability the soot layer was coated with 20 ± 5 nm thick silica and annealed at 600 °C for 2 h.

Contact angle hysteresis

The advancing and receding contact angles were measured by titrating 3 μl (10 μl) water (hexadecane) to a 3 μl (5 μl) drop and removing the solvent afterwards (Fig. S3). The data were analyzed using Image Pro Plus (Media Cybernetics). The contact angles depend on the choice of the baseline. Due to the roughness of the coating the substrate always appears a bit blurred, making a precise location of the three-phase contact line difficult. The data were evaluated using Image Pro Plus, because this image analysis and processing software offers the option to increase the contrast, thereby reducing the error in determining the baseline. Water drops possess contact angles above 160° and show low hysteresis, $CA_{adv} - CA_{res} = (165° \pm 1) - (163° \pm 1°) \approx 2°$ (Fig. S3 A). Both, the advancing and receding contact angle for drops of hexadecane are slightly lower ($CA_{adv} = 158° \pm 1°$, and $CA_{res} = 152° \pm 1°$). Still, its hysteresis is small, $CA_{adv} - CA_{res} \approx 6°$, proving the coatings superamphiphobicity.
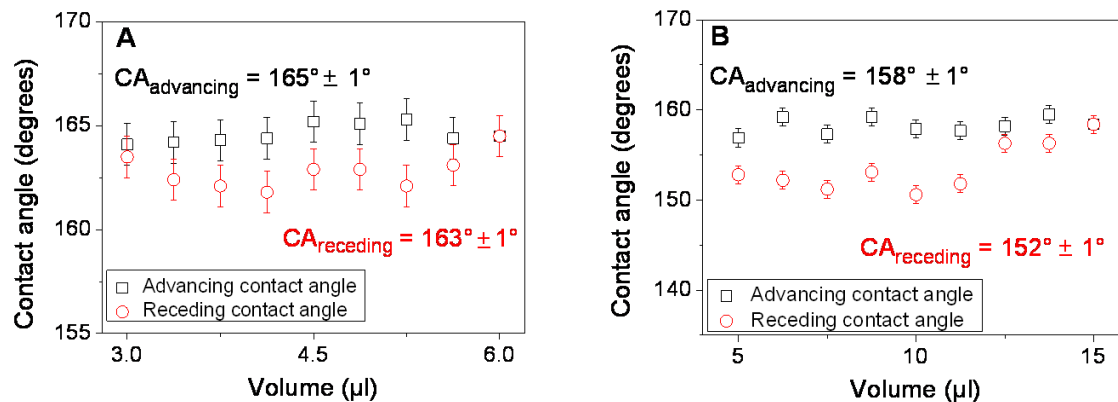
Fig. S3. (A) **Advancing and receding contact angle for water and** (B) **hexadecane.**

Hexadecane drop impact

The impact of hexadecane drops was investigated at various velocities. The falling height varied between 4 mm and 30 cm. Fig. S4 shows images of hexadecane drops 1 ms after lifting off. For heights of fall up to 5 cm the drops completely rebounded. This corresponds to an impact velocity of 1 m/s and a Weber number of $We = \frac{\rho R v^2}{\gamma} = 23$, where ρ is the density, R the radius of the drop, v its impact velocity, and γ the liquid-air surface tension. The contact time of the drop with the coating increased from 10 ms (0.4 cm drop height) to 14 ms (5 cm). Impinging from 8 cm height left a small satellite droplet on the surface. The size of the satellite droplet increased with the height of fall. The corresponding impact velocities, Weber number, and area of the pinned satellite droplet on the coating are listed in Table S1.

Fig. S4. Snapshots of 5 μl hexadecane drops after impinging on a superamphiphobic surface from different heights of fall. The images were taken 1 ms after lifting off. The red line marks the height of fall, separating the region of complete rebound and partial pinning.

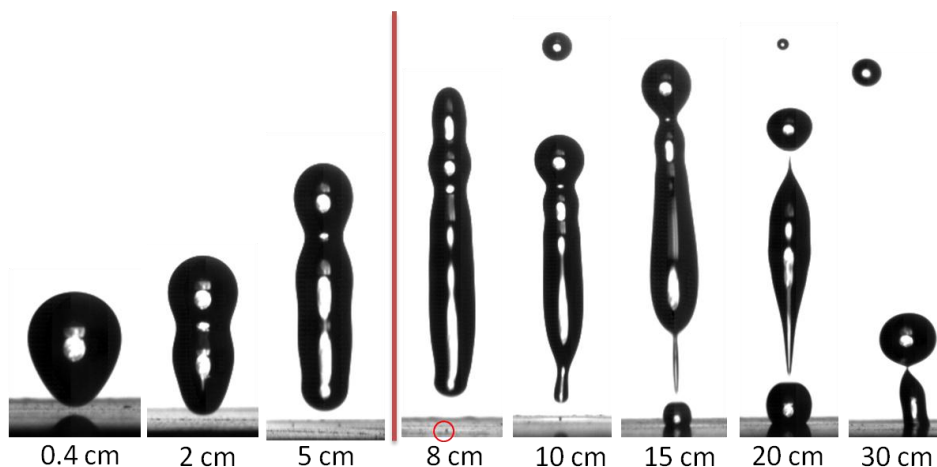| Height of fall (cm)	Impact velocity (m/s)	Weber number	pinning area (mm^2)
0.4	0.3	2	0
2	0.6	10	0
5	1	23	0
8	1.3	37	0.001
10	1.4	47	0.004
15	1.7	69	0.61
20	2.0	96	1.5
30	2.4	138	1.8

Table S1. Height of fall, impact velocity v, Weber number We, and contact area of the pinned satellite drop on the coating. Drop radii: R = 0.85 mm, surface tension of hexadecane: γ = 27.5 mN/m, Density: ρ_{HD} = 0.77 g/ml, Weber number: $We = \frac{\rho R v^2}{\gamma}$.

Fig. S5 shows details of the rebound of a 5 μl hexadecane drop impinging on a superamphiphobic surface at a velocity of 1.4 m/s. After the drop hit the surface at time t = 0 s, it first expanded (t = 0.93 ms), retracted (t = 7.6 ms) and then rebounded (t = 27.2 ms). The drop considerably deformed and ejected satellite drops. At the bottom of the elongated drop, a tiny satellite drop formed that stuck to the surface. This pinned satellite drop is marked by the white circle. However, this pinning is reversible. While the hexadecane drop re-impacted the surface at t ≈ 60 ms the pinned satellite drop merged with the original drop. The full drop bounced back (t = 70.1 ms), which proves the repellency of the surface to low interfacial tension liquids like hexadecane.
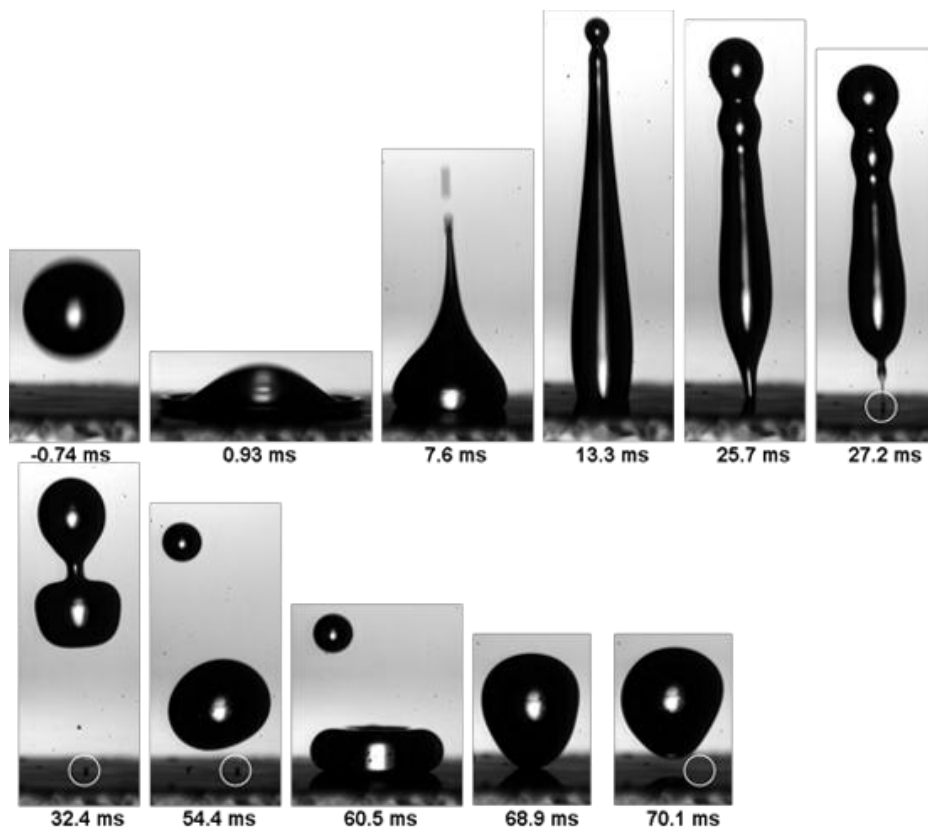
Fig. S5. Details of the rebound of a 5 µl hexadecane drop impinging on a superamphiphobic surface at a velocity of 1.4 m/s.

Drop impact resistance

The durability of the coating towards long-term drop impact was tested, letting water drops impinge a 5 µm thick coating from 1 cm and 10 cm, respectively, Fig. S6. For a falling height of 1 cm (impact velocity of 0.44 m/s) the coating did not show hints of altering after 360 000 drop impacts, i.e. the coating remained superamphiphobic. After impinging of 12000 water drops from 10 cm height (1.4 m/s) the coating lost its superhydrophobicity.
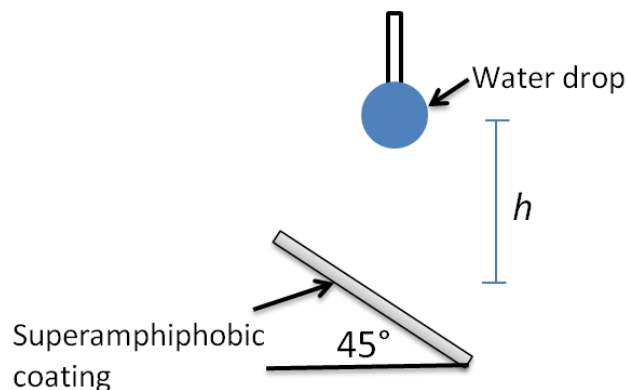
Fig. S6. Sketch of the setup to test the coating's long term resistance against drop impact. 1 mm sized water drops impinged a 5 µm thick coating from a falling height of 1cm and 10 cm, respectively. The substrate was tilted by 45° and fixed above a sink to ensure water drain off.

Self-cleaning

    Sand (white dots in Fig. S7) polluted superamphiphobic coatings were rinsed by water and hexadecane. Both solvents enwrapped the sand and took it away while the drops rolled off the surface.
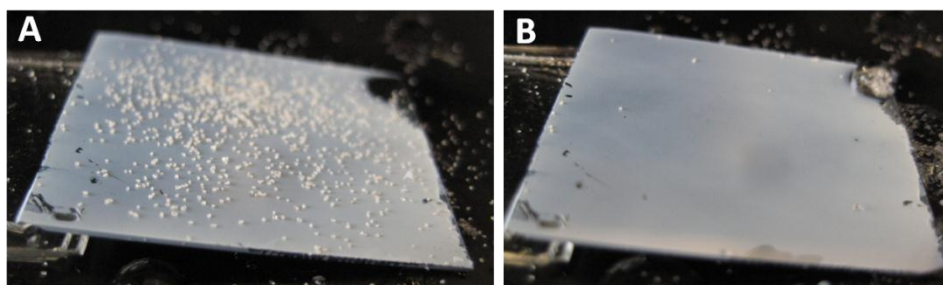
Fig. S7. Sea sand polluted superamphiphobic surface (A) before and (B) after hexadecane drops took up the contaminants encountered on its way.

Temperature stability

    The static contact and roll-off angle remained unchanged after heating up to 400 °C for 1 h (Fig. 3A in the manuscript). Heating the coatings at even higher temperatures decomposed the

fluorosilane, causing that the coating lost its superamphiphobicity. The silica network turned hydrophilic. Superamphiphobicity can be recovered by CVD of a fluorosilane. Annealing the coating at 1100°C caused onset of sintering. This is reflected in a smoothening of the silica strings (Fig. S8 B). Still, the coating kept its self-similarity (Fig. S8 A). After CVD of a fluorosilane the sintered layer remained superhydrophobic but lost its superamphiphobicity (Fig. S8 C,D).
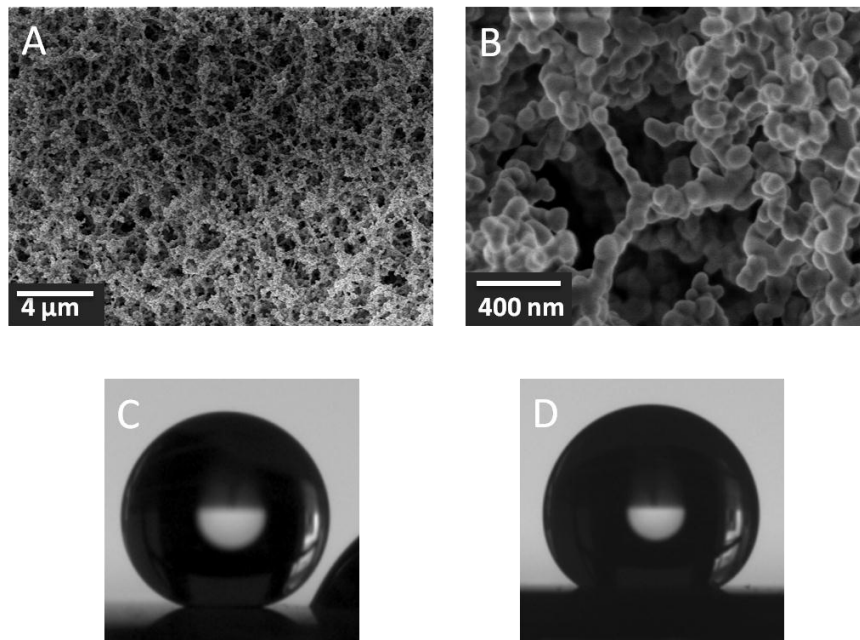
Fig. S8. (A, B) SEM images taken after annealing an initially superamphiphobic coating at 1100°C for two hours. After CVD of a fluorosilane the contact angles with water **(C)** and hexadecane **(D)** were 163° (roll off angle: 2°) and 149° (roll off angle > 60°), respectively.

Transparency of the coating

The transparency of the coating depends on its thickness as well as on the thickness of the silica shells (Figs. S9, S10). The coating's transmittance most pronounced decreased at short wavelengths. Whereas the transmittance of 1µm thick coatings closely resembled those of pristine glass, 45 µm thick coatings showed 50 % transmittance only for wavelengths above 500

nm. The transmittance strongly decreased with the thickness of the silica shells (Fig. S10 B). Recently, Retsch et. al. calculated the dependence of the transmittance of hollow silica spheres on particle size and shell thickness (*1*). They observed a pronounced dependence of the transmittance on the shell thickness in line with our observations.
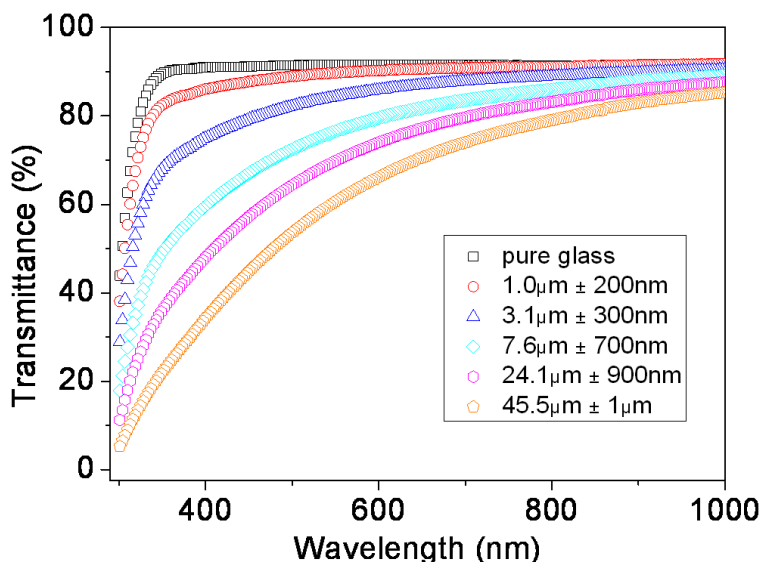
Fig. S9. UV-VIS transmittance spectra of coatings of different thickness. The average thickness of the coating increased 1 μm to 45 μm (top to bottom). The black squares show the wavelength dependent transmittance of pristine glass. CVD of TES was performed for 24 h on all coatings.

Sand impact resistance

For the sand abrasion test 20 g of commercial sand (diameter: 100 μm to 300 μm) impacted the surface from a height between 5 and 40 cm, while the substrate was held at 45° to the horizontal surface. The mechanical stability increased with the thickness of the silica shell, which increased with the period of CVD of TES. Sand abrasion tests of the coating were performed after 1 day, 2 days, and 3 days of CVD of TES. After 3 days CVD of TES the coating can stand 5 minutes impact of 100 to 300 μm sized sand grains, impacting at a velocity of 8 km/h (40 cm), details in Table S2. Compared to these large particles, aerosol particles have radii below 10 μm (*3*). Taking smaller grains should strongly increase the impact duration or impact velocity, due to

decreased impact energy (*4*). A predictive description of the coatings mechanical stability is not yet available because breakage depends on sample history (*2*), as well as on details of the fractal-like silica network, such as local density, shell thickness, angles between neighboring strings, etc. Thicker coating can provide longer damage resistance, both, against drop and sand impact. Thick shells are mechanically more stable, but less transparent (Fig. S9 B) (*1*). After 3 days of CVD of TES the fractal pearl necklace-like morphology of the silica strings smoothened and the strings turned more rod-like (Fig. S10). The average string-string distance decreased as did the coating's superamphiphobicity. After 3 days of CVD of TES the hexadecane drops showed a SCA of 145° and a roll off angle of 40°. The contact and roll off angle remained unchanged for water.
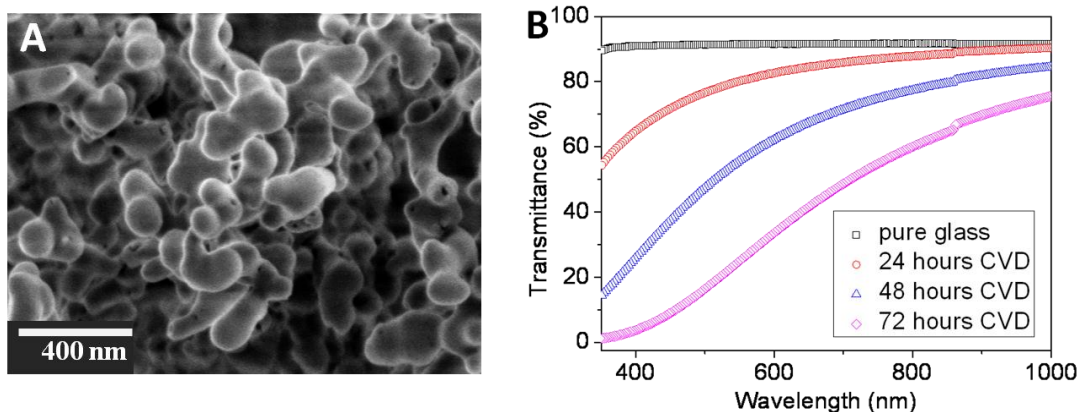
Fig. S10. **(A)** SEM image of the coating after performing CVD of TES for 72 hours. **(B)** Transparency of a 8 μm thick silica porous film after different times of CVD of TES.

Time of CVD of TES	Thickness of silica shell	Transparency	Impact velocity$_{SA}$
24 hours	20 ±5 nm	77%	1.4 m/s
48 hours	35 ±5 nm	47%	1.7 m/s
72 hours	60 ±10 nm	17%	2.2 m/s

Table S2. Dependence of the duration of CVD of TES on the thickness of the silica shells, the coatings transparency at a wavelength of 500 nm, and impact velocity$_{SA}$ of the sand grains. The thickness of the coating was taken to be 8 μm for all samples. At the given impact velocities$_{SA}$

the surface remained superamphiphobic after 5 min sand abrasion. For longer impact duration the impact damages the coating that can be observed optically.

Supporting references:

S1. M. Retsch, M. Schmelzeisen, H.-J.Butt, E. L. Thomas, *Nano Lett*. **11**, 1389 (2011).

S2. S. Aman, J. Tomas, H. Kalman, *Chem. Eng. Sci*. **65**, 1503 (2010).

S3. A. S. Ahmed, A. A. Ali, M. A. Alhaider, *Atmospheric Environment*. **21**, 2723 (1987).

S4. X. Deng *et al.*, *Adv. Mater.* **23**, 2962 (2011).

Chapter 4: Liquid drops impacting superamphiphobic coatings

Xu Deng,[1,2] Frank Schellenberger,[1] Periklis Papadopoulos,[1] Doris Vollmer[1*], Hans-Jürgen Butt[1*]

[1]Max Planck Institute for Polymer Research, Ackermannweg 10, 55128, Mainz, Germany

[2]Center of Smart Interfaces, Technical University Darmstadt, 64287 Darmstadt, Germany

*Corresponding authors: butt@mpip-mainz.mpg.de, vollmerd@mpip-mainz.mpg.de

ABSTRACT

The dynamics of liquid drops impacting superamphiphobic coatings is studied by high speed video microscopy. Superamphiphobic coatings repel water and oils. The coating consists of a fractal-like hydrophobized silica network. Mixtures of ethanol-water and glycerin-water are chosen to investigate the influence of interfacial tension and viscosity on spreading and retraction dynamics. Drop spreading is dominated by inertia. At low impact velocity the drops completely rebound. However, the contact time increases with impact velocity, whereas the restitution coefficient decreases. We suggest that the drop temporarily impales the superamphiphobic coating, although the drop completely rebounds. From an estimate of the pressure is can be concluded that impalement is dominated by depinning rather than sagging. With increasing velocity the drops partially pin and an increasing amount of liquid remains on the coating. A time-resolved study of the retraction dynamics reveals two well separated phases: a fast inertia-dominated phase followed by a slow decrease of the contact diameter of the drop. The crossover occurs when the diameter of the retracting drop matches the diameter of the drop before impact. We suggest that the depth of impalement increases with impact velocity, where impalement is confined to the initial impact zone of the drop. If the drop partially pins on the coating the depth of impalement exceeds a depth preventing the whole drop to be removed during the retraction phase.

INTRODUCTION

Impact dynamics of liquid drops is of high importance in a variety of industrial processes such as rapid spray cooling, spray painting and coating, precision solder-drop dispersions in microelectronics, or deposition of pesticides on plant leaves.[1-3] Of special importance is the transition regime between complete rebound and pinning since here the wetting behavior of surfaces change. The interfacial tension, the viscosity of the liquid, the height of impact, and the chemical and physical properties of the surface determine the spreading and retraction dynamics. An impacting drop may homogeneously wet a surface, roll-off after impact, or stick to a small area not much larger than the initial diameter of the drop.[4-7] A drop can also rebound or fall apart into many tiny drops. Complete rebound is desired for water-repellent coatings of textiles,[8] walls,[9] glasses,[10] or solar cells.[11-12]

Superhydrophobic surfaces are characterized by high apparent contact angles for drops of water of $\Theta_{app} \geq 150°$. In addition, a drop rolls off when tilting the substrate by more than $5°$.[13] This low roll-off angle is due to a low adhesion of the drop on the surface, resulting from the combination of a low energy surface and roughness on the nano- or micrometer scale.[14-19] A gently deposited drop does not wet the underlying substrate but is supported by hydrophobic protrusions. In the interstitial space air cushions separate the drop from the substrate (Cassie state).[20] A drop can wet the substrate (Wenzel state).[21] if it impacts with a high enough velocity or kinetic energy.[12,22] This threshold impact velocity depends on the surface morphology and the chemical and physical properties of the surface and the liquid. Furthermore, superhydrophobic surfaces are still wetted by surfactant solutions and organic liquids such as alcohols or alkanes.[23-24]

Superamphiphobic surfaces instead repel these organic liquids, in addition to water.[1] The fundamental difference between water and non-polar liquids is the contact angle on flat low-energy surfaces. Water can form a contact angle above $90°$ with these surfaces. In contrast, no flat surface exists (to our knowledge) that forms a contact angle above $90°$ with non-polar liquids. According to Young's equation the materials contact angle Θ_0 of the liquid with a flat, undeformable, inert, homogeneous substrate is given by the interfacial energies, $\cos\Theta_0 = (\gamma_{SV}$-

---

[1] We use the term *superamphiphobic* rather than –*omniphobic* or *oleophobic*. Omniphobic comes from the Latin word „omni" for "all". So far no surface has been fabricated that is superomniphobic for highly volatile liquids such as pentane or for fluorinated solvents. Our surface neither repels ethanol, methanol, acetone, or THF. Therefore, we consider the term superomniphobic as too comprehensive. Oleophobic only refers to oils but not to ionic liquids, blood, or soap solutions.

$\gamma_{SL})/\gamma$.[25-26] Here, γ_{SV} is the solid-vapour, γ_{SL} the solid-liquid, and γ the liquid-vapour interfacial tension. In water, mercury, and few other polar liquids, the interaction between the liquid molecules among themselves is so strong, that it requires high energy to create solid-liquid interface. As a result, $\gamma_{SL} > \gamma_{SV}$ and Θ_0 can be higher than 90°. For organic liquids γ is typically 15 - 40 mN/m. Mainly van der Waals interactions act between the liquid and the hydrophobized substrate. Therefore γ_{SL} is low, $\gamma_{SV} - \gamma_{SL}$ is positive, and $\Theta_0 < 90°$. Thus, to create surfaces with an apparent contact angle above 150° and a low roll-off angle with non-polar liquids, microscopic overhanging structures that prevent the liquid from sliding down the protrusions are necessary.[23-24, 27] One example is a coating consisting of fractal-like aggregates of nanoscopic spheres (Fig. 1).[28-29]. The air cushion (Cassie state) is maintained and the apparent contact angle can be larger than 150°. The Cassie state of a non-polar liquid on a superamphiphobic coating is only metastable. Once the liquid has penetrated the coating is will remain inside.
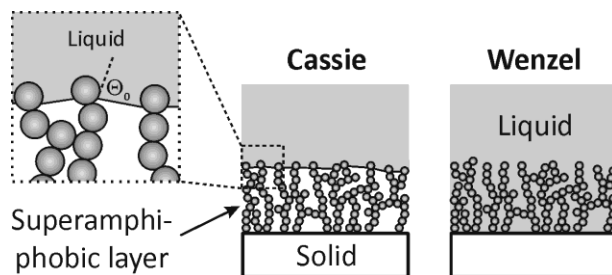
Figure 1. Schematic of a liquid resting on a superamphiphobic coating consisting of fractal-like aggregates of microscopic spheres. Although the liquid forms a material's contact angle $\Theta_0 <$ 90°, the energy barrier is sufficient to prevent the liquid-air interface from sliding down the aggregates at the underside of the spheres. Air can be entrapped leading to the Cassie state.

Penetration of a superhydro- or superamphiphobic coating is more likely during drop impact, because of the instantaneous high pressure. The dynamics of drop impact was investigated by varying the impact velocity and geometric parameters of regular and random superhydrophobic surfaces, such as the mean spacing, diameter, and height of protrusions, for liquids of high interfacial tension and low viscosity.[12, 22, 30-36] For superamphiphobic surfaces a characterization

by drop impact is even more important since impalement of non-polar liquids leads to a permanent breakdown of the Cassie state.[23, 37] Furthermore, superamphiphobic surfaces allow a systematic investigation of the impact dynamics of drops with low interfacial tension.

In this article, we investigate the transition regime between complete rebound and partial pinning by varying the impact velocity, interfacial tension, and viscosity. The drops consist of mixtures of water with glycerol or ethanol. By varying the glycerol concentration, the liquid viscosity is tuned, keeping the liquid density and its interfacial tension nearly constant. Varying the ethanol concentration changes the interfacial tension while the viscosity varies only slightly.

Before starting with results we summarize the quantitative description of drop impact. Impact dynamics is subdivided into two phases: a spreading and a retraction phase. In the spreading phase an impacting drop experiences an effective acceleration that flattens the drop and determines its maximal lateral extent.[38] In this process the kinetic energy of a drop just before impact is partially converted to interfacial energy of the deformed drop.[35, 39]

At the limit of low impact velocities the deformation of the drop is small compared to its diameter. In this case the bouncing of a drop of low viscosity can be modeled by a spring of stiffness γ and mass $\approx \rho R^3$, oscillating with a constant period $\tau_0 \approx \sqrt{\rho \pi^2 R^3 / 2\gamma}$.[40-43] Here, R is the initial radius of the drop. The period of the oscillations shows good correlation with the lowest Rayleigh frequency of the drop.[43]

Oscillations of the rebounding drop and residual flow in the drop cause dissipation of energy. Therefore, the restitution coefficient [44-46] defined as the ratio of the velocity directly after, v_a, and before, v_0, rebound, $C_R \equiv |v_a / v_0|$, is lower than one. The amount of energy dissipation during spreading and retraction determines the minimum impact height such that a drop has sufficient energy to rebound.

The ratio of the drop's kinetic to surface energy can be described in terms of the dimensionless Weber number: $We \equiv \rho v_0^2 R / \gamma$. With increasing We the maximum lateral extension of a low viscous drop increases. At sufficiently high We the rim breaks up and the drop splashes. For low-viscous drops the maximal spreading diameter D_{max} scales as $D_{max} / D_0 \propto We^{1/4}$.[38, 42] $D_0 = 2R$ is the initial diameter of the drop.

Bonn et. al. noted that the retraction dynamics of water-glycerol drops on flat hydrophobic surfaces can be divided into two distinct regimes.[45] They observed, that at higher Weber number the retraction rate is independent of impacting velocity and at fixed viscosity the evolution of $D(t)/D_{max}$ collapsed on one curve for all impact velocities investigated. With increasing viscosity the retraction rate, $\dot{\varepsilon} = \max|-dD(t)/dt|/D_{max}$ crosses from a capillary-inertia dominated regime to a capillary-viscous regime. The cross-over occurs at an Ohnesorge number close to $Oh \approx 0.05$, where the Ohnesorge number, $Oh \equiv We^{1/2}/Re = \eta/\sqrt{\rho R \gamma}$, compares the dissipative viscous forces to the non-dissipative capillary forces. The Reynolds number $Re \equiv \rho v_0 R_0 / \eta$ compares the ratio of inertial to viscous forces.[6-7, 38] Contrary to the impact dynamics on a flat surface, on a rough surface a drop can impale the coating. Impalement of a drop into the coating may cause pinning of the drop (Cassie-to-Wenzel transition).[22, 30, 47] The degree of impalement depends on the applied pressure,[48] which increases with the impact velocity v_0. Impalement can come about in at least two ways: by sagging or depinning. For sagging, the curvature of the liquid interface reaches a value set by the geometry of the pattern such that the liquid touches the substrate.[30, 47, 49] The antiwetting pressure for sagging is of the order of $P_{sag} \approx \gamma / r$, where r is the distance between neighboring protrusions. It can be approximated as $P_{sag} \approx 40$ kPa, assuming a spacing between neighboring particle strings or aggregates of $r \approx 1$ μm and $\gamma \approx 0.04$ N/m. This pressure needs to be compared to the dynamic wetting pressure $P_D = 0.5\rho v_0^2$, which ranges from 0.1 kPa for $v_0 = 0.5$ m/s to 3 kPa for $v_0 = 2.5$ m/s. Thus, $P_D < P_C$ and sagging is unlikely to lead to impalement.

For superamphiphobic surfaces depinning impalement is likely to occur at lower pressure than sag impalement.[29] For depinning impalement, the liquid-air interface depins from the top of the pillars and moves downwards.[48, 50-52] For our superamphiphobic surface (Fig. 1, 2a) depinning occurs when the liquid detaches from the top sphere and slides down the aggregates of nanospheres. For the ideal situation of a square array of vertical pillars consisting of spherical particles with diameter a at a spacing r the critical pressure for depinning impalement is [29]

$$P_{dep} = \frac{\pi \gamma a}{r^2} \sin^2 \frac{\Theta_0^a}{2} \qquad (1)$$

With typical values of $a = 60$ nm, $r = 1$ µm, advancing contact angle $\Theta_0 = 75°$, and $\gamma = 0.04$ N/m we obtain $P_{dep} = 2.8$ kPa. It decreases to $P_{dep} = 0.7$ kPa for $r = 2$ µm. It should be noted that for our fractal-like arrangement of nanospheres the distance between neighboring aggregates varies, i.e. a drop will impale the coating first at positions with largest distances between neighboring aggregates (Fig. 2a). Therefore, P_{dep} can locally fall below P_D for sufficiently high impact velocities. Impalement and the resulting impact scenario should therefore depend on the ratio of the Bernoulli pressure and the pressure for depinning impalement.

2. EXPERIMENTAL SECTION

Materials. Tetraethoxysilane (TES) (98 %) was purchased from Acros Organics, 1H,1H,2H,2H-perfluorodecyldimethylchlorosilane (tech. 90 %) from Alfa Aesar, ethanol absolute and glycerin from Sigma Aldrich. All chemicals and solvents were used without further purification. Milli-Q water was obtained from a Millipore purification system operating at 18.2 MΩ. Glass slides and silicon wafers used as substrates were sonicated twice in a 2 % Hellmanex II solution (Hellma GmbH), extensively rinsed with Milli-Q water and dried with nitrogen before usage.

Fabrication of superamphiphobic surfaces. Superamphiphobic surfaces were fabricated by a template technique. First, an about 20 µm thick coating of soot was deposited on a glass substrate. The soot consisted of 30 to 50 nm sized almost spherical particles forming a porous network of particle chains and small particle aggregates. To increase the mechanical stability the soot coatings were coated with a silica shell making use of chemical vapour deposition (CVD) of tetraethoxysilane (TES) catalysed by ammonia. Afterwards, the soot-coated substrates were placed in a desiccator together with two open glass vessels containing tetraethoxysilane (TES) and ammonia, respectively. Silica formed by hydrolysis and condensation of TES. After 24 h of CVD the particles were coated by a 20 ± 5 nm thick silica shell (Fig. 2). SEM images show that the coating kept its high porosity even after the soot particles were encased in a silica shell (Fig. 2a). After calcination the hybrid carbon/silica network at 600 °C for 2 h the coating turned transparent. This silica coating was hydrophilic and became superamphiphobic after hydrophobization with a semi-fluorinated trichlorosilane. Further details are given in Deng et. al. [28]
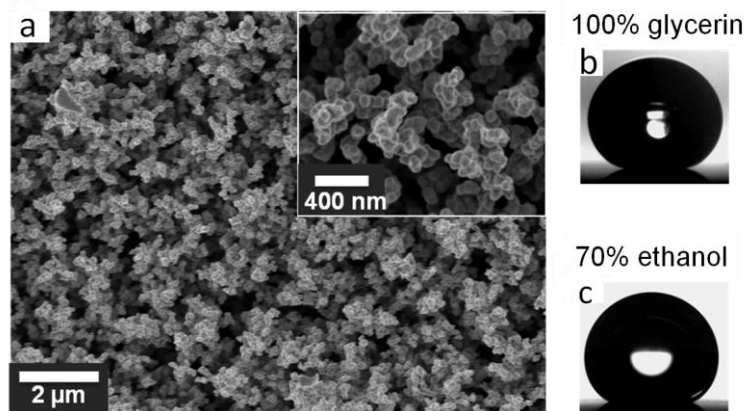
Figure 2. (a) SEM images of the morphology of the superamphiphobic coating. Inset: High magnification image after coating the soot particles with a 20 – 30 nm thick silica shell. (b) A 5 µl drop of pure glycerin shows a contact angle of 161° and a roll off angle of 1°. (c) A 4 µl drop containing 70% ethanol shows a static contact angle of 151° and a roll-off angle larger than 90°.

Characterization. The morphology of the substrate and of the particles was characterized by Scanning Electron Microscopy (SEM, LEO 1530 Gemini, Zeiss, Oberkochen, Germany) and a Hitachi SU8000 (Hitachi High-Technologies Europe GmbH, Krefeld, Germany) at low operating voltages (0.5 – 1.4 kV).

Contact angles were measured with the sessile drop method (OCA35, Data Physics Instruments GmbH, Germany). Static contact angles were measured after depositing a liquid droplet of 5 µl on the surface. For each sample, the contact angle was measured at 5 different places and the arithmetic mean was calculated. The roll-off angle was measured after depositing a 5 µl drop on the surface and tilting the stage, while recording the movement of the drop by a CCD camera.

Drop impact experiments. Mixtures of ethanol and glycerol with water were prepared (Table 1). Mixtures with more than 70% ethanol wetted the substrate already after a few seconds. Liquid drops were released from heights between 0.2 and 40 cm. The impact, spreading, and retraction process were imaged with a high speed camera (Photron, Fastcam SA-1) in side view at 5400 frames/s.

Liquid	D_0 (mm)	ρ (kg/m^3)	γ (mN/m)	η (mPa·s)	Θ_{app}	α	Θ_{app}^{flat}
Water	2.4	998	72	1.0	165°	1°	102°
20% ethanol	2.2	969	39	2.2	157°	2°	82°
40% ethanol	2.0	935	31	2.9	155°	3°	75°
50% ethanol	2.0	914	29	2.9	154°	4°	67°
70% ethanol	1.8	868	26	2.5	151°	> 90°	54°
20% glycerin	2.4	1047	67	1.8	164°	1°	101°
40% glycerin	2.4	1099	66	3.7	164°	1°	102°
60% glycerin	2.4	1154	65	11	164°	1°	102°
80% glycerin	2.4	1209	64	60	164°	1°	101°
90% glycerin	2.4	1235	63	220	164°	1°	102°
100% glycerin	2.4	1261	63	1410	161°	1°	102°

Table 1. Volume fractions of ethanol-water and glycerin-water drops, initial drop diameter D_0, density ρ, interfacial tension γ, and viscosity η, at 20°C.[53-55] Apparent contact angles Θ_{app} and roll off angles α of various ethanol-water and glycerin-water drops on superamphiphobic surfaces and the material contact angle Θ_{app}^{flat} on flat hydrophobized surfaces. The standard deviation for Θ_{app}^{flat} is ± 1°. The standard deviation for Θ_{app} is ± 3°. Note, the contact angle depends on the size of the drop, how it is deposited on the surface, and the optical resolution of the device.

Contact and roll-off angles. Gently deposited drops showed static contact angles exceeding 150° and roll-off angles were below 5°, except for the 70% ethanol solution (Table 1). Mixtures of water and ethanol containing 70% ethanol did not roll off (roll-off angle above 90°), because the drop impaled the coating (Fig. 2c). For glycerin-water mixtures the static contact angle exceeded 160° and the roll-off angle was close to 1° for all mixing ratios (Tab. 1).

3. RESULTS AND DISCUSSION

Time-resolved impact. Fig. 3a shows snapshots of drops of 50% ethanol-water mixture impacting a superamphiphobic coating from different heights, i.e. at different velocities, v_0. The images in the first row show drops just before impact. We define $t = 0$ as the time where the drop first contacts the coating. Before impact the drops are almost spherical with diameter D_0. After impact the drops spread until they reach a maximal spreading diameter, D_{max} (second row). Its shape resembles a cylindrical lamella. At low velocities, that is in the velocity range $0.1 \leq v_0 \leq 0.4$ m/s, D_{max} only slightly exceeds D_0 (second row, first column). For $v_0 \leq 0.1\,\text{m/s}$ the kinetic energy of the drop is insufficient for the drop to rebound, i.e. it sticks to the surface.[38] With increasing impact velocity the diameter of the lamella increases and its thickness decreases. At $v_0 \geq 2.4\,\text{m/s}$ the rim of the ethanol-rich lamella becomes unstable, the drop splits up into many small droplets and splashes (Fig. 3, third row).

In the retraction phase the shape depends on composition and height of fall. The drops completely rebound, partially pin on the surface, or they splash. At low impact velocities, ($v_0 = 0.4\,\text{m/s}$) the drops retract and rebound (first column). At increasing impact velocity the rebounding drops elongate. For $v_0 \geq 1$ m/s the bottom part of the elongated ethanol-rich drops irreversibly pin on the surface (Video S1). The amount of pinned material increases with v_0 second column). Increasing the impact velocity even further leads to rupturing of the drops and formation of satellite droplets (third column). The qualitative behavior of the impact dynamics for glycerin-rich drops is identical, instead completely rebound until v_0 = 2.4m/s (Video S2). With increasing impact velocity the drop strongly elongates and the contact time with the surface increases, even the drop completely rebounds (Fig. 3b, second column). Thus, the outcome of the retraction phase depends qualitatively on both impact velocity and composition.
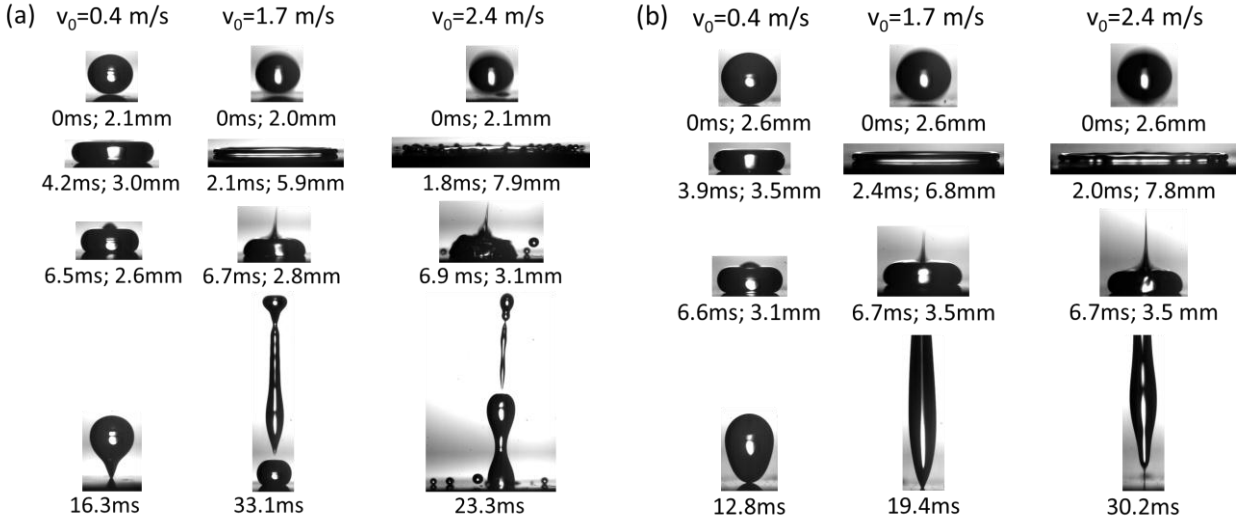
Figure 3. Time resolved bouncing of drops of 50% ethanol-water (a) and 60% glycerin-water (b) mixtures at different impact velocities. The impact velocities 0.4 m/s, 1.7 m/s, and 2.4 m/s correspond to a release height of 0.8 cm, 15 cm, and 30 cm, respectively. The first row shows a picture of the drop just before impact. The second row shows the drops at maximal deformation, D_{max}, and the third row about 7 ms after impact. The pictures in last row show the last image before the drop pinches-off or just before partial rebound. The numbers under each image refer to the time after the drop first touches the surface and the diameter of the drop.

Rebound, pinning and splashing. To identify the experimental parameters which determine drop impact we plot *We* versus *Re* and indicate the specific impact scenario (Fig. 4a,b). For ethanol-water the drops completely rebound at low *We* (roughly ≤ 4), i.e., at impact velocities, $v_0 \leq 0.8$ m/s. For *We* ≥ 4–10, drops remain partially pinned (red symbols). Close to but just below the transition rebound - partial pinning the drops strongly elongate (Video S3). For *We* just above the transition only a tiny amount of liquid remains on the surface (Video S1). With increasing *We* the relative amount of residual liquid increases gradually. At high *We* ≥ 50–200 also splashing is observed (blue symbols).

The impact scenarios for mixtures of glycerin-water resemble those for mixtures of ethanol-water (Fig. 4b). However, drops consisting of glycerin-water mixtures rebound in a wider range of *Re* and *We* (Video S2*)*. Again, increasing *We* induces pinning of the drops on the surface,

84

where the relative amount of residual liquid increases gradually. At sufficiently high v_0 the drop pinches at its top and one or more satellite drops are ejected. With increasing viscosity the transition towards splashing shifts to higher We.
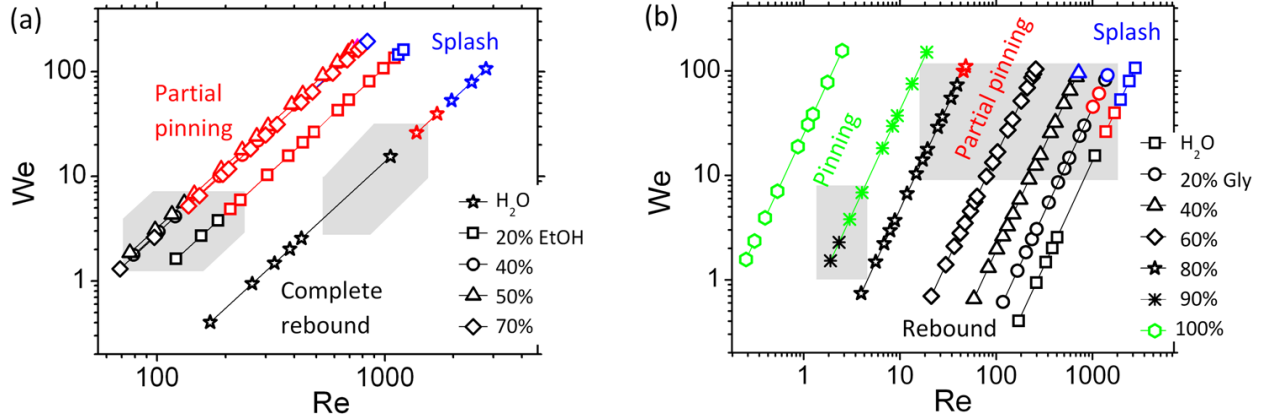

Figure 4. Weber number versus Reynolds number for (a) ethanol-water drops and (b) glycerin-water drops impacting on a superamphiphobic surfaces. The symbols connected by a solid line belong to drops of equal composition but different impact velocity; (a) ethanol concentration: stars 0%; squares: 20%, diagonals: 40%, spheres: 50 %, triangles: 70% (b) glycerin concentration: squares: 0%; spheres: 20%; triangles: 40%; diagonals: 60%; stars: 80%; asterisk: 90%; octagon: 100%. The grey areas sketch the transition regime from rebound to partial pinning, which is the focus of this manuscript.

At low Re (pure glycerin) the drops pin on the surface for all investigated impact velocities. Understanding how energy is dissipated during impact if the drop pins on the surface is highly challenging, since the mechanism differs for sticky and (partially) rebounding drops. In the following we focus on the transition from rebound to partial pinning (dashed areas in Fig. 4).

Time dependent diameter. The contact diameter of the drop with the substrate $D(t)$ reflects the spreading and retraction dynamics and the energy dissipation of the impacting drop (Fig. 5). $D(t)$ first increases, passes a maximum at $t = t_{max}$, and then decreases again. The lateral expansion of the drop increases with increasing v_0. For high impact velocity the fit even works till a few ms after the onset of retraction. Spreading is always faster than retraction although the

evolution of the contact diameter is almost mirror-symmetric close to its maximum at high impact velocities (solid lines, Fig. 5). At larger times the temporal evolution of the contact diameter shows a pronounced dependence on impact velocity. The contact time, τ_0, increases with increasing v_0. Furthermore the retraction phase shows two well separated phases, a fast retraction phase followed by a much slower decrease of $D(t)$. The retraction dynamics change at $t \approx 8$ ms, equalizing the times where the diameter of the retracting drop matches the diameter of the drop before impact (Tab. 1).
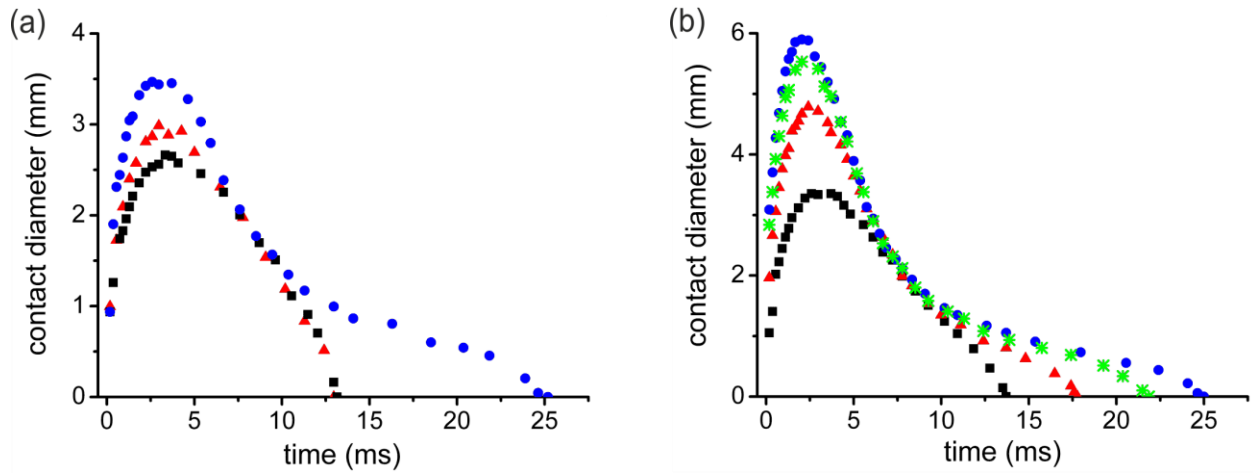

Figure 5. Temporal evolution of the contact diameter $D(t)$ upon spreading and retraction. a) Mixtures of ethanol-water, containing 50% ethanol. Impact velocities: ■ $v_0 = 0.4$ m/s; ▲ $v_0 = 0.5$ m/s; ● $v_0 = 0.8$ m/s; drop diameter: $D_0 = 2.0$ mm. b) Mixtures of glycerin-water containing 60 % glycerin. Impact velocities: ■ $v_0 = 0.6$ m/s; ▲ $v_0 = 1.3$ m/s; ✱ $v_0 = 1.7$ m/s; ● $v_0 = 2$ m/s; drop diameter: $D_0 = 2.4$ mm. Solid lines: parabolic fits.

To be able to better compare impact dynamics for drops with different interfacial tension and viscosity we plotted the scaled diameter $D(t)/D_{max}$ versus time at different impact velocities (Fig. 6a,b). For all liquid mixtures and impact velocities, $D(t)/D_{max}$ first increases, reaches a maximum at t_{max} and then decreases again (Video S1, S3). The ethanol rich drops rebound for $v_0 = 0.4$ m/s and $v_0 = 0.6$ m/s, whereas part of the drops pins on the coating at higher v_0. Noteably,

the temporal evolution of $D(t)/D_{max}$ depends on v_0. This is in contrast to drops impacting on flat hydrophobic surfaces, where $D(t)/D_{max}$ collapsed onto a single curve at different impact velocities.[45] This indicates that the mechanisms determining the retraction dynamics on hydrophobic and superamphiphobic surfaces differ. The different mechanism is also reflected in the dependence of $D(t)/D_{max}$ on varying the interfacial tension or viscosity. On flat surfaces the retraction dynamics depends on composition. [45] In contrast, on superamphiphobic coatings, the evolution of $D(t)/D_{max}$ is similar for ethanol-water and glycerin-water mixtures (Fig. 6c, 6d). At fixed impact velocity the evolution of the drop diameters $D(t)/D_{max}$ even collapse on a single curve for rebounding and partially rebounding drops for a variety of compositions. Again, at high impact velocity ($v_0 = 1.7$ m/s) the retraction phase shows two well separated phases, a fast retraction followed by a regime of much slower retraction.
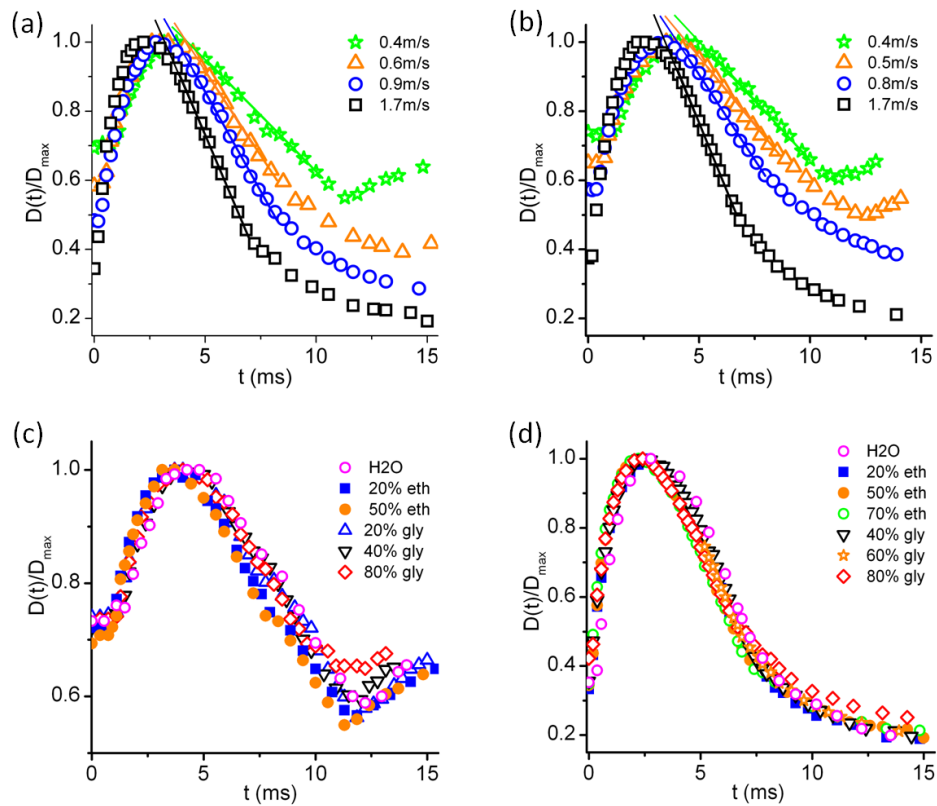

Figure 6. Temporal evolution of the contact diameter upon spreading and retraction normalized by the maximum spreading diameter. a) mixtures of ethanol-water containing 50 % ethanol, drop

diameter: D_0 = 2.0 mm; b) mixtures of glycerin-water containing 60 % glycerin, initial drop diameter: 2.4 mm; c) Variation of the composition while keeping the impact velocity constant, v_0 = 0.4 m/s. d) Variation of the composition while keeping the impact velocity constant, v_0 = 1.7 m/s. a) and b) The solid lines give the maximum retraction rate.

A possible reason for the different retraction dynamics on flat surfaces compared to superamphiphobic coatings may be that a drop can partially impale a superamphiphobic coating. Figs. 5 and 6 support the following scenario (Fig. 7). At low impact velocities or low *We*, the drop hardly impales the coating whereas with increasing v_0 the depth of impalement increases (Fig. 7a). We expect that partial impalement is restricted to the area just underneath the initial impact zone of the drop, since the retraction dynamics changes when the diameter of the retracting drop matches the diameter of the drop before impact. With increasing impact velocity the liquid impales deeper in the coating and more energy is required to pull the drop out (Fig. 7b).

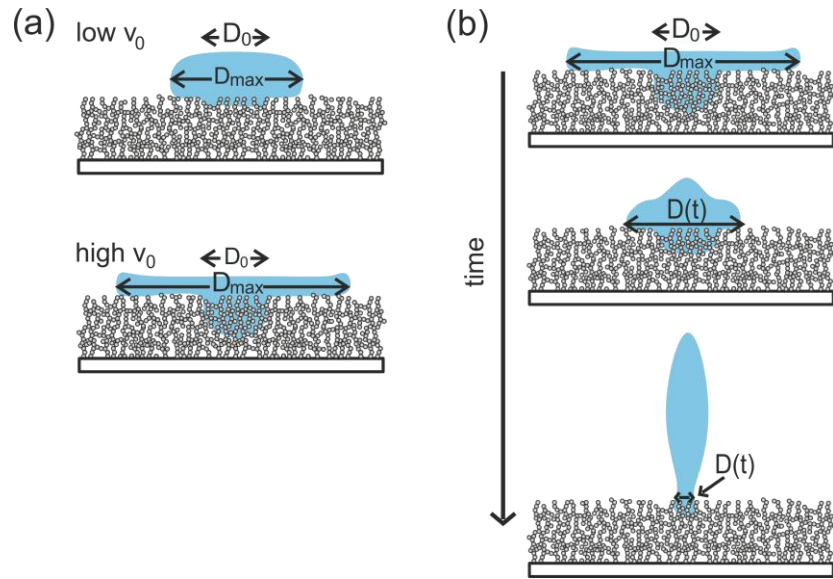**Figure 7.** Sketch of the drop close to maximum spreading. (a) At low impact velocity the drop hardly impales the coating. The depth of impalement increases with impact velocity. (b) Sketch of the evolution of a retracting drop.

Maximum spreading diameter. If this hypothesis is correct, for low viscous liquids the maximum spreading diameter should follow the $We^{1/4}$ law,[38] and the fast retraction rate should be

determined by capillarity and inertia.[38, 45] Furthermore, the contact time and the restitution coefficient should increase with v_0. For low viscous mixtures the normalized maximum spreading diameter correlates well with $We^{1/4}$, and thus with $v_0^{0.5}$, i.e. viscous dissipation of the moving contact line is negligible (Fig. 8). This $We^{1/4}$ scaling even holds for mixtures containing 70% of ethanol, $\gamma = 26$ mN/m, i.e. for mixtures that wet the surface, hinting that wetting does not affect the spreading dynamics (Fig. 8a). This implies that spreading is determined by capillarity and inertia, independent of whether a drop rebounds or pins on the surface.

With increasing glycerin concentration viscous dissipation influences the spreading dynamics (Fig. 8b). However, up to 60% glycerin the influence of viscosity on the spreading dynamics is small. At high glycerin content ($\geq$ 80% glycerin) the $We^{1/4}$ scaling breaks down.
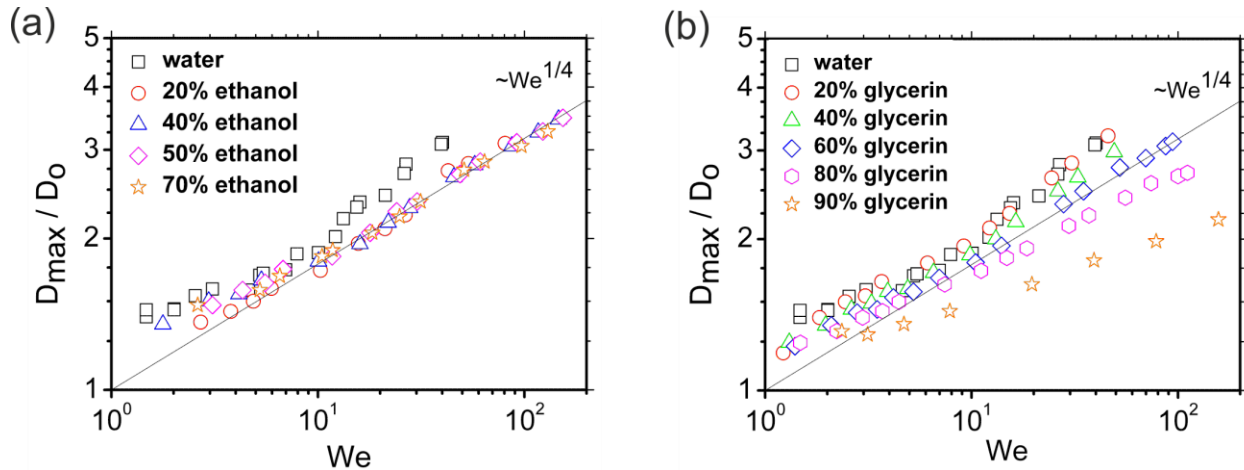
Figure 8. Maximum diameter D_{max} of a spreading drop normalized by the diameter of the drop before impact as a function of the Weber number for ethanol-water mixtures (a). The solid line has a slope of 0.25. (b) Glycerin-water mixture as a function of the Reynolds number. The solid lines are guides to the eye, with slopes decreasing from 0.25 to 0.125.

Retraction rate. We investigated the influence of impact velocity, interfacial tension, and viscosity on the maximum retraction rate $\dot{\varepsilon}$ (solid lines in Fig. 6a, 6b). For both systems $\dot{\varepsilon}$ increases with impact velocity and thus with We (Fig. 9). Bartolo et al. report that on a flat surface $\dot{\varepsilon}$ did not depend on We but varied with composition.[45] However, the authors focused on

higher *We,* where the flattened drop can be described by a thin film. When plotting the dimensionless retraction rate $\dot{\varepsilon}\tau_0$ versus the Ohnesorge number *Oh*, it remains almost constant for all compositions investigated (inset Fig. 9). The independence of $\dot{\varepsilon}\tau_0$ on the Ohnesorge number implies that in the first phase the retraction rate is dominated by capillarity and inertia and less by viscosity.
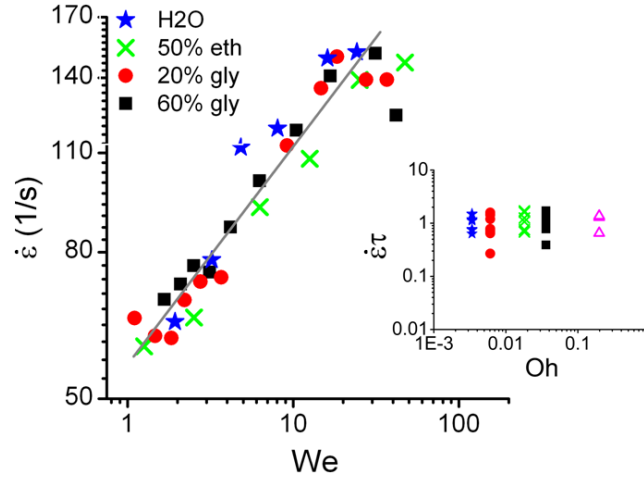

Figure 9. a) Retraction rate $\dot{\varepsilon}$ versus Weber number for drops of different ethanol-water and glycerin-water mixtures. The solid line serves as a guide to the eye. b) Dimensionless retraction rate $\dot{\varepsilon}\tau_0$ versus the Ohnesorge number, *Oh*. Inset: Impact velocity: $v_0 = 0.4$ m/s (lowest data points) $v_0 = 2.0$ m/s (topmost data points).

Contact time. To quantify the interaction of the drop with the surface we measured the contact time τ_0 of drops in dependence on composition and impact velocity. At low impact velocity, $v_0 = 0.35$ m/s, the contact time was constant and did not depend on the composition; the only exceptions were for the highest ethanol (Fig. 10a) and glycerol concentrations (Fig. 10b). The contact time agreed with the longest Rayleigh period $\tau_0 \approx \sqrt{\rho\pi^2 R^3/2\gamma}$. The calculated values are close to the extrapolation of the experimental ones at low impact velocity. This result is in agreement with previous observations on hydrophobic and superhydrophobic surfaces and indicates that impact at low velocities is dominated by capillarity and inertia.[38, 56]

	water	20%eth	40%eth	50%eth	70%eth	20%gl	40%gl	60%gl	80%gl	90%gl

τ_0 [ms]	10.8	12.8	12.2	12.4	11.0	11.5	11.9	12.3	12.7	12.6

Table 2. Calculated contact times

Contact times increase with impact velocity (Fig. 10c,d). Despite the longer contact times the drops rebound, i.e. no sign of pinning is visible by eye. High contact times with the substrate are strongly correlated with an elongation of the drop just before rebound (Fig. 3, Video S2, S3). The advancing Θ_a and receding Θ_r contact angle change during spreading and retraction. Θ_r closely approaches Θ_a in the first phase of retraction supporting weak adhesion, since adhesion depends on the difference between the advancing and receding contact angle. [33, 45, 48]
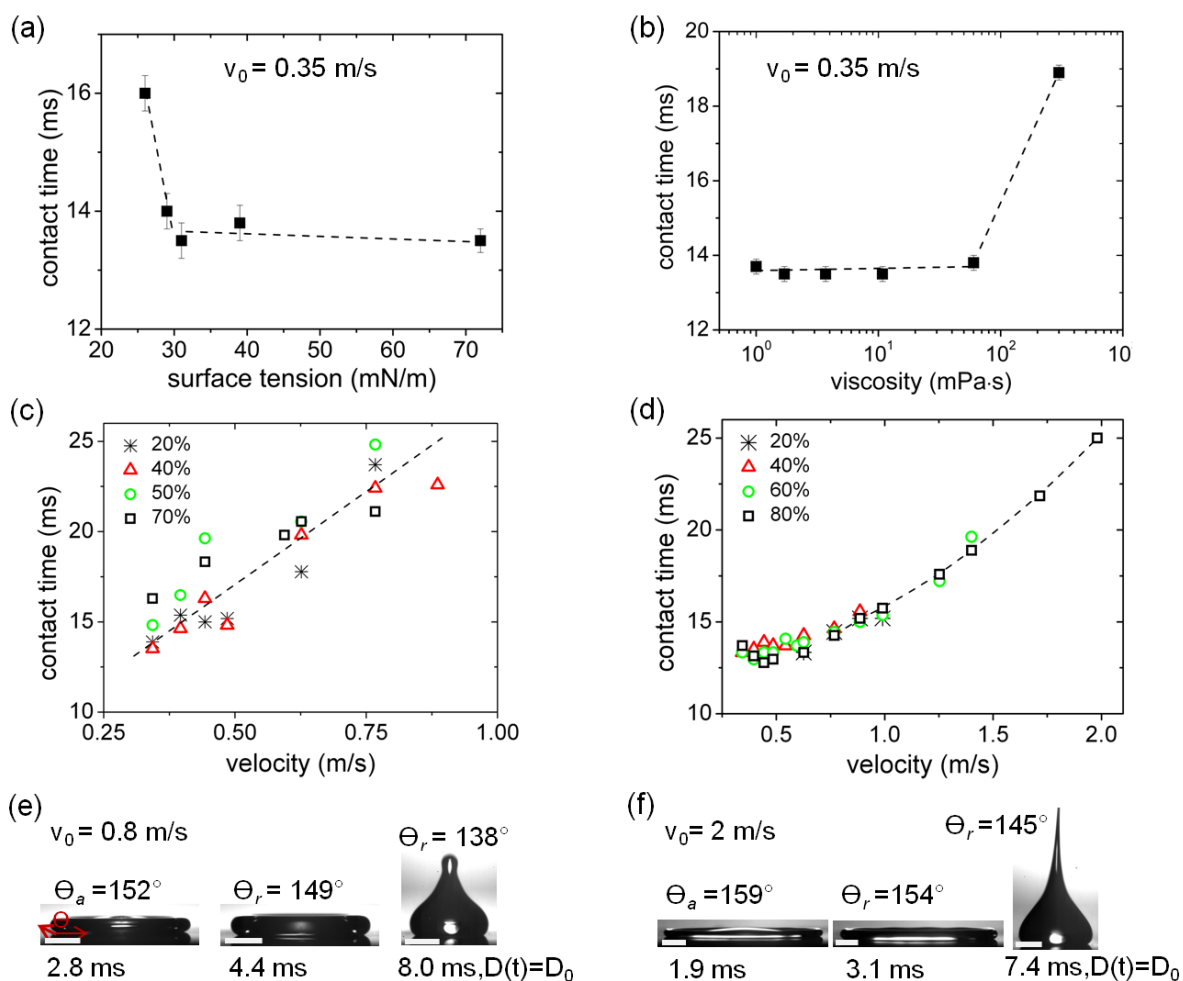
Figure 10. Dependence of the contact time τ of bouncing drops on velocity for different compositions. a) Mixtures of ethanol-water varying the ethanol concentration at $v_0 = 0.35$ m/s. b) Mixtures of glycerin-water varying the glycerin concentration at $v_0 = 0.35$ m/s. c) Dependence of the contact time on velocity for mixtures of ethanol-water. d) Dependence of the contact time on velocity for mixtures of glycerin-water. Only contact times for rebounding drops are evaluated where no hint of pinning was observed. Pictures of ethanol-rich e) and glycerin-rich f) drops. The advancing $\Theta_a(t)$ and receding $\Theta_r(t)$ contact angles just before and after the drop reaches its maximum spreading diameter and at $D=D_{max}$ are added. The dashed lines serve as a guide to the eye.

Restitution coefficient. The impalement of a drop into the coating is reflected in the restitution coefficient, because of viscous dissipation inside the porous coating. The restitution coefficient C_R for pure water was $C_R \approx 0.8$ at an impact velocity of $v_0 = 0.35$ m/s (Fig. 11a). Decreasing γ decreases the critical pressure for depinning impalement (Eq. 1). As long as $\gamma > 30$ mN/m wetting is prevented and C_R decreases only by 15%. However, C_R strongly decreases for $\gamma \leq 30$ mN/m. C_R also decreases with increasing viscosity (Fig. 11 b). Again the dependence is most pronounced at high viscosities, i.e. close to the transition regime between rebound and partial pinning. Increasing impact velocity increases the dynamic wetting pressure P_D whereas P_{dep} remains unchanged. This decreases the energy barrier against impact. Likely this causes deeper impalement of the drop into the coating. Thus more energy is dissipated while pulling the drop out of the coating, i.e. C_R decreases (Fig. 11c). The restitution coefficient differs between subsequent rebounds of the same drop (Fig. 11d), where we determined C_R with respect to the previous rebound. At $v_0 = 0.5$ m/s, the restitution coefficient takes a value of CR $= 0.65$ for the first impact (60% glycerin-water). Subsequent impacts rebound with CR ≈ 0.95 at the same part of the surface. SEM images taken after drop impact did not reveal changes of the surface morphology. However, it might be that a partially impaled drop breaks a few silica necks while retracting. Due to the coating's self-similarity this would not alter the structure nor the fractal dimension. However, it maight be a source of energy dissipation.
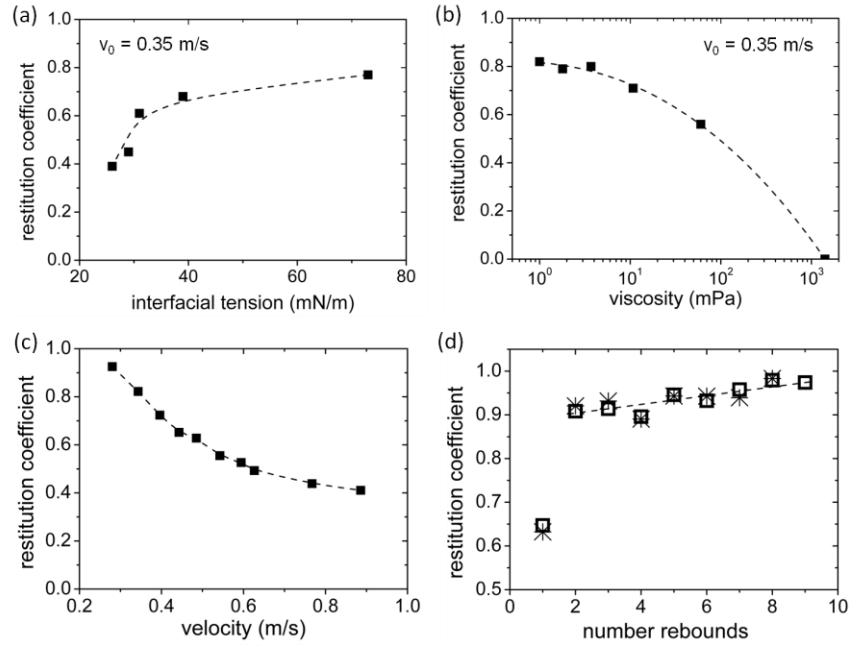
Figure 11. The restitution coefficient C_R of liquids impacting on a superamphiphobic surface as a function of (a) surface tension and (b) viscosity. Impact velocity: $v_0 = 0.35$ m/s. c) Dependence of the restitution coefficient for mixtures of 60% glycerin-water on impact velocity. d) Dependence of the restitution coefficient for mixtures of glycerin-water on the number of rebounds. Squares: 20% glycerin, stars: 40% glycerin, impact velocity: $v_0 = 0.35$ m/s.

Discussion. Due to the inherent inhomogeneity of the structure the local impalement pressure varies (Fig. 2). The decrease of the restitution coefficient with increasing velocity supports that the depth of impalement increases with We. So far it is unclear how deep a drop impales into the coating. The lower surface tension of ethanol rich drops favors partial impalement. Therefore, ethanol-rich drops pin at lower impact velocities on the surface compared to glycerin-rich drops, in agreement with our results. Local impalement of the drop underneath the initial contact zone is supported by the cross-over of the fast ($t < 7$ ms) to the slow decrease ($t > 8$ ms) of the contact diameter during retraction. The beginning of the slow phase correlates to the initial drop diameter. The two retraction regimes are also reflected in the contact angles. During the first phase of retraction the receding contact angle is close to the advancing (Figs. 10e, 10f), i.e. adhesion is small. The receding contact angle increases strongly in the second phase, reflecting strong adhesion of the drop on the coating. This supports that impalement is limited to the area underneath the initial contact zone (Video 1, and Video 3). It might be that a partially impaled

drop breaks a few silica necks while retracting. Due to the coating's self-similarity this would not alter the structure nor the fractal dimension. However, it maight be a source of energy dissipation.

Recently, it has been argued that pinning might be caused by the so called effective liquid Hammer pressure. In the very first stage after a drop hits the surface, the compressed liquid creates a shock wave that adds a vertical component to the velocity of the fluid. The shock wave relaxes as soon as it overtakes the moving contact line. The effective Hammer pressure is given by $P_{EWH} = \delta \rho C_S v_0$, where $C_S = 1500$ m/s is the sound velocity in water. Depending on details of the impact the prefactor δ varies between 0.2 and 2.5 for flat surfaces.[57-58] To the best of our knowledge, for superhydrophobic surfaces δ is experimentally not directly accessible. Values varying between $\delta = 0.2$ and $\delta = 0.001$ have been postulated,[49, 51, 59] resulting in $P_{EWH} = 1.5 -$ 300 kPa for an impact velocity of $v_0 = 1$ m/s. Although P_{EWH} may exceed P_{sag} and P_D, the short duration of the shock wave makes it unlikely that impalement is dominated by the Hammer pressure. On a flat surface compressibility effects are relevant until the radius x_0 of the contact periphery reaches $x_0 \approx D_0 v_0/2C_S$.[57] The duration t_s of this compression lasts until the release wave passed through the compressed liquid, $t_s \approx x_0 / C_S = v_0 D_0 / 2 C_S^2 \approx 1$ ns for a 2 mm sized drop impacting the surface with a velocity of $v_0 = 2$ m/s.[57, 60] Even at the highest impact velocity ($v_0 = 2.4$ m/s) the drop would impale the structure only by less than 2.4 nm until the shock wave relaxed. Therefore, we expect that impalement is determined by depinning.

Summary. After impacting on a superamphiphobic coating, drops of ethanol-water and glycerin-water rebound, partially or fully pin, or splash, depending on their velocity and viscosity. At low velocity the drops completely rebound. The temporal evolution of the drop diameter during spreading is determined by capillarity and inertia. The retraction dynamics shows two well-separated regimes, a fast and a slow one. In the fast regime, energy stored in the deformation of the surface is transformed back into kinetic energy. This phase is inertia dominated, even up to 80% glycerin. The existence of a slow phase supports our hypothesis that the drop impales the coating only underneath its initial impact zone. With increasing impact velocity the liquid impales the coating deeper. Less energy can be converted back to kinetic energy; it is required to pull the drop out of the coating. This is reflected in the decrease of the restitution coefficient with

impact velocity. We argue that partial pinning starts when the wetting pressure $\rho v_0^2/2$ of the drop leads to an impalement depth that exceeds a viscosity and interfacial tension dependent critical value. Impalement is dominated by depinning rather than sagging. Depinning is also most likely the impalement mechanism for drop impact experiments on superhydrophobic surfaces, too.

Acknowledgements

References

(1) Yarin, A. L., Drop impact dynamics: Splashing, spreading, receding, bouncing. *Annu Rev Fluid Mech*. **2006**, *38*, 159-192.

(2) Marengo, M.; Antonini, C.; Roisman, I. V.; Tropea, C., Drop collisions with simple and complex surfaces. *Curr. Opin. Colloid Interface Sci.* **2011,** *4*, 292-302.

(3) Bartolo, D.; Josserand, C.; Bonn, D., Singular jets and bubbles in drop impact. *Phys Rev Lett.* **2006,** *96*, 124501.

(4) Reyssat, M.; Pepin, A.; Marty, F.; Chen, Y.; Quere, D., Bouncing transitions on microtextured materials. *Europhys Lett.* **2006,** *74*, 306-312.

(5) Rioboo, R.; Marengo, M.; Tropea, C., Time evolution of liquid drop impact onto solid, dry surfaces. *Exp Fluids.* **2002,** *33*, 112-124.

(6) Chandra, S.; Avedisian, C. T., On the Collision of a Droplet with a Solid Surface. *P Roy Soc Lond A Mat.* **1991,** *432*, 13-41.

(7) Rein, M., Phenomena of liquid drop impact on solid and liquid surfaces. *Fluid Dyn Res.* **1993,** *12*, 61-93.

(8) Hoefnagels, H. F.; Wu, D.; de With, G.; Ming, W., Biomimetic superhydrophobic and highly oleophobic cotton textiles. *Langmuir.* **2007,** *23*, 13158-13163.

(9) Feng, X.; Jiang, L., Design and creation of superwetting/antiwetting surfaces. *Adv Mater.* **2006,** *18*, 3063-3078.

(10) Bravo, J.; Zhai, L.; Wu, Z. Z.; Cohen, R. E.; Rubner, M. F., Transparent superhydrophobic films based on silica nanoparticles. *Langmuir.* **2007,** *23*, 7293-7298.

(11) Deng, X.; Mammen, L.; Zhao, Y.; Lellig, P.; Muellen, K.; Li, C.; Butt, H.-J.; Vollmer, D., Transparent, Thermally Stable and Mechanically Robust Superhydrophobic Surfaces Made from Porous Silica Capsules. *Adv Mater.* **2011,** *23*, 2962-2965.

(12) Nguyen, T. P. N.; Brunet, P.; Coffinier, Y.; Boukherroub, R., Quantitative Testing of Robustness on Superomniphobic Surfaces by Drop Impact. *Langmuir.* **2010,** *26*, 18369-18373.

(13) Barthlott, W.; Neinhuis, C., Purity of the sacred lotus, or escape from contamination in biological surfaces. *Planta.* **1997,** *202*, 1-8.

(14) Quere, D., Non-sticking drops. *Rep. Prog. Phys.* **2005,** *68*, 2495-2532.

(15) Gao, L. C.; McCarthy, T. J., The "lotus effect" explained: Two reasons why two length scales of topography are important. *Langmuir.* **2006,** *22*, 2966-2967.

(16) Feng, L.; Li, S. H.; Li, Y. S.; Li, H. J.; Zhang, L. J.; Zhai, J.; Song, Y. L.; Liu, B. Q.; Jiang, L.; Zhu, D. B., Super-hydrophobic surfaces: From natural to artificial. *Adv Mater.* **2002,** *14*, 1857-1860.

(17) Extrand, C. W., Model for contact angles and hysteresis on rough and ultraphobic surfaces. *Langmuir.* **2002,** *18*, 7991-7999.

(18) Li, X.-M.; Reinhoudt, D.; Crego-Calama, M., What do we need for a superhydrophobic surface? A review on the recent progress in the preparation of superhydrophobic surfaces. *Chem. Soc. Rev.* **2007,** *36*, 1350-1368.

(19) Bormashenko, E.; Pogreb, R.; Whyman, G.; Erlich, M., Cassie-wenzel wetting transition in vibrating drops deposited on rough surfaces: Is the dynamic cassie-wenzel wetting transition a 2D or 1D affair? *Langmuir.* **2007,** *23*, 6501-6503.

(20) Cassie, A. B. D.; Baxter, S., Wettability of porous surfaces. *Trans. Faraday Soc.* **1944,** *40*, 0546-0550.

(21) Wenzel, R. N., Resistance of solid surfaces to wetting by water. *Ind. Eng. Chem.* **1936,** *28*, 988-994.

(22) Jung, Y. C.; Bhushan, B., Dynamic Effects Induced Transition of Droplets on Biomimetic Superhydrophobic Surfaces. *Langmuir.* **2009,** *25*, 9208-9218.

(23) Tuteja, A.; Choi, W.; Ma, M. L.; Mabry, J. M.; Mazzella, S. A.; Rutledge, G. C.; McKinley, G. H.; Cohen, R. E., Designing superoleophobic surfaces. *Science.* **2007,** *318*, 1618-1622.

(24) Chen, W.; Fadeev, A. Y.; Hsieh, M. C.; Oner, D.; Youngblood, J.; McCarthy, T. J., Ultrahydrophobic and ultralyophobic surfaces: Some comments and examples. *Langmuir.* **1999,** *15*, 3395-3399.

(25) Young, T., An essay on the cohesion of fluids. *Philos. Trans. R. Soc. London.* **1805,** *95*, 65-87.

(26) Butt, H. J.; Graf, K. H.; Kappl, M., *Physics and chemistry of interfaces*. Wiley-VCH: Weinheim, **2006**; p 386

(27) Herminghaus, S., Roughness-induced non-wetting. *Europhys. Lett.* **2007,** *52*, 165-170.

(28) Deng, X.; Mammen, L.; Butt, H.-J.; Vollmer, D., Candle soot as a template for a transparent robust superamphiphobic coating. *Science.* **2012,** *335*, 67-70.

(29) Butt, H.-J.; Semprebon, C.; Papadopoulos, P.; Vollmer, D.; Brinkmann, M.; Ciccotti, M., Design principles for superamphiphobic surfaces. *Soft Matter.* **2013,** *9*, 418-428.

(30) Bartolo, D.; Bouamrirene, F.; Verneuil, E.; Buguin, A.; Silberzan, P.; Moulinet, S., Bouncing or sticky droplets: Impalement transitions on superhydrophobic micropatterned surfaces. *Europhys. Lett.* **2006,** *74*, 299-305.

(31) Tsai, P.; van der Veen, R. C. A.; van de Raa, M.; Lohse, D., How Micropatterns and Air Pressure Affect Splashing on Surfaces. *Langmuir.* **2010,** *26*, 16090-16095.

(32) Kwak, G.; Lee, M.; Senthil, K.; Yong, K., Impact dynamics of water droplets on chemically modified WOx nanowire arrays. *Appl Phys Lett.* **2009,** *95*, 153101.

(33) Rioboo, R.; Voue, M.; Vaillant, A.; De Coninck, J., Drop Impact on Porous Superhydrophobic Polymer Surfaces. *Langmuir.* **2008,** *24*, 14074-14077.

(34) Duvivier, D.; Rioboo, R.; Voue, M.; De Coninck, J., Drop impact on superhydrophobic surfaces : varying gravitational effects. *Atomization Spray.* **2012,** *22*, 409-429.

(35) Jung, Y. C.; Bhushan, B., Dynamic effects of bouncing water droplets on superhydrophobic surfaces. *Langmuir.* **2008,** *24*, 6262-6269.

(36) Patankar, N. A., Consolidation of Hydrophobic Transition Criteria by Using an Approximate Energy Minimization Approach. *Langmuir.* **2010,** *26*, 8941-8945.

(37) Pan, S.; Kota, A. K.; Mabry, J. M.; Tuteja, A., Superomniphobic Surfaces for Effective Chemical Shielding. *J. Am. Chem. Soc.* **2013,** *135*, 578-581.

(38) Clanet, C.; Beguin, C.; Richard, D.; Quere, D., Maximal deformation of an impacting drop. *J Fluid Mech.* **2004,** *517*, 199-208.

(39) Richard, D.; Clanet, C.; Quere, D., Surface phenomena - Contact time of a bouncing drop. *Nature.* **2002,** *417*, 811.

(40) Tsai, P.; Pacheco, S.; Pirat, C.; Lefferts, L.; Lohse, D., Drop Impact upon Micro- and Nanostructured Superhydrophobic Surfaces. *Langmuir.* **2009,** *25*, 12293-12298.

(41) Wang, Z.; Lopez, C.; Hirsa, A.; Koratkar, N., Impact dynamics and rebound of water droplets on superhydrophobic carbon nanotube arrays. *Appl Phys Lett.* **2007,** *91*, 023105.

(42) Okumura, K.; Chevy, F.; Richard, D.; Quere, D.; Clanet, C., Water spring: A model for bouncing drops. *Europhys. Lett.* **2003,** *62*, 237-243.

(43) Rayleigh, L., On the capillary phenomena of jets. *Proc. Roy. Soc. London* **1879,** *29*, 71-97.

(44) Biance, A. L.; Chevy, F.; Clanet, C.; Lagubeau, G.; Quere, D., On the elasticity of an inertial liquid shock. *J Fluid Mech.* **2006,** *554*, 47-66.

(45) Bartolo, D.; Josserand, C.; Bonn, D., Retraction dynamics of aqueous drops upon impact on non-wetting surfaces. *J Fluid Mech.* **2005,** *545*, 329-338.

(46) Schroll, R. D.; Josserand, C.; Zaleski, S.; Zhang, W. W., Impact of a Viscous Liquid Drop. *Phys Rev Lett.* **2010,** *104*, 034504.

(47) Reyssat, M.; Yeomans, J. M.; Quere, D., Impalement of fakir drops. *Europhys. Lett.* **2008,** *81*, 26006.

(48) Papadopoulos, P.; Mammen, L.; Deng, X.; Vollmer, D.; Butt, H. J., How superhydrophobicity breaks down. *P Natl Acad Sci USA.* **2013,** *110*, 3254–3258.

(49) Deng, T.; Varanasi, K. K.; Hsu, M.; Bhate, N.; Keimel, C.; Stein, J.; Blohm, M., Nonwetting of impinging droplets on textured surfaces. *Appl Phys Lett.* **2009,** *94*, 133109.

(50) Rothstein, J. P., Slip on Superhydrophobic Surfaces. *Annu Rev Fluid Mech.* **2010,** *42*, 89-109.

(51) Kwon, D. H.; Lee, S. J., Impact and wetting behaviors of impinging microdroplets on superhydrophobic textured surfaces. *Appl Phys Lett.* **2012,** *100*, 171601.

(52) Extrand, C. W., Designing for optimum liquid repellency. *Langmuir.* **2006,** *22*, 1711-1714.

(53) Vazquez, G.; Alvarez, E.; Navaza, J. M., Surface Tension of Alcohol Water + Water from 20 to 50 .degree.C. *J Chem Eng Data.* **1995,** *40*, 611-614.

(54) Perry, R. H.; Green, D. W., Perry's Chemical Engineers' Handbook (7th Edition). In McGraw-Hill: **1997**; pp 3-89.

(55) Romero, C. M.; Paéz, M. S., Surface tension of aqueous solutions of alcohol and polyols at 298.15 K. *Phys Chem Liq.* **2006,** *44*, 61-65.

(56) Chen, L.; Li, Z., Bouncing droplets on nonsuperhydrophobic surfaces. *Phys Rev E.* **2010,** *82*, 016308.

(57) Bowden, F. P.; Field, J. E., The Brittle Fracture of Solids by Liquid Impact, by Solid Impact, and by Shock. *P Roy Soc Lond A Mat.* **1964,** *282*, 331-352.

(58) Lesser, M. B.; Field, J. E., THE IMPACT OF COMPRESSIBLE LIQUIDS. *Annu Rev Fluid Mech.* **1983,** *15*, 97-122.

(59) Kwon, H.-M.; Paxson, A. T.; Varanasi, K. K.; Patankar, N. A., Rapid Deceleration-Driven Wetting Transition during Pendant Drop Deposition on Superhydrophobic Surfaces. *Phys Rev Lett.* **2011,** *106*, 036102.

(60) Mongruel, A.; Daru, V.; Feuillebois, F.; Tabakova, S., Early post-impact time dynamics of viscous drops onto a solid dry surface. *Phys Fluids.* **2009,** *21*, 032101.

Chapter 5: Towards green chemistry: Solvent-free synthesis of microparticles on superamphiphobic surfaces

Xu Deng, Maxime Paven, Periklis Papadopoulos, Ming Ye, Si Wu, Thomas Schuster, Markus Klapper, Doris Vollmer*, Hans-Jürgen Butt*

Affiliations:

Max Planck Institute for Polymer Research, Ackermannweg 10, D-55128, Mainz, Germany

*Correspondence to: butt@mpip-mainz.mpg.de, vollmerd@mpip-mainz.mpg.de

Polymer particles constitute a large part of all synthetic materials, with applications ranging from drug delivery and diagnosis to paints and coatings. So far, most particle synthesis requires solvents or a continuous immiscible liquid phase, and surfactants. Here we show that superamphiphobic layers can be used to produce polymeric and composite microspheres without solvents, process liquids, or additives. We take advantage of the repellency of superamphiphobic layers to monomers and polymer melts and the extremely low adhesion to particles. Polymers can be directly synthesized on superamphiphobic layers, as demonstrated for a radical polymerization. Janus and magnetic microspheres are produced by melting agglomerates of powder. Synthesizing microparticles in an efficient and environmentally-friendly way is a significant step towards green chemistry.

Synthetic polymer particles are omnipresent in our daily life. Multicomponent polymer-based microspheres find applications in drug delivery[1-2], protein isolation and analysis[3], photonics[4-5], and displays[6-8]. Depending on the function, different materials, sizes and architectures are required; architectures include microgels[2], core-shell, patchy, multicompartment, and Janus particles[7,9-13]. It is a common practice that microparticles are produced in solution or that drops of the primary, reacting liquid are confined in a second, immiscible liquid, stabilized by surfactants or high molecular amphiphiles (e.g. emulsion polymerization)[14]. Several novel methods have been developed to produce even multicomponent, functional microparticles[9,11,13,15], e.g. by microfluidic photo[5,10,16-18] or thermal polymerization[7].

Superhydrophobic surfaces have been used to produce particles by evaporation of water from a dispersion[19-20] or solution[1]. These methods rely on solvents or processing liquids and often involve the use of surfactants. For environmental and health reasons and to reduce energy consumption it is mandatory to reduce or completely avoid using any type of solvent or, to go a step further, also to avoid surfactant.
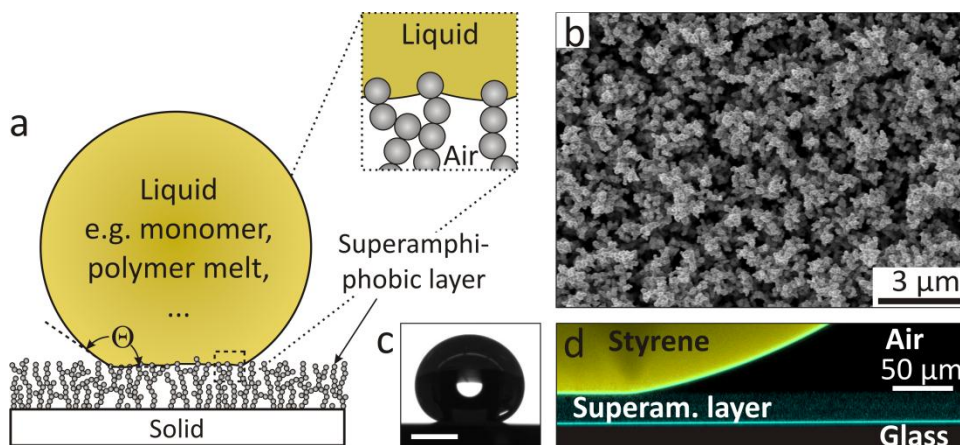

Figure 1| Liquid drop on a superamphiphobic layer. a, Schematic of a liquid drop on a superamphiphobic layer and a magnified view of the interface between the liquid and the superamphiphobic layer. **b**, Scanning electron microscope (SEM) image of a superamphiphobic layer. **c**, Video image and **d** vertical section through a drop of styrene on a superamphiphobic layer imaged with a confocal microscope. Scale bar in **c** is 1 mm. The 6 µL drop was labeled with 0.04 mg/mL N-(2,6-diisopropylphenyl)perylene-3,4-dicarbonacidimide.

Here, we describe a novel method to synthesize one- or multicomponent, functional micro-particles. Our method requires neither solvent nor surfactants but makes use of the low adhesion of monomers, polymer solutions and melts with the superamphiphobic layer (Fig. 1). Polymeric microspheres are synthesized by radical polymerization from methacrylate derivatives. To show the generality of the presented approach we fabricated magnetic and Janus particles starting from a polymer powder. The extremely low adhesion allows removing the microparticles easily after solidification.

Superamphiphobicity extends the properties of superhydrophobicity towards organic liquids and aqueous solutions of surfactants or proteins[21-26]. On superamphiphobic layers even non-polar liquids form an apparent contact angle above 150 ° and a roll-off angle below 10 ° (Fig. 1a). For superhydro- and -amphiphobicity surface roughness and low interfacial energy are essential. Microscopic pockets of air are trapped beneath the liquid. Entrapped air leads to an increase of the apparent contact angle Θ, reduces contact angle hysteresis, and leads to the low roll-off angle. However, for superamphiphobicity roughness and low interfacial energy are not sufficient. Protrusions with overhanging geometries are required as an additional element to stabilize the drop[24,27-28]. Otherwise, drops, initially resting on air pockets and protrusions, pass the transition to complete wetting, i.e. the droplet impales the layer. Since the drop rests on top of the protrusions the real solid/liquid interfacial area is much smaller than the apparent contact area [28]. This minimizes adhesion of the drop on the surface.

We recently developed a simple method to fabricate optically transparent, robust superamphi-phobic layers (Fig. 1)[29]. Our design is based on a fractal-like arrangement of nanoparticles. A template of soot particles (30-50 nm diameter) is coated with a 20-30 nm thick layer of SiO_2 (Fig. 1b). To render the layer transparent the soot is burned away at 600 °C. Finally, the porous SiO_2 layer is coated with a semifluorinated alkylsilane (trichloro(1H,1H,2H,2H-perfluorooctyl) to lower the surface energy (Fig. 1c,d). The layer is UV resistant, stable up to 350 °C, optically transparent, and does not swell in organic or polar liquids. This opens up the opportunity to fabricate almost contact-free solid-liquid interfaces. Even drops of monomers form contact angles above 150 ° and low roll-off angles (table 1).

Monomer	Θ	α	γ (mN/m)
Styrene	158°	6°	34
Methyl methacrylate	156°	10°	28
Acrylic acid	154°	7°	29
Adipoyl chloride	152°	9°	38
Ethylenediamine	152°	16°	42

Table 1| Contact angle Θ, roll-off angle α, and surface tension γ of some monomers on a superamphiphobic surfaces at 20°C.

A drop of monomer and initiator can be directly polymerized by UV irradiation or by heating on a superamphiphobic layer. As an example we carried out a radical polymerization of two methacrylates with an UV initiator. After mixing bisphenol A glycerolate dimetacrylate (bis-GMA) and triethylene glycol dimethacrylate (TEGDMA) with the photoinitiator phenylbis(2,4,6-trimethylbenzoyl)phosphine oxide, a drop was placed with a pipette on a superamphiphobically coated slightly concave watch glass (Fig. 2a). The mixture showed an advancing contact angle of 159 ° and a roll-off angle of 20 °. The polymerization was initiated by UV irradiation. To avoid deformation due to gravity or adhesion, the watch glass was moved by a 2D orbital shaker to keep the drop in rolling motion while its viscosity continuously increased. The size of the spherical particles corresponds to the initial volume of the monomer drop and can be as large as a few millimeters (Fig. 2b,c).
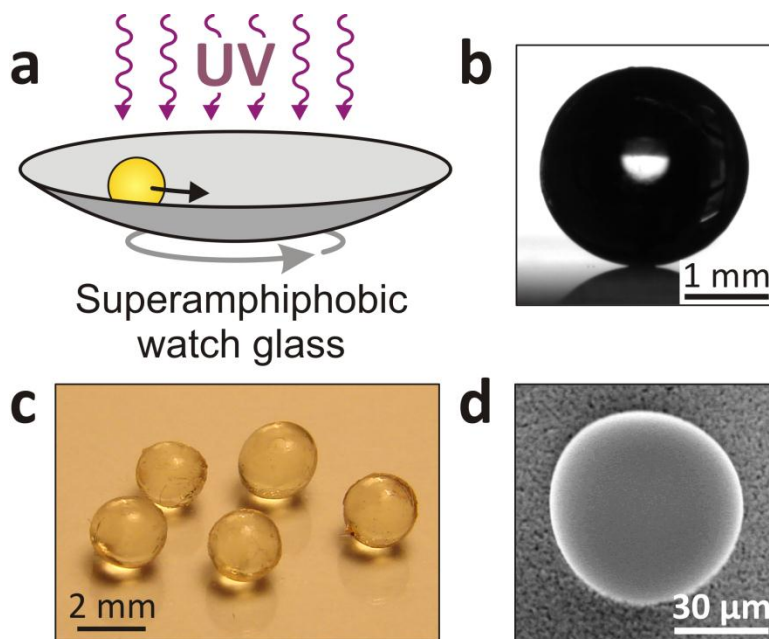

Figure 2| Synthesis of microspheres by radical polymerization. a, Schematic of the set-up. **b** and **c** Particles synthesized from 15 wt% Bis-GMA, 84 wt% TEGDMA, 1 wt% photoinitiator. After mixing and sonication for 30 min a drop of 8-10 μL was pipetted into a concave watch glass (10 cm diameter, 1.5 cm high) coated with a superamphiphobic layer. The polymerization

was initiated by pulsed UV irradiation for 1 min followed by 4 min continuous illumination (LQ 400, UV-A: 200 mW/cm^2 at the end of the glass fiber). **d**, SEM image of a microsphere from 99 wt% TEGDMA with 1 wt% photoinitiator polymerized by 3 min UV exposure. The mixture was deposited by an inkjet printer (Nano-Tip J A 070-401) held at a distance of 4 cm.

Particle diameters as small as few 10 µm are obtained when the monomer mixture is deposited using an inkjet (Fig. 2d). Such small particles might also be obtained by spray coating. The minimal size of the microsphere needs to exceed the spacing between neighboring protrusions to prevent drops from sinking into the superamphiphobic layer. For our layers this spacing is about 1 µm. Another limit is the impact velocity. When the impact velocity of the drop exceeds a certain critical value it impales the superamphiphobic layer and super-repellency is lost.

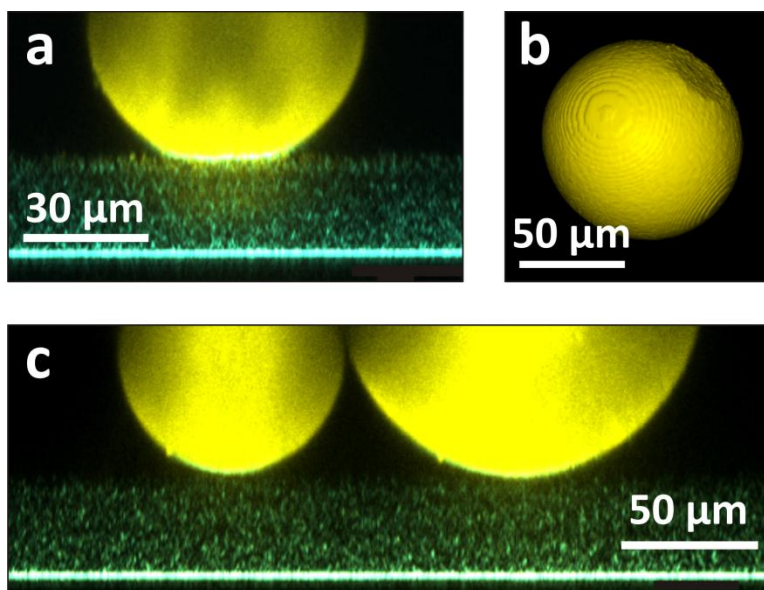**Figure 3| Confocal images of polystyrene particles formed on a superamphiphobic layer after heating the powder to 100°C. a**, Vertical cross-section. **b**, Particle showing the previous contact area on the top right side. **c**, Two polystyrene particles without a flat area. Polystyrene was labeled with rhodamine B (M_W= 13.8 kg/mol, T_g=91 °C, Synthesis described in supplementary information).

The monomer drops have an extremely small contact area with the superamphiphobic layer. In confocal microscope images it shows up as a planar area (Fig. 1d). In some cases this planar area shows up also in polymer particles, which had been molten on a superamphiphobic layer (Fig. 3a,b). In other cases the annealed polymer particles looked perfectly spherical (Fig. 3c), presumably the particles somehow shifted or moved during cooling. To avoid a planar region the drops need to be kept in motion while the particles solidify.

Since the superamphiphobic layers remain stable up to 350 °C microspheres can also be produced by heating a thermoplastic polymer powder or blend above its glass transition temperature, T_g (Fig. 4a). As an example we fabricated polystyrene microspheres (Supplementary Movie. S1 and Fig. S5) and magnetic hybrid microspheres. Microparticles with a permanent magnetic dipole moment are useful as micro-rheological probes, magnetic micro mixers[17-18] and they are used in various biomedical applications, e.g. as immunoassays and for protein analysis[3,17]. Polystyrene was mixed with iron oxide nanoparticles (See supplementary information, supplementary Fig. S1) and deposited on a superamphiphobic layer (Fig. 4b). When heating to 165 °C, the powder agglomerate transformed into spherical microparticles with a smooth surface. While annealing at 165 °C a magnetic field of 35 mT was applied to orient the iron oxide nanoparticles for 2 hours. The spherical shape and the orientation of the nanoparticles are preserved after cooling.
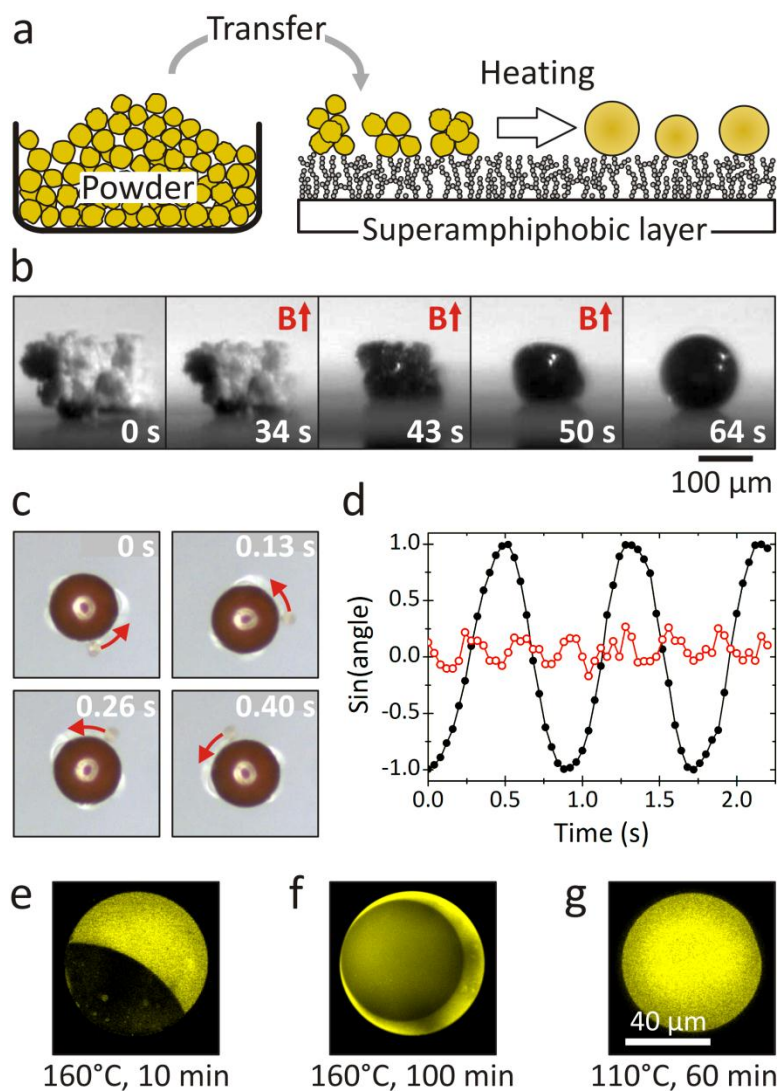
Figure 4| Microspheres by melting a thermoplastic polymer on a superamphiphobic layer.
a, Schematic of the strategy. **b**, Sequence of video microscope images of a polystyrene/iron-oxide composite powder annealed at 165 °C for 2 h in a magnetic field of 35 mT (B↑) on a superamphiphobic layer. Polystyrene was synthesized in house by anionic polymerization (M_W=5.8 kg/mol, T_g=78 °C). The composite microsphere contained 12 vol% of iron-oxide. **c**, Video microscope images of a polystyrene/iron-oxide microsphere in water rotating in an external magnetic field of 1.3 mT at 1.2 Hz. The rotation can be seen following the defect indicated by the red arrow. **d**, Sine of the orientation of a composite microsphere fabricated in the presence (black) and absence (red) of an external magnetic field. **e**, Fluorescence confocal microscope images of a polystyrene/PMMA blend particle annealed at 160 °C for 10 min, **f**, 160

°C for 100 min, **g**, and at 110 °C for 1 h. Polystyrene was labeled with rhodamine B. Excitation wavelength: 570 nm.

To demonstrate that the composite microspheres acquired a permanent magnetic dipole moment, we dispersed individual microspheres in water and exposed them to a weak, rotating magnetic field (Fig. 4c,d). The microspheres rotated with a frequency corresponding to the external magnetic field (Supplementary Fig. S2). When the polymer melt solidified without applying an external field the microspheres did not rotate but performed an oscillatory or rocking motion (Fig. 4d) (Supplementary Movie. S2). Cryo-focused ion beam milling combined with scanning electron microscopy showed that the nanoparticles formed elongated aggregates when applying an external magnetic field during heating (Supplementary Fig. S3).

To document the generality of our synthetic approach we produced Janus microspheres from polystyrene and poly(methyl methacrylate) (PMMA). The polystyrene/PMMA blend (synthesis described in supplementary information) was placed on a superamphiphobic surface and annealed at 160 °C. This temperature was well above the glass transition temperatures of both polystyrene (T_g=91 °C) and PMMA (T_g=120 °C). Polystyrene was tacked with fluorescent dye to visualize the phase separation by confocal microscopy. Since we used a blend containing equal amounts of polystyrene and PMMA (1:1 w/w) the Janus microspheres consisted of one half polystyrene and the other half of PMMA (Fig. 4e). The degree of phase separation depends on the annealing period and particle size (Supplementary Fig. S4). Since polystyrene shows a lower interfacial tension with air than PMMA, polystyrene in thermodynamic equilibrium embeds PMMA[30]. This was indeed observed when annealing for a long time (100 min at 160 °C in Fig. 4f). Thus, the surface properties can be tuned by the duration of annealing. To verify that phase separation requires heating both components above their glass transition temperatures we annealed another particle at 110 °C for 1 hour (Fig. 4g). No phase separation was observed.

Superamphiphobic layers can be used for solvent and emulsifier free particle synthesis. This challenges the paradigm that defined organic particles have to be prepared in a confinement formed by an immiscible liquid. Particles can be made by radical-polymerization or from one single polymer without surface active compounds. Avoiding solvents excludes the pollution of a continuous phase by monomers, initiators, etc. Expensive purification of a continuous aqueous

phase - a major problem in the industrial emulsion polymerization - becomes obsolete. Such a method fulfills all demands of a modern green chemistry. Furthermore, migration and ageing effects due to a slow phase separation between particles and stabilizers typically occurring in particle films is avoided. Finally, this method opens the door to a new generation of particles for medical applications e.g. for drug delivery. Since only one component is used government approval for clinical testing is much simplified.

References

1   Lima, A. C., Sher, P. & Mano, J. F. Production methodologies of polymeric and hydrogel particles for drug delivery applications. *Expert Opin. Drug Deliv.* **9**, 231-248 (2012).

2   Ma, S. H. *et al.* Fabrication of Microgel Particles with Complex Shape via Selective Polymerization of Aqueous Two-Phase Systems. *Small* **8**, 2356-2360 (2012).

3   Choi, J. W. *et al.* An integrated microfluidic biochemical detection system for protein analysis with magnetic bead-based sampling capabilities. *Lab Chip* **2**, 27-30 (2002).

4   Galisteo-López, J. F. *et al.* Self-Assembled Photonic Structures. *Adv. Mater.* **23**, 30-69 (2011).

5   Dendukuri, D. & Doyle, P. S. The Synthesis and Assembly of Polymeric Microparticles Using Microfluidics. *Adv. Mater.* **21**, 4071-4086 (2009).

6   Comiskey, B., Albert, J. D., Yoshizawa, H. & Jacobson, J. An electrophoretic ink for all-printed reflective electronic displays. *Nature* **394**, 253-255 (1998).

7   Nisisako, T., Torii, T., Takahashi, T. & Takizawa, Y. Synthesis of monodisperse bicolored janus particles with electrical anisotropy using a microfluidic co-flow system. *Adv. Mater.* **18**, 1152-1156 (2006).

8   Ghosh, A., Sheridon, N. K. & Fischer, P. Voltage-Controllable Magnetic Composite Based on Multifunctional Polyethylene Microparticles. *Small* **4**, 1956-1958 (2008).

9   Roh, K. H., Martin, D. C. & Lahann, J. Biphasic Janus particles with nanoscale anisotropy. *Nature Materials* **4**, 759-763 (2005).

10   Nie, Z. H., Li, W., Seo, M., Xu, S. Q. & Kumacheva, E. Janus and ternary particles generated by microfluidic synthesis: Design, synthesis, and self-assembly. *J. Am. Chem. Soc.* **128**, 9408-9412 (2006).

11   Du, J. Z. & O'Reilly, R. K. Anisotropic particles with patchy, multicompartment and Janus architectures: preparation and application. *Chem. Soc. Rev.* **40**, 2402-2416 (2011).

12   Chen, Q. *et al.* Supracolloidal Reaction Kinetics of Janus Spheres. *Science* **331**, 199-202 (2011).

13   Hu, J., Zhou, S. X., Sun, Y. Y., Fang, X. S. & Wu, L. M. Fabrication, properties and applications of Janus particles. *Chem. Soc. Rev.* **41**, 4356-4378 (2012).

14   Matyjaszewski, K. & Davis, T. P. *Handbook of Radical Polymerization*. (J.A. Wiley & Sons, 2002).

15   Kaufman, J. J. *et al.* Structured spheres generated by an in-fibre fluid instability. *Nature* **487**, 463-467 (2012).

16   Xu, S. Q. *et al.* Generation of monodisperse particles by using microfluidics: Control over size, shape, and composition. *Angew. Chem. Int. Ed.* **44**, 724-728 (2005).

17   Chen, C. H., Abate, A. R., Lee, D. Y., Terentjev, E. M. & Weitz, D. A. Microfluidic Assembly of Magnetic Hydrogel Particles with Uniformly Anisotropic Structure. *Adv. Mater.* **21**, 3201-3204 (2009).

18   Yuet, K. P., Hwang, D. K., Haghgooie, R. & Doyle, P. S. Multifunctional Superparamagnetic Janus Particles. *Langmuir* **26**, 4281-4287 (2010).

19   Rastogi, V. *et al.* Synthesis of Light-Diffracting Assemblies from Microspheres and Nanoparticles in Droplets on a Superhydrophobic Surface. *Adv. Mater.* **20**, 4263-4268 (2008).

20   Marín, A. G. *et al.* Building microscopic soccer balls with evaporating colloidal fakir drops. *Proc. Natl. Acad. Sci. USA* **109**, 16455-16458 (2012).

21   Shibuichi, S., Yamamoto, T., Onda, T. & Tsujii, K. Super water- and oil-repellent surfaces resulting from fractal structure. *J. Colloid Interface Sci.* **208**, 287-294 (1998).

22   Chen, W. *et al.* Ultrahydrophobic and ultralyophobic surfaces: Some comments and examples. *Langmuir* **15**, 3395-3399 (1999).

23   Xie, Q. D. *et al.* Facile creation of a super-amphiphobic coating surface with bionic microstructure. *Adv. Mater.* **16**, 302-305 (2004).

24   Tuteja, A. *et al.* Designing superoleophobic surfaces. *Science* **318**, 1618-1622 (2007).

25   Yao, X., Song, Y. L. & Jiang, L. Applications of bio-inspired special wettable surfaces. *Adv. Mater.* **23**, 719-734 (2011).

26   Pan, S., Kota, A. K., Mabry, J. M. & Tuteja, A. Superomniphobic surfaces for effective chemical shielding. *J. Am. Chem. Soc.* **135**, 578-581 (2013).

27   Herminghaus, S. Roughness-induced non-wetting. *Europhys. Lett.* **52**, 165-170 (2000).

28   Butt, H. J. *et al.* Design principles for superamphiphobic surfaces. *Soft Matter* **9**, 418-428 (2013).

29   Deng, X., Mammen, L., Butt, H.-J. & Vollmer, D. Candle Soot as a Template for a Transparent Robust Superamphiphobic Coating. *Science* **335**, 67-70 (2012).

30   Marenduzzo, D. & Orlandini, E. Phase separation dynamics on curved surfaces. *Soft Matter* **9**, 1178-1187 (2013).

Supporting Information

Synthesis of polystyrene and labeling with rhodamine B

A 200 mL ampoule was filled with 140 mL freshly distillated cyclohexane and transferred into a glove box. 20 ml freshly distillated styrene was added and the mixture was stirred for a few seconds. The reaction was initiated by adding 3.7 mL sec-butyllithium. The ampoule was taken out of the glove box and put on a vibrating table over night. All steps were done at room temperature. Properties obtained by Gel Permeation Chromatography and differential scanning calorimetry: Molecular weight MW = 5800 g/mol, polydispersity D = 1.05, glass transition temperature Tg = 78 °C.

One half of the solution was quenched with methanol. To obtain labeled polystyrene, 32 mL of a solution containing 5.1 g rhodamine B acid chloride dissolved in 63 ml THF was added to the second part. The mixture was placed on a vibrating table for two days and quenched afterwards with methanol. Properties: M_W= 13800 g/mol, $D = 1.07$, $T_g = 91$ °C.

The labeled and the none labeled polystyrene were equally processed. The dissolved polystyrene was passed through a folded filter and the solvent was removed using a rotary evaporator. The residue was re-dissolved in 200 mL THF and precipitated in 1.5 L methanol to remove unbound dye. This procedure was repeated twice. Finally the product was dried.

Synthesis of iron oxide nanoparticles

$FeCl_3 \cdot 6H_2O$ (5.4 g) and sodium oleate (18.25 g) were dissolved in a mixture of ethanol (40 mL), water (30 mL), and hexane (70 mL). The resulting solution was heated to 70 °C and kept at that temperature for 4 hours. Then, the reaction was cooled down to room temperature. The upper organic layer containing the iron-oleate complex was washed three times with 15 mL water. Then, the iron-oleate complex in a waxy solid form was obtained by evaporating the solvents.

Iron-oleate complex (1.8 g) and oleic acid (0.285 g) were dissolved in 1-octadecene (10 g) at room temperature. The solution was heated to 320 °C slowly and kept at that temperature for 30 min. Then, the solution was cooled down to room temperature. Ethanol (25 mL) was added to the solution to precipitate the nanoparticles. The nanoparticles were separated by centrifugation

at 5000 rpm. Then, the resulting nanoparticles were dispersed in a minimal amount of toluene and precipitated with excess ethanol. The nanoparticles were isolated via centrifugation at 5000 rpm. The isolated nanoparticles were dispersed in THF for subsequent experiments.
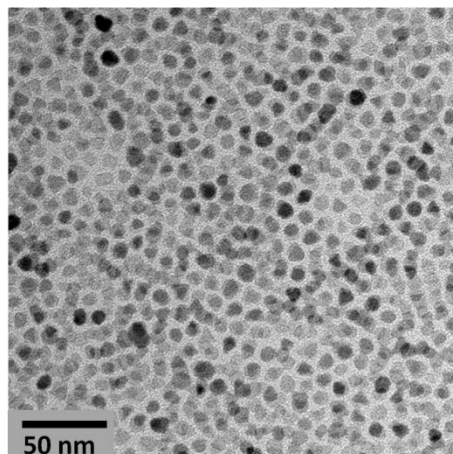

Figure S1| Transmission electron micrograph of the iron oxide nanoparticles.

Synthesis of iron oxide/polystyrene composite powder

To fabricate magnetic microspheres, the nanoparticles were dispersed in THF together with the dissolved polystyrene (M_W = 5800 g/mol). The dispersion was precipitated in methanol and dried at 30°C in vacuum for 1 day, resulting in a homogeneous polymer-nanoparticle powder.
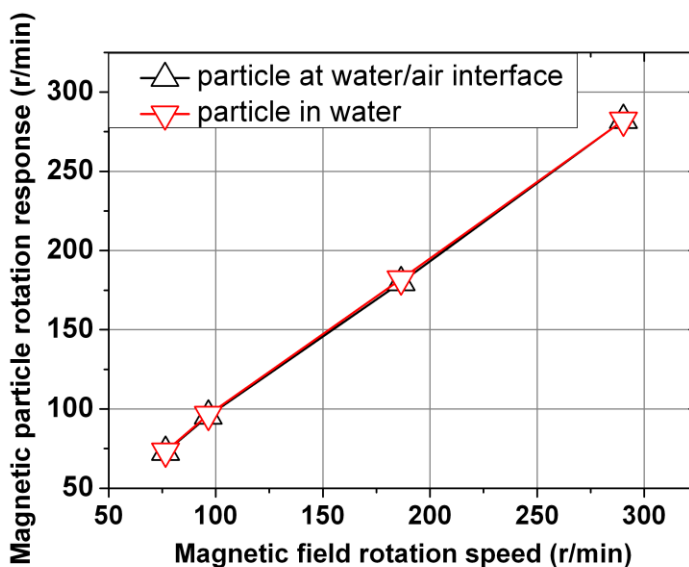
Figure S2| The rotation velocity of magnetic particle versus the rotation speed of the external magnetic field. Both particles were measured at the water/air interface and fully dispersed in water. The torque applied by the external field was sufficient to overcome the viscous friction up to at least 4.8 Hz.

Cryo-FIB/SEM of magnetic particles

To further analyze the distribution and morphology of the iron oxide nanoparticles in the polymer matrix we carried out cryo-focused ion beam/scanning electron microscopy (cryo-FIB/SEM)[1]. The microparticles were first sputter-coated with 100 nm Platinum. Then vertical slices of 200 nm were milled away in a Ga^+ focused ion been (FIB, FEI Nova 600 Nanaolab) at room temperature. After removing a slice the structure was imaged in the scanning electron microscopy (SEM) mode. Without a magnetic field during annealing, the iron oxide nano-particles form small aggregates which are randomly distributed and oriented (Supplementary Fig. S3a). The nanoparticles tend to aggregate because the residual magnetic moments lead to a weak attraction. When a magnetic field was present during annealing, the iron oxide nanoparticles formed elongated aggregates parallel to the field (Supplementary Fig. S3b). An external field leads to an alignment of the magnetic dipoles and consequently to much stronger attraction between the particles. When this attractive potential overcomes thermal energy, the nanoparticles orient along the field lines.
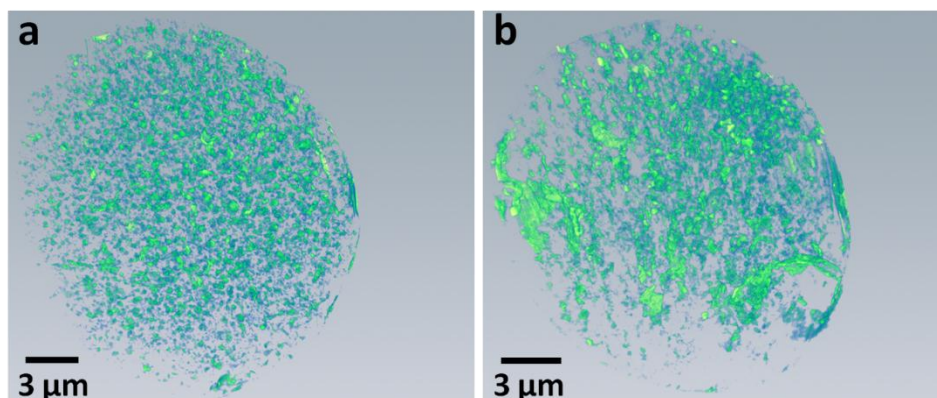

Figure S3| Three-dimensional reconstruction obtained by cryo-FIB/SEM tomography. a, Composite microspheres fabricated without a magnetic field. **b,** In the presence of a magnetic field. Aggregates of iron oxide nanoparticles are shown in green.

Production of polymer blend powder

Polystyrene and PMMA (1:1 w/w) were dissolved in tetrahydrofuran (THF) at a concentration of 20 mg/mL. Polystyrene was labeled with rhodamine B to visualize it by laser scanning confocal microscopy. THF is a good solvent for both polymers. Then the polymers were precipitated in methanol. Residual THF was extracted by drying at 30 °C under vacuum for 1 day. Alternatively, both powders could be mixed by shaking. However, in that case it is more difficult to achieve uniform mixing.

Polymer	M_W (g/mol)	γ at 120 °C (mN/m)	γ at 160 °C (mN/m)	T_g
Polystyrene	5800	34	32	78 °C
PMMA	9500	46	43	120 °C

Table. S1. Characteristics of polystyrene and poly(methyl methacrylate) (PMMA) including molecular weight M_W, surface tension γ, and glass transition temperature T_g.[2-3]

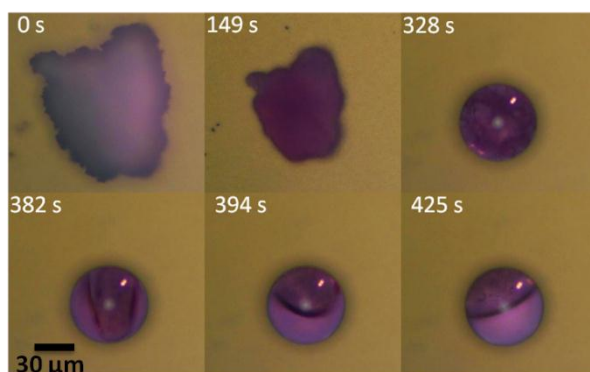**Phase separation of PMMA and dyed polystyrene**

Figure S4| Time resolved video microscopy images of the phase separation of PMMA and dyed polystyrene. Polystyrene was sprinkled on a superamphiphobic layer. Thereafter, the layer was heated to 160 °C, inducing melting of polystyrene and particle formation.
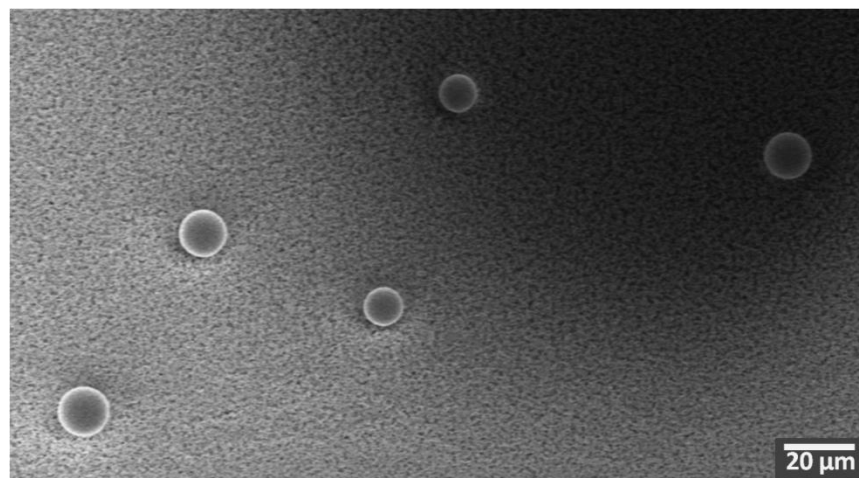
Figure S5| Polystyrene particles after heating on a superamphiphobic surface. Relatively monodisperse particles are obtained when the powder was filtered by a mesh before sprinkling the powder on a superamphiphobic surface. Particle diameter: 12 ± 1 µm.

References

1   Rykaczewski, K., Landin, T., Walker, M. L., Scott, J. H. J. & Varanasi, K. K. Direct Imaging of Complex Nano- to Microscale Interfaces Involving Solid, Liquid, and Gas Phases. *ACS Nano* **6**, 9326-9334 (2012).

2   Cifra, P., Nies, E. & Karasz, F. E. Free Surface Profile and Surface Tension in a Polymer Melt: A Monte Carlo Study. *Macromolecules* **27**, 1166-1171 (1994).

3   Lau, W. W. Y. & Burns, C. M. Kinetics of spreading. Polystyrene melts on plane glass surfaces. *Journal of Colloid and Interface Science* **45**, 295-302 (1973).

Acknowledgements

I'd like to give my thanks and gratitude to Prof. Dr. Hans-Jürgen Butt for offering me this nice opportunity to study in MPIP, and providing fruitful discussions and direct this research and write the dissertation.

I would like to give special thanks to my supervisor PD Dr. Doris Vollmer, who provided me with such an interesting and challenging topic and supported me during the whole process. I am very grateful for her nice guidance, nice ideas, great efforts, and personal support.

My thanks also go to Dr. Günter Auernhammer for his help and really useful discussion.
Dr. Periklis Papadopouls, Lena Mammen, Maxime Paven, Gabriele Schäfer, and Frank Schellenberger for their creative work and nice cooperation made the outcome fruitful.

I am grateful to many colleagues in the AK-Butt working group, who shared their experiences and provided precious counsel and advice.

Finally, I would like to express my deepest gratitude to my parents and my wife Chunxiao Ma for their constant support, understanding, encourages, and loves.

<div align="center">*Curriculum Vitae*</div>

Personal information:
  First name: Xu
  Last name: Deng
  Date of Birth: 21.10.1984
  Nationality: China
  Sexual: Male

Educational Background:
    2009.11-present   Ph.D candidate
                     Max Planck Institute for Polymer research, Germany
    2007.9-2009.8   Gyeongsang National University, South Korea

                     Master of Science in Polymer Science and Engineering (GNU)
    2008.12-2009.3   Max Planck Institute for Polymer research, Germany

    2003.9-2007.8   Tianjin Polytechnic University, China
                   Dept of Materials Science and Engineering
Bachelor of Science in Materials Science and Engineering, Major in Polymer Materials (TJPU)

Publications:
Google scholar linkage**:** http://scholar.google.com/citations?user=Z3RzWoQAAAAJ

1. *Xu Deng, Maxime Paven, Periklis Papadopoulos, Ming Ye, Si Wu, Thomas Schuster, Markus Klapper, Doris Vollmer, Hans-Jürgen Butt*
   Solvent-free synthesis of microparticles on superamphiphobic surfaces. Under review (2013)

2. *Xu Deng, Frank Schellenberger, Periklis Papadopoulos, Doris Vollmer, Hans-Jürgen Butt*
   Liquid drops impacting superamphiphobic coatings. Under review (2013)

3. *Xu Deng, Lena Mammen, Hans-Jürgen Butt, and Doris Vollmer*
   Candle Soot as a Template for a Transparent Robust Superamphiphobic Coating. ***Science (2012),335,67***

4. *Xu Deng, Lena Mammen, Yanfei Zhao, Philipp Lellig, Klaus Müllen, Chen Li, Hans-Jürgen Butt, and Doris Vollme*
   Transparent, thermally stable and mechanically robust superhydrophobic surfaces made from porous silica capsules. ***Advanced Materiasls*** *(2011), 23, 2962*

5. *Periklis Papadopoulos, Lena Mammen, Xu Deng, Doris Vollmer, Hans-Jürgen Butt*
    How superhydrophobicity breaks down. ***Proceedings of the National Academy of Sciences*** *(2013), 110, 9, 3254*

6. *Periklis Papadopoulos, Xu Deng, Doris Vollmer and Hans-Jürgen Butt*

<div align="center">117</div>

*Electrokinetics on superhydrophobic surfaces. **Journal of Physics: Condensed Matter (2012), 24, 464110***

7. *Periklis Papadopoulos, Lena Mammen, <u>Xu Deng</u>, Doris Vollmer and Hans-Jürgen Butt, Pinning-induced Variations of the Contact Angle of Drops on Microstructured Surfaces. **Chemisty Letters** (2012), 41, 1343*

8. *Lena Mammen, <u>Xu Deng</u>, Maria Untch, Dandapani Vijayshankar, Periklis Papadopoulos, Rüdiger Berger, Enrico Riccardi, Frédéric Leroy, and Doris Vollmer,*
Wetting on the Microscale: Effect of Nanoroughness on Highly Hydrophobic and Superhydrophobic Coatings. ***Langmuir** (2012), 28, 15005*

9. *Periklis Papadopoulos, <u>Xu Deng</u>, Lena Mammen, Dirk-Michael Drotlef, Glauco Battagliarin, Chen Li, Klaus Müllen, Katharina Landfester, Aranzazu del Campo, Hans-Jürgen Butt, and Doris Vollmer*
*Wetting on the Microscale: Shape of a Liquid Drop on a Microstructured Surface at Different Length Scales. **Langmuir** (2012), 28, 8392*

10. *Maria D'Acunzi, Lena Mammen, Maninderjit Singh, <u>Xu Deng</u>, Marcel Roth, Günter K. Auernhammer, Hans-Jürgen Butt and Doris Vollmer*
*Superhydrophobic surfaces by hybrid raspberry-like particles. **Faraday Discuss** (2010),146, 35-48*

Patent:
Mechanical stable, transparent, superhydrophobic, and oleophobic surfaces made of hybrid raspberry-like particles, EUROPEAN PATENT APPLICATION, EP 2 484 726 A1

Conference:

2012	14th international association of colloids and interface conference, Japan
2011	2011 MRS Fall Meeting, Boston, USA (**Oral presentation**)
2011	The 25th European Colloid and Interface Society meeting, Germany (**The best poster prize, Issued by Elsevier Publishing Group**)
2009	13th IUPAC Conference on Polymers and Organic Chemistry, Canada

Awards:

2012	Chinese Government Award for Outstanding Self-financed Students Abroad
2011	The best poster prize, 25th European Colloid and Interface Society Conference
2009	Brain Korea 21 scholarship

Languages:
English, Chinese, Korean